STELLAR OCCULTATION STUDIES OF TRITON'S ATMOSPHERE

by

Catherine Blair Olkin

S. B., Aeronautics and Astronautics, Massachusetts Institute of Technology (1988)
M. S., Aeronautics and Astronautics, Stanford University (1989)

Submitted in Partial Fulfillment of the Requirements for the Degree of

DOCTOR OF PHILOSOPHY

in

EARTH, ATMOSPHERIC AND PLANETARY SCIENCES

at the

MASSACHUSETTS INSTITUTE OF TECHNOLOGY

June, 1996

Author _____

Department of Earth, Atmospheric, and Planetary Sciences
April 30, 1996

Certified by _____

Professor James L. Elliot
Thesis Supervisor
Department of Physics and
Department of Earth, Atmospheric, and Planetary Sciences

Accepted by _____

Professor Thomas Jordan
Chairman, Department of Earth, Atmospheric, and Planetary Sciences

Stellar Occultation Studies of Triton's Atmosphere

by

Catherine Blair Olkin

Submitted to the Department of Earth, Atmospheric and Planetary Sciences
on April 30, 1996 in Partial Fulfillment of the Requirements for the Degree of
Doctor of Philosophy

Abstract

This thesis presents new results about Triton's atmosphere from the analysis of three stellar occultations observed from 1993 to 1995. These data are complementary to the observations of the Voyager 2 spacecraft. They probe an altitude range (20–100 km) intermediate to those sensed by the spacecraft instruments and provide a temporal baseline for monitoring seasonal change in Triton's atmosphere. These stellar occultation observations have good spatial coverage and include the first Triton central-flash occultation.

We have analyzed the data using three different methods to retrieve information about Triton's atmosphere. The standard analysis methods of numerical inversions and simple atmospheric model fitting were applied. Also a new method for fitting physical models of atmospheric structure was applied to these occultation data.

Using these methods, we see no detectable change in atmospheric pressure between 1993 and 1995. From isothermal model fits, the pressure at 1400 km from the center of Triton, where these observations are most sensitive, changed by -0.09 ± 0.26 μbar/yr. Using the physical model fits to relate conditions at the microbar level to the surface, we find the change in surface pressure to be less +4.4 μbar/yr and more than –6.3 μbar/yr (3σ).

The atmospheric pressure derived from the occultation data is greater than predicted by a model of the Voyager data (Strobel *et al.* 1996). This pressure difference can be explained by an underestimate of the surface radius or by an inaccurate description of the atmospheric structure in the microbar region (where Voyager was not sensitive). The temperature gradient predicted by models of Voyager data (Krasnopolsky *et al.* 1993; Strobel *et al.* 1996) is not present in the highest signal-to-noise ratio data.

We see evidence for asymmetry in the scale height of Triton's atmosphere from one site. The asymmetry can be due to a different temperature, temperature gradient or mean molecular weight between the immersion and emersion locations. If interpreted as a temperature difference, we find the region probed during immersion to be 7 K colder than that probed during emersion.

Thesis Supervisor: James L. Elliot
Title: Professor of Earth, Atmospheric, and Planetary Sciences and
Professor of Physics

Acknowledgments

First and foremost, I would like to thank Jim Elliot. He gave an engineer with an interest in planetary science the opportunity to become an astronomer. Over the last 5 years, he has taught me not only how to conduct scientific research, but also the other skills needed to be a successful scientist. This project is the result of his drive to push the limits of occultation observations to smaller and smaller bodies. This thesis has benefited every step of the way from his insight and enthusiasm. Jim also understands that a happy graduate student is a productive graduate student. Thank you for allowing me to complete my thesis from California.

Stellar occultation data are most easily interpreted when multiple occultation chords are observed. There was a successful effort by the occultation community to record the 1995 Triton occultation. I would like to thank Marc Buie, Ted Dunham, Bill Hubbard, Dave Rank, and Harold Reitsema for supplying their data for use in this thesis.

Over the years, I have had a few occasions to work with the staff of the Kuiper Airborne Observatory and it has always been a pleasure. I hope that the next generation airborne observatory (SOFIA) has as dedicated a team. I would also like to acknowledge the staff of the Infrared Telescope Facility on Mauna Kea for their assistance during our observing run in August 1995. In particular, thank you for helping us mount our visible system on the optical port of NSFCAM.

I would like to acknowledge the contributions to this thesis of past and present MIT students and staff. I thank Phil Tracadas for valuable discussions about numerical inversions, Dawn Chamberlain for her work on the physical-model fitting method and Steve McDonald for his participation in occultation predictions. Improvements in the prediction methods are as much a result of his work as mine. I would also like to recognize the more indirect (but quite substantial) contributions of Amanda Bosh and Leslie Young. Not only have we have had many interesting scientific (and non-scientific) discussions, but during my first few years of graduate school, they taught me the basics of astronomy from photometry to astrometry.

This thesis would not be nearly as interesting without the model of Strobel *et al.* (1996) for comparison. I would like to thank Darrell Strobel and Xun Zhu for providing many models for comparison.

I would like to thank my parents for their constant encouragement in whatever I do and my friends for always being interested. Finally, I would like to thank Terry. He has constantly supported my decision to go to graduate school and understood when I had to go out of town for weeks.

Table of Contents

List of Figures

List of Tables

1. Introduction

Prior to the Voyager 2 encounter with the Neptune system in 1989, we knew little about Triton. There was significant uncertainty in such basic parameters as the satellite's albedo, radius, and mass (Cruikshank and Brown 1986). However, there had been indications of an atmosphere from ground-based spectroscopy that revealed CH_4 ice and N_2 ice on Triton's surface (Cruikshank and Silvaggio 1979; Cruikshank *et al.* 1984). For a wide range of temperatures, these species would coexist as vapor and ice, and nitrogen would be the major atmospheric constituent because of its larger vapor pressure. Despite this information, the surface pressure of Triton's atmosphere was uncertain because the vapor pressure of N_2 is strongly dependent on temperature (Brown and Ziegler 1980) and the pre-Voyager estimates of Triton's surface temperature depended on the satellites albedo which was not accurately known.

The atmosphere on Triton was confirmed by the observations of the Voyager 2 instruments. Three instruments detected Triton's tenuous atmosphere: the Radio Science Subsystem (RSS), the Ultraviolet Spectrometer (UVS) and the Imaging Subsystem (ISS). The occultation of the spacecraft's radio signal has been used to determined the temperature and pressure in Triton's atmosphere near the surface (Tyler *et al.* 1989; Gurrola 1995). The UVS instrument recorded both a solar and stellar occultation. These data have been used to determined the temperature and pressure in the altitude range of 500-700 km (Broadfoot *et al.* 1989; Krasnopolsky *et al.* 1993) and the concentration of methane near 40 km altitude.

In this thesis, we present new results about Triton's atmosphere from ground-based observations of three stellar occultations by Triton. These data are complementary to the observations of the Voyager 2 spacecraft. They probe an altitude range (near the microbar pressure level, 20-100 km altitude) intermediate to those sensed by the spacecraft's instruments and provide a temporal baseline for monitoring seasonal change in Triton's atmosphere. The new results will be compared to a model (Strobel *et al.* 1996) of the atmosphere based on Voyager data. We will refer to this model as the nominal Voyager model.

The first ground-based stellar occultation by Triton was observed in 1993 (Elliot *et al.* 1993; Olkin *et al.* 1993). Two years later, the occultation of a double star by Triton was widely observed (Dunham *et al.* 1995; Olkin *et al.* 1995; Reitsema *et al.* 1995; Wasserman *et al.* 1995). The occultation chords from the double star event covered

almost 75 percent of Triton's shadow from the furthest north chord to the furthest south chord (with a mean spacing between chords of 400 km). These are the three stellar occultation events presented in this thesis (and the only ground-based stellar occultations observed to date).

Stellar occultations provide an inexpensive method, relative to *in situ* measurements, for probing planetary atmospheres with high-spatial resolution [see Elliot and Olkin (1996) for a complete description of what one can learn about planetary atmospheres from stellar occultations]. From the shape of these occultation light curves, we investigate Triton's atmospheric structure near the microbar pressure level. From the lack of spikes in the light curves, we place limits on the turbulence in the atmosphere. From the stellar occultation probes of Triton's atmosphere at two different times, we constrain the change in atmospheric pressure with time. Finally, from the multiple chord observations of the 1995 stellar occultation, we find latitudinal differences in the scale height of Triton's atmosphere.

The thesis begins with a look at the high-speed imaging data (Chapter 2) which recorded the occultations. Next we present astrometric results that locate the occultation chords relative to the center of Triton (Chapters 3 and 4). Chapters 5, 6 and 7 apply different analysis methods to the stellar occultation data to learn about Triton's atmospheric structure in the microbar region. These methods are: (i) isothermal model fits, (ii) numerical inversions, and (iii) physical (numerical) model fits–a new technique. A synthesis of the results from the different analysis methods and the implications of the results will be presented in Chapter 8. Chapter 9 summarizes the new conclusion about Triton's atmosphere and technical developments used in this analysis. The first two appendices present occultation prediction methods. Appendix III describes the instrument mount used at the Infrared Telescope Facility for simultaneous dual-wavelength observations. Appendix IV presents a new method to determine the closest approach distance between a star and a solar system body that passes nearby. Appendix V lists the *Mathematica* notebooks used in these analyses. Finally, Appendix VI is a glossary of terms and acronyms.

2. Triton Occultation Data[1]

In this chapter, we describe the high-speed imaging observations of the Triton occultations, the method used to transform the imaging data into an occultation light curve, and discuss post-event photometry to establish the zero-flux level of the occulted star.

2.1 Observational Parameters

This thesis presents the analysis of all recorded ground-based stellar occultations by Triton. Recent advances in detector technology have improved the scientific results derivable from these events. Array detectors contributed in two respects. First, the increased quantum efficiency of CCD devices compared with photomultiplier tubes has increased the signal-to-noise ratio (SNR) of a given event (which has increased the number of scientifically interesting opportunities). Second, array detectors allow for more precise photometric and astrometric reduction, including point-spread model fitting, improved background subtraction, and pre- and post-event astrometry. This is critical for Earth-based observations of stellar occultations by Triton because of the scattered-light from Neptune. All these observations have been recorded with array detectors.

The star occulted by Triton in 1993 (Tr60, R magnitude = 13.9) was initially identified from an observational program to search for occultation candidates (McDonald and Elliot 1992). See Appendix I for a description of past and present occultation candidate search methods. McDonald and Elliot (1992) recorded strip scan observations of stars in Triton's path. A strip scan is a CCD image of the sky that can be of arbitrary length in the right ascension direction. The telescope is left stationary, while the columns of the detector are clocked out at the same rate as the stellar images move across the detector (Dunham *et al.* 1991). For small-body occultations (such as Triton events), a refined prediction is needed to accurately place observers in the shadow path. Appendix II presents our methods of occultation prediction refinement through case studies of occultation predictions from 1992 to 1995.

More than a month in advance of the occultation, the location of the occultation shadow path can be uncertain by a diameter of the shadow path or more for a Triton occultation (approximately 2900 km). With this large uncertainty, observations of the

---

[1]Data sets provided by Marc Buie, Ted Dunham, Bill Hubbard, Dave Rank, and Harold Reitsema

(1993) Tr60 occultation were planned from many sites including Western Australia at Perth Observatory, South America at Cordoba Astronomical Observatory, South Africa at the South African Astronomical Observatory and the South Atlantic from the Kuiper Airborne Observatory. The event would occur while Triton was near opposition which is advantageous because observers can be located anywhere in the shadow path and still be in darkness.

The reconstructed occultation shadow path is shown in Figure 2.1. The only observed occultation chord was recorded from the Kuiper Airborne Observatory (KAO). The skies in South Africa and Argentina were cloudy and the occultation path passed north of observers in Australia.

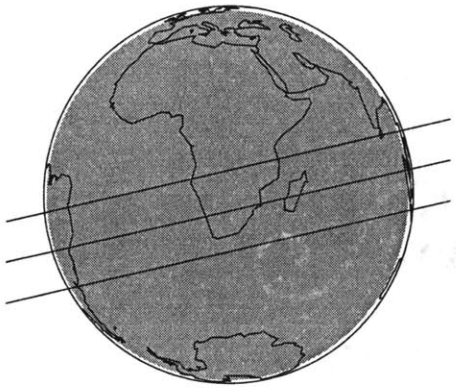

Figure 2.1 The shadow path of the Tr60 occultation. This is the globe of Earth as seen from Triton at the midtime of the occultation. The three lines are the shadow path (northern limit, midline and southern limit). The shaded region indicates where the sun is below -12° altitude. The occultation would have been visible from South Africa and Argentina; however, clouds prevented the observations. The KAO was flying above the south Atlantic ocean. Australia is south of the occultation shadow.

The KAO was deployed from Punta Arenas Chile (at the southern tip of South America) due to the expected southern track of the occultation shadow. Each day before the occultation, we received new astrometric measurements, and the predicted shadow path was refined. Each day it consistently moved north. This complicated the deployment plans as we needed the full flight range of the KAO to get to the occultation shadow (over the ocean). For the occultation flight, we needed to refuel in Buenos Aires, Argentina before returning to Chile. Despite the logistical difficulties, the KAO team got us to the predicted shadow path for the observations at the designated time.

The 1995 stellar occultation candidate Tr148 was also identified using strip scan observations (McDonald and Elliot 1995). The shadow path of this event was originally predicted to be north of the Earth (not visible). However, experience with other occultation candidate stars, whose refined paths were off the Earth, led us to consider candidates with tracks off the Earth. If we were losing potential occultation events because the refined predictions placed the shadow paths off Earth, surely we would be gaining events that were originally predicted not to be visible. From observations of

Tr148 by the Carlsberg Automatic Meridian Circle (CAMC), we discovered that the occultation path would likely be visible from Earth. With this information, deployment plans were made. Details of the prediction refinement are given in Appendix II.

This event occurred about one month after opposition. Again, most of the Triton-facing hemisphere of Earth was in darkness. Table 2.1 lists the sites where observations were planned. From some locations, we planned dual wavelength observations (visible and near-infrared) to study extinction in Triton's atmosphere (from the extinction efficiency dependence on wavelength). It was not until after the occultation event that we realized the star was double. The occultation of the brighter companion (Tr148A, V=13.2) was observed from four sites and the occultation of the fainter star (Tr148B, V=14.7) was also recorded from four sites, see Table 2.1. Dual-wavelength observations were made from the IRTF, and two telescopes at Lick Observatory recorded both occultations in two different wavelengths.

As seen from the IRTF, Triton passed within 150 km from the occulted star. This was close enough to record the first Triton central-flash occultation. The increase in flux near the midtime of the event is a result of geometric focusing (see Chapter 5), not being within the evolute of an oblate atmosphere (Elliot *et al.* 1977).

Specifics of the observations, such as telescope, detector and exposure time are given in Table 2.1. All four portable CCD (PCCD) instruments (Buie *et al.* 1993) were used in these observations. These instruments were designed by a consortium of occultation observers (at Lowell Observatory, MIT, NASA Ames Research Center and the University of Arizona) for occultation observations. The detector in a PCCD system is a TH 7883 liquid-cooled CCD from Photometrics with 384×576 pixels (each 23 μm square). The specifications of the detector show a peak quantum efficiency of 40% at 0.7 μm, a readout noise of 8 e^-/pixel. The dark current is 6.5 e^-/sec/pixel at the operating temperature of -45° C. The timing of the instrument is controlled by a GPS time signal through the use of a Trak GPS receiver.

A SNAPSHOT clone (Dunham *et al.* 1985) used at Lick Observatory was also designed for high-speed occultation observations. It uses a Tektronics 2048×2048 CCD and is also triggered from a GPS time signal.

Table 2.1 Observational Parameters

Date	Star	Obs.	Telescope Aperture (m)	Instrument	Int. Time (sec)	Subframe Size[a] (pixels)	Detector Scale (arcsec/pix)	No. Integrations	SNR Per Sec	Observers
93 07 10	Tr60	KAO	0.9	Ames PCCD	0.500	50×50	1.0	4200	16.3	Elliot, Dunham & Olkin
93 07 10	Tr60	Perth[b]	0.6	Lowell PCCD	-	-	-	-	-	L. Wasserman
93 07 10	Tr60	CAO[c]	1.5	U. of A. PCCD	0.333	-	-	1000	-	Hubbard, Reitsema, Carranza
93 07 10	Tr60	SAAO	1.0	MIT PCCD	0.500	40×40	-	5000	-	Millis, Bus
95 08 14	Tr148B	IRTF	3.0	MIT PCCD	0.300	23×23	0.3	8000	43.7	Olkin, Hammel & Cooray
95 08 14	Tr148B	IRTF	3.0	NSFCAM	0.500	48×48	0.31	3600	16.3	Olkin, Hammel & Cooray
95 08 14	Tr148A	KAO	0.9	Ames PCCD	0.342	50×50	1.0	3600	26.5	Elliot & Dunham
95 08 14	Tr148A & B	Lick	0.9	SNAPSHOT	1.000	40×40	2.28	1800	23.6/6.1	McDonald & Young
95 08 14	Tr148A & B	Lick	1.0	LIRC2	3.000	256×256	1.14	260	6.0/1.2	Rank, Holbrook
95 08 14	Tr148B	Lowell	1.8	Lowell PCCD	0.140	46×30	0.59	9400	9.0	Buie, Millis, Wasserman
95 08 14	Tr148A	WIRO	2.3	U. of A. PCCD	0.400	90×50	3.25	3000	5.7	Reitsema, Hill & Howell
95 08 14	-	Steward[c]	2.2	2-channel photometer	-	-	-	-	-	Hubbard, Marcialis
95 08 14	-	Yerkes	1.1	CCD	2-10	252×241	0.6	117	-	Wild, Briggs & Drish

[a] Some observations were recorded with on-chip binning. Subframe size and detector scale are reported in binned pixels.
[b] Track north of observer.
[c] Cloudy. The Tr60 occultation observations from Cordoba were centered on the wrong star because of inadequate setup time due to clouds.

Both systems use a frame-transfer readout scheme to minimize deadtime (the time between integrations). This scheme uses only a subsection of the detector for imaging (this part of the detector is referred to as the subframe). The charge (signal) in the subframe is transferred to the frame-transfer area of the detector and the next integration is begun. The charge in the frame-transfer region is read out during subsequent integrations (for the PCCD systems, the subframe is read out during the next integration and for the SNAPSHOT system, the subframe resides in the frame-transfer region for the next four integrations). This minimizes deadtime because it takes less time to transfer the charge to the frame-transfer region than to read out the subframe. Using the frame-transfer method, the instrument is not losing time while reading out the detector.

A mask can be used to eliminate sky signal and imaging of stars while the charge is in the frame transfer region. For these observations, no mask was used, but care was used in the orientation of the detector such that detectable field stars did not lie in the frame transfer area. Only the observations at the 0.9-m (Crossley) telescope at Lick Observatory had a field star in the frame-transfer region. This instrument was used for strip scans immediately before and after the occultation so the orientation of the detector was fixed. The location of the field star in the recorded subframe is not near Triton.

2.2 Sample Images and Light Curves

In this section, we present sample images, a description of the light curve generation, the Tr60 occultation light curve and the Tr148 occultation light curves from the IRTF, KAO and Lick observations. The other occultation light curves were supplied by their observers. The Tr148B occultation light curve from Lowell Observatory was supplied by M. Buie and the Tr148A occultation light curve from WIRO was provided by W. Hubbard and H. Reitsema.

2.2.1 Tr60 KAO data

Sample images from the KAO observations of the Tr60 event are displayed in Figure 2.2. The shape of the point-spread function (PSF) varies from frame to frame due to poor tracking. To get the highest signal-to-noise (SNR) light curve, we used a numerical PSF model fitting method to determine the intensity of the blended Triton-Tr60 image relative to Neptune. We could not use aperture photometry to derive the light curve from the images because of the proximity of Neptune to the blended Triton-Tr60 and the rapidly changing image shape. Other PSF fitting techniques, such as using an analytic model such as an elliptical Lorentzian (Bosh *et al.* 1992), proved unsatisfactory because the frequently elongated PSF was not well fit by the analytic model.

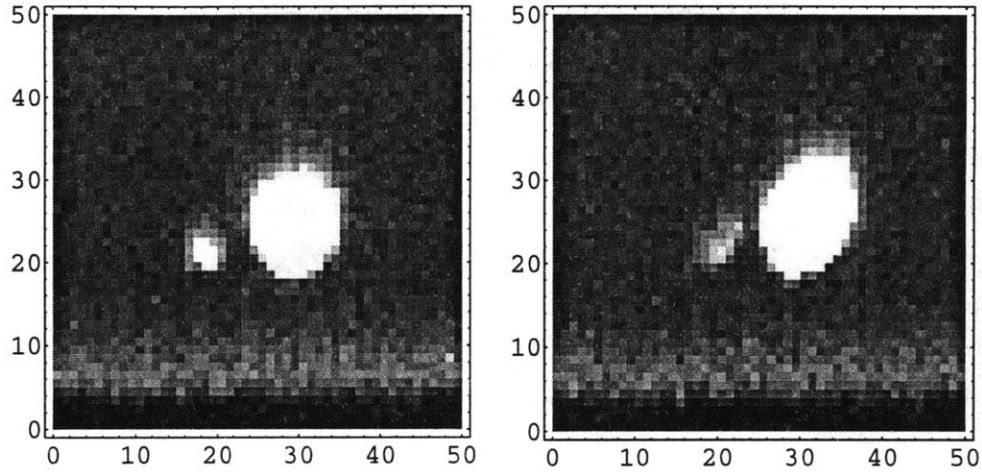

Figure 2.2 Sample images from the Triton occultation of Tr60. The left panel (frame 1803) shows a "round" image while the right panel (frame 1805) shows a "trailed" image. Neptune is the bright object. The other is the blended image of Triton-Tr60. The data were recorded using the NASA Ames PCCD system aboard the Kuiper Airborne Observatory flying above the south Atlantic Ocean. The data were unfiltered with an integration time of 0.5 seconds. A charge transfer efficiency problem is seen by the streaking of the images to the top. The banded pattern in the lower ten rows is an artifact of the detector read out. The image scale is approximately 1 arcsec/pixel.

There are three components to the numerical PSF model fit: (i) a sloping background, (ii) a PSF model for Neptune, and (iii) a PSF model for the blended Triton-Tr60. Only a subsection of each subframe was used in the fitting, so that the bright and dark band at the bottom of the images would not be included.

If a field star brighter than the blended Triton-Tr60 image would have been in the field, it would have been used as a reference PSF. Unfortunately, no such star was available, so Neptune was used. Although Neptune is not a point source (its disk subtends 2.3 arcsec), we can use it as a PSF source because of the 3-5 arcsec seeing.

The model numerical PSF for each frame was derived from a cubic interpolation of the Neptune image with the background removed. The background has a mean value as well as a slope in row and column. After each iteration, the background was recalculated and the numerical PSF model was updated (with the new background removed).

The two-source image model was fit simultaneously to the blended image of Triton-Tr60 and the image of Neptune. The fitted parameters include an offset of the Triton-Tr60 center from Neptune, the peak of the Triton-Tr60 PSF relative to the Neptune peak and three background parameters (mentioned above). Pixels common to both PSFs were not included in the fit. The resulting light curve is displayed in Figure 2.9. The flux scale (ordinate) is the ratio of the blended image to Neptune.

2.2.2 Tr148 IRTF Data

Simultaneous infrared (IR) and visible wavelength observations were made at the IRTF of the Tr148B stellar occultation. Two instruments were used: (i) the NSFCAM (Shure *et al.* 1994), and (ii) the MIT PCCD system mounted on the optical port of the NSFCAM. The mount included a relay lens that increased the image scale by approximately a factor of 7 (from 0.04 arcsec/pixel to 0.3 arcsec/pixel). The reducing optics were designed to sample the PSF with an image scale smaller than the seeing while maintaining a useful field of view (see Appendix III). The field of view was vignetted outside of a circular aperture with diameter equal to 47 arcsec due to the relay lens. This reduced field of view was sufficient to record the occultation. We simultaneously recorded a series of two subframes using the MIT PCCD. The subframe containing Neptune was ~9 arcsec square and the Triton-Tr148 subframe was ~7 arcsec (see Figure 2.3). Vignetting of the optical system distorted the Neptune image such that it was not useful as a PSF source.

The charge transfer efficiency (CTE) problem seen in the Tr60 images is not present in the 1995 data due to a change in the instrument. The clock level was increased from 9 to 10 Volts and the parallel delay was increased (from 9 to 50) for the 1995 observations (E. Dunham, personal communication).

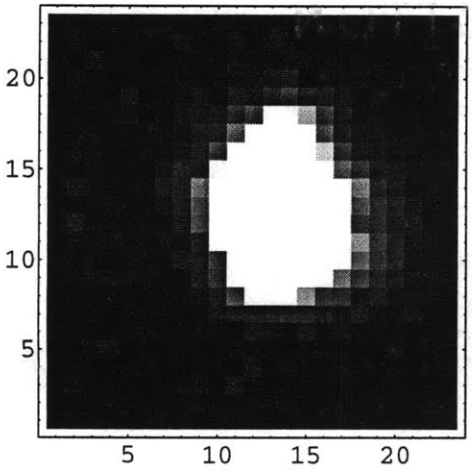

Figure 2.3 Sample IRTF-PCCD image from the Triton occultation of Tr148B. This is the blended image of Triton-Tr148A-Tr148B. The data were recorded using the MIT PCCD system. The data were unfiltered with an integration time of 0.3 seconds. Two subframes were read out; one for Triton and the other for Neptune. The image scale is approximately 0.3 arcsec/pixel.

The occultation light curve (Figure 2.9) was generated with aperture photometry. The signal from the blended object was determined with an aperture 16 pixels square (4.8 arcsec square), centered on the object. The background level was determined from the remaining pixels in the subframe.

In the infrared, a series of approximately 15 arcsec square subframes was recorded with NSFCAM (K filter: center wavelength 2.21 μm and FWHM 0.39 μm). These data

were reduced with aperture photometry. The aperture was 12 pixels square (2.7 arcsec square); see Figure 2.4 for a sample image.

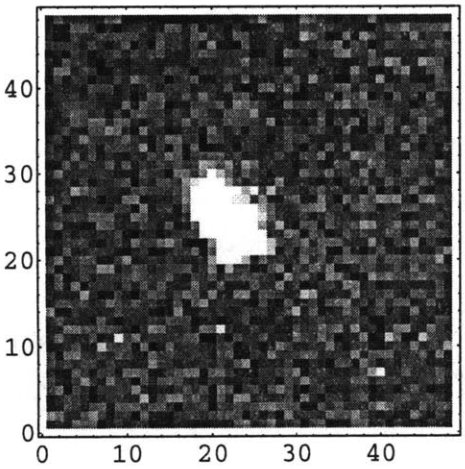

Figure 2.4 Sample IRTF-NSFCAM image from the Triton occultation of Tr148B. This is the blended image of Triton-Tr148A-Tr148B through a K filter. A dichroic in the main beam allowed simultaneous observation in the visible and IR. The image scale is 0.31 arcsec/pixel. The elongation of the PSF is a result of a collimation problem (the collimation was inadvertently set for another instrument).

The PCCD system eliminates deadtime between integrations by recording the images in frame transfer mode, but the NSFCAM instrument does not. See Smith (1995) for a description of the readout scheme of the NSFCAM instrument and calibration of the timing. The deadtime between integrations depends on the number of pixels being read out and the location of those pixels.

To establish the deadtime, we recorded a series of subframes imaging a blinking infrared light-emitting diode (LED). This was done in the same configuration as the occultation observations (box size, box location, integration time and series length). The LED was triggered by the 1 pulse/sec output of a GPS receiver. The first 48 images from the series are displayed in Figure 2.5. With an exposure time of 0.5 sec, the LED is initially seen in every other image. By the eighteenth frame, the deadtime has accumulated to shift the pattern by one exposure. This pattern repeats itself every 21 frames (the first frame was not at the beginning of the pattern). If N is the number of frames between shifts (21), t_d is the deadtime and t_i is the integration time, we find the deadtime by the following equation:

$$t_d = \frac{t_i}{N} \tag{2.1}$$

For this observing setup, the deadtime is 24 ms.

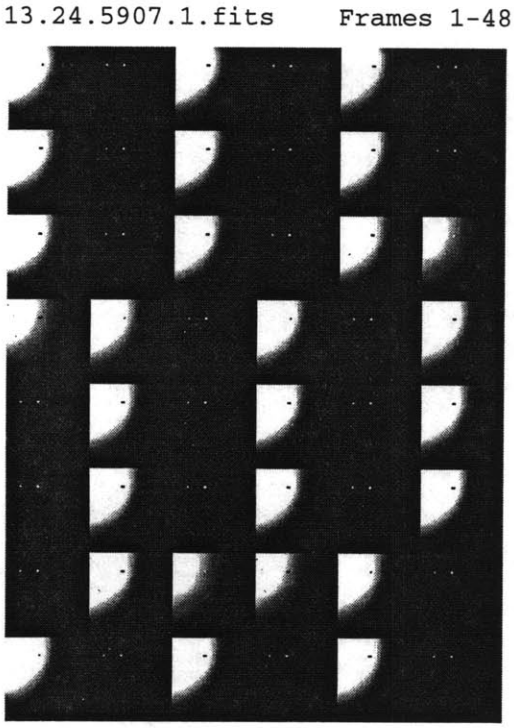

Figure 2.5 The first 48 images in the LED calibration series. The images are in sequential order from right to left then down rows. There are six subframes in a row. The image series was used to establish the deadtime in the readout of the array. The LED was on during the first 100 ms of each second (triggered by a GPS receiver). The exposure time for each image is 0.5 seconds. The alternating pattern of the LED on and off can be seen in the upper left corner of the subframe. Also evident is the shift of this pattern due to the deadtime.

2.2.3 Tr148A KAO data

The occultation of Tr148A was recorded by J. L. Elliot and E. W. Dunham from the Kuiper Airborne Observatory flying north of Hawaii over the Pacific Ocean. At the time of the occultation from the KAO's location, Triton was a few degrees less than 35° above the horizon. The telescope aboard the KAO can point only as low as 35° altitude, so the KAO was tipped about 3° from horizontal for the acquisition. Triton was rising, so the airplane tip was removed slowly during the observations. When flying an airplane at a non-zero roll angle, the lift vector gains a horizontal component and the plane will turn unless rudder is applied. The pilots skillfully kept the plane on course during the roll allowing the occultation data to be acquired.

A sample image from the 3600 recorded subframes is shown in Figure 2.6. The brightest object is Neptune and the image on the right is the blended image of Tr148AB and Triton.

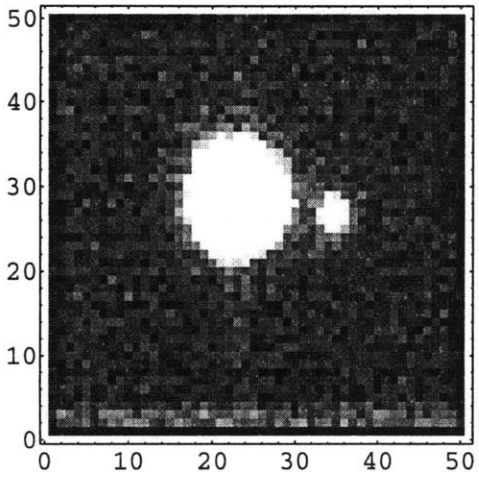

Figure 2.6 Sample KAO-PCCD image from the Triton occultation of Tr148A. This is the blended image of Triton-Tr148A-Tr148B. The data were unfiltered with an integration time of 0.342 sec. The image motion on the KAO was less during the Tr148 occultation relative to the Tr60 occultation. The charge-transfer-efficiency problem, so prominent in the Tr60 images, is also less due to a change in the parallel delay and clocking voltage in the instrument. The banding at the bottom of the subframe is still visible.

Although the start time of the data recording was read from the GPS receiver, the integration timing of the PCCD was not triggered from the GPS receiver because of a communication problem between the computer and the GPS receiver. The integration time was controlled by the clock in the instrument computer, and the integration time was calculated from a series of images of the secondary mirror nodding in and out of the beam. The nodding occurred at 1 cycle per second, controlled by a GPS receiver. The integration time was calculated to be 0.342 sec using a method similar to that described for the deadtime calibration of the NSFCAM series.

The KAO was in the shadow of the Tr148B occultation, but the instrument was not recording at the event time. The Tr148B occultation occurred about 5.5 minutes before the predicted occultation time, and the instrument was not recording this early due to an attempt to correct the problems with the GPS receiver triggering the exposures.

2.2.4 Tr148 Lick (Visible) data

J. S. McDonald and L. A. Young observed the occultation of both Tr148A and Tr148B by Triton from Lick Observatory. They used the 0.9-m Crossley telescope and a clone of the SNAPSHOT CCD system (Dunham *et al.* 1985). A sample subframe is displayed in Figure 2.7. The brightest object is Neptune with the blended image of Triton-Tr148 to the left and above Neptune. The bright star below and to the right of Neptune is a field star about 9.3 arcmin (245 binned rows) from Neptune. At this location, the field star was recorded two integration intervals before the Triton subframe on which it appears. Therefore, the field star is not present on the first or second subframe, but appears for the first time on the third exposure.

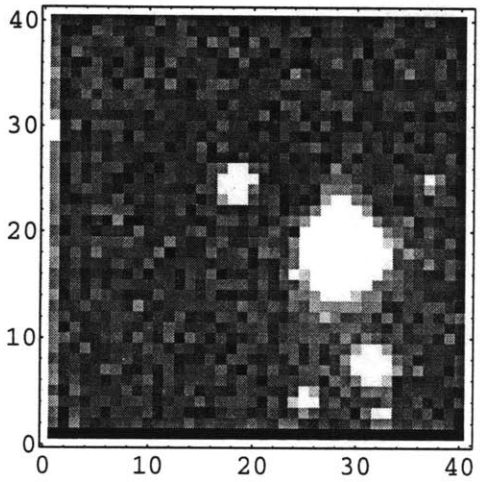

Figure 2.7 Sample Lick-SNAPSHOT image from the Triton occultation of Tr148A and Tr148B. This is the blended image of Triton-Tr148A-Tr148B. The data were unfiltered with an integration time of 1.0 sec. Triton-Tr148 is the object near the center of the frame. Neptune is the brightest object.

2.2.4 Tr148 Lick (Infrared) data

The occultations of Tr148A and Tr148B were recorded in the infrared at Lick Observatory by D. M. Rank and J. Holbrook. K' filter images of the blended Triton-Tr148 were recorded with the Lick infrared camera (LIRC2) instrument (a NICMOS 256×256 pixel array). The LIRC2 instrument does not read out subframes; instead the whole detector is read out. The Triton field was recorded for 260 consecutive frames (13 minutes) around the event time. The images were flattened by A. S. B. Schultz. The light curve was generated by aperture photometry of the flattened images (with a four pixel square aperture). Figure 2.8 shows a sample image.

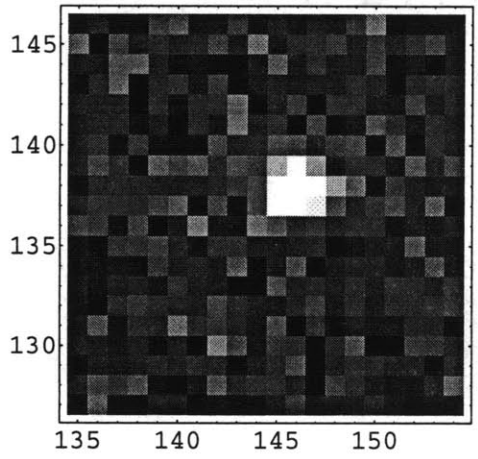

Figure 2.8 Sample Lick-LIRC2 image from the Triton occultation of Tr148A and Tr148B. This is the blended image of Triton-Tr148A-Tr148B. The data were recorded using a K' filter which has a center wavelength of 2.12 μm and a FWHM of 0.34 μm. The instrument does not read out subframes, so there is significant deadtime between integrations while the detector is read out.

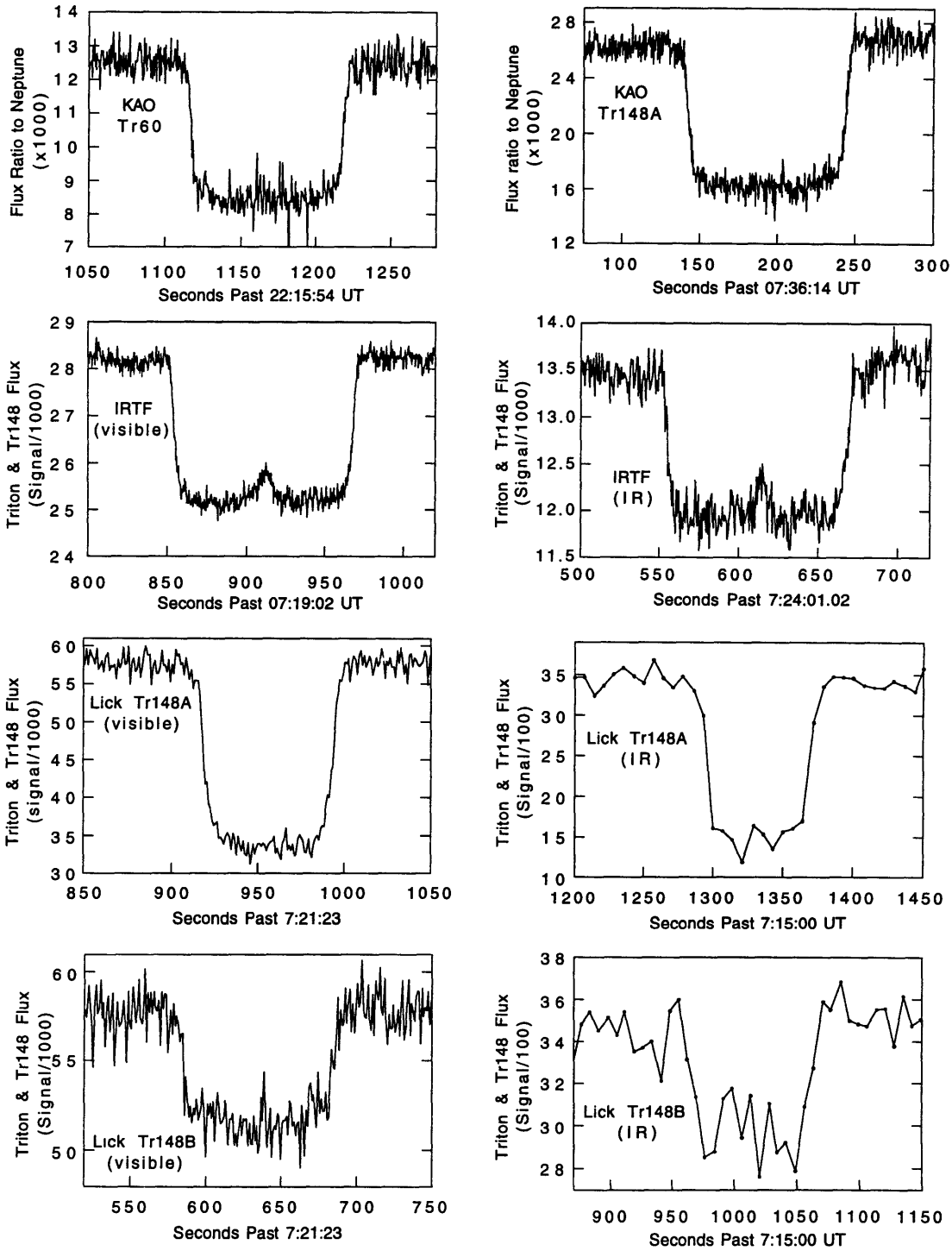

Figure 2.9 Unnormalized Triton light curves. The KAO light curves were constructed by PSF model fitting and their ordinate is the flux of the blended Triton-star image to Neptune. The other light curves were derived from aperture photometry and the ordinates are the signal of the blended Triton-star image above the background.

2.4 Post-Event Photometry

The photometric calibration of an occultation light curve establishes the signal levels corresponding to the full- and zero-flux levels of the occulted star. In a normalized light curve, the full-flux level of the occulted star is set to one and the zero-flux level of the occulted star is set to zero.

We used two methods to calibrate the occultation light curves. One uses conventional photometric techniques (*i.e.*, aperture photometry or PSF model fitting) to determine the relative intensity of the star to Triton and then calculates the background level. The other method uses the background level from isothermal model fits. This second method assumes (i) the atmosphere is isothermal and (ii) extinction is not contributing to the bending of the starlight.

The unnormalized signal in the Tr60 light curve is the intensity ratio of the blended Tr60-Triton image to Neptune. We define the background flux level of an occultation light curve s_b to be the flux level corresponding to zero flux from the occulted star. For this event, this is the intensity ratio of Triton to Neptune. From numerical PSF model fitting of 146 subframes containing Neptune and Triton (but not Tr60) recorded on the night of the occultation, we established the relative intensity of Triton to Neptune to be 0.00781 ± 0.00004. The image series was recorded in the same mode as the occultation. In Chapter 5, we will compare this result with the fitted level of the background from isothermal model fits.

For the photometric calibration of the 1995 Triton light curves, we need to know the relative magnitude of Triton to each of the stars (Tr148A and Tr148B). From post-event photometry (when Tr148 and Triton were separated), we can determine the relative intensity of the blended star to Triton (r_1 = Tr148AB/Triton). In Chapter 5, we will determine the relative intensity of Tr148A to Tr148B by isothermal model fits to the Lick Tr148A and Tr148B light curves. In this section, we will present the determination of r_1 from images recorded on the night of the occultation.

From post-event images recorded at the IRTF, KAO and Lick Observatory, we derived four values of r_1 (Tr148AB/Triton, see Table 2.2). The value of r_1 in the near-infrared is different from the others; this is not surprising. However, there is significant disagreement between the values of r_1 determined from the unfiltered CCD imaging. Reasons for the differences will be discussed below. First, we will discuss the data and the photometric methods used to determine r_1.

In the Lick-SNAPSHOT data, Triton and Tr148 were sufficiently separated such that aperture photometry could be used to retrieve the intensity ratio from the 30 minute

occultation-mode imaging series. The intensity ratio shows no trend over the 1800 subframes. From the IRTF-PCCD observations, the intensity ratio of the two sources was determined from numerical PSF model fitting. The blended image of Tr148A-Tr148B was used as the reference PSF and both sources (Triton and the blended star) were fit to a two-source model with sloping background. A different approach was taken with the post-event KAO data because of the scattered light from Neptune and the larger seeing. A three-source numerical PSF model (for Neptune, Triton and the blended Tr148) with sloping background was fit to the KAO subframes using Neptune as a reference PSF. For the IRTF-NSFCAM data, the intensity ratio was determined from aperture photometry when the images were separated.

Table 2.2 Intensity of Tr148AB/Triton

Site	Instrument	Filter	r_1
IRTF	MIT PCCD	None	1.560 ± 0.020
IRTF	NSFCAM	K	3.146 ± 0.035
KAO	Ames PCCD	None	1.2315± 0.0069
Lick	SNAPSHOT	None	1.4412 ± 0.0015

The three visual-wavelength determinations of r_1 (the intensity ratio of the blended star to Triton) disagree by significantly more than one standard deviation. The observations were all recorded with no filter in frame-transfer mode. The IRTF and KAO observations were both recorded with PCCD instruments. From the different quantum efficiency responses of the PCCD and SNAPSHOT detectors and the different altitude of the observations, we expect only a 1% difference in the ratio from the PCCD instrument relative to the ratio from the SNAPSHOT instrument. This does not account for all the differences seen in Table 2.2. The KAO value for the ratio is 14% smaller than the Lick value and the IRTF determination is 8 % larger.

Other reasons for the differences in r_1 could account for more change. The first is scattered light from Neptune biasing the photometry. When Triton (or the star) is near Neptune, the background level is contaminated with scattered light from Neptune. This can inflate or deflate the flux from Triton (or the star) depending on how the background is modeled. This is especially important when the seeing disk is large, as it is for observations from the KAO.

The second reason is only applicable to the IRTF-PCCD occultation data. Part of the field of view of the detector was vignetted (*i.e.*, part of the optical path was blocked,

see Appendix III). We can estimate the extent of the vignetting by examining an image of an evenly illuminated field (flat field). We see a gradient in the signal in the flat-frames (left panel of Figure 2.10) at the location of the subframe where the occultation was recorded. The variation across the subframe is about 13% of the signal (above the bias level). The subframe used for separate photometry of Triton and the star was ~15 pixels away from the subframe that recorded the occultation. The response of the two subframes to an evenly illuminated field is different (see Figure 2.10) due to the vignetting.

Neither the reduction of occultation image series nor the post-event photometry series had the flat-field response removed. The standard method for removing the flat-field response is not applicable to data recorded in frame-transfer mode because of the signal accumulated in the frame-transfer region. An appropriate technique for removing this uneven response is not currently known. However, this uneven response does not bias the occultation observations because the entire occultation takes about two minutes and the motion of blended Triton-Tr148 image across the detector in five minutes around the occultation time is about one pixel. Also, in the analysis of these occultation data, we allow for a linear trend in the observed flux with time, which would be the effect (to first-order) of the image moving across this vignetted field.

This non-uniform flat-field response does affect the photometric calibration of the zero-flux level because the post-event photometry was recorded in a different part of the detector. In Chapter 5, we will present another method for performing this calibration.

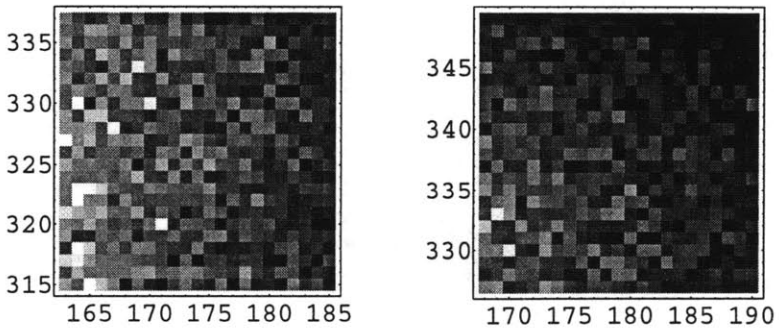

Figure 2.10 Two subframes from an image of an evenly illuminated field. The subframe on the left is area used to record the Triton occultation of Tr148B, while that on the right was used to record post-event images. The signal levels displayed are the same on the two subframes (black = 1300 ADU and white = 1500 ADU above the bias level).

3. Single-Chord Occultation Astrometry[2]

3.1 Introduction

From an occultation observation, one can learn about planetary rings and atmospheres with kilometer-scale spatial resolution (Elliot 1979), but to use these data requires accurate knowledge of the location of the observed chord relative to the center of the occultation shadow. This must be known with an accuracy (ideally better than a few kilometers) such that the uncertainty introduced by astrometric errors into the physical parameters derived from the light curve is smaller than their formal errors from model fitting. The most reliable method for determining the location of an occultation chord relative to the center of the shadow has been to use the immersion and emersion times from a set of occultation chords to fit a two-dimensional figure to the body shadow (see Chapter 4 for an application of this method to the 1995 Triton occultation data). For the giant planet atmospheres, which are rapidly rotating, an oblate figure is fit to the "half-light" times (French *et al.* 1985; Baron *et al.* 1989). For a slowly rotating atmosphere, such as Pluto, a spherical model is adequate (Millis *et al.* 1993). For large, airless bodies, such as Pallas, an elliptical figure has been used (Wasserman *et al.* 1979), but with a larger number of chords, more details can be inferred about the figure of the body (Dunham *et al.* 1990).

Other methods for determining the location of the occultation chord relative to the center of the occultation shadow include (for Saturn and Uranus) using ring occultations to establish the astrometry and learn where in the atmosphere the chord probed (Baron *et al.* 1989; Nicholson *et al.* 1995), since the orbits of the rings are known quite accurately (French *et al.* 1988; Elliot *et al.* 1993). Also, a central flash can be used to establish the position of a single chord (Lellouch *et al.* 1986). Finally, one can use the length of the chord along with the known figure of the body at a specific pressure level (Sicardy *et al.* 1991) to achieve the same end. However, in using that method, one must assume that the atmospheric structure is the same at the time for which the figure was established and at the time of the single-chord observation.

---

[2]This chapter is based on Olkin, C. B., J. L Elliot, S. J. Bus, S. W. McDonald, C. C. Dahn, (1996) Astrometry of single-chord occultations: Application to the 1993 Triton event, Publ. Astron. Soc. Pacific, 108:202-210.

For the Triton occultation presented here, we have only one observed chord (from the KAO), so the standard method of fitting immersion and emersion times from multiple chords cannot be used for the astrometric calibration. We were fortunate to obtain high-quality astrometric data to predict the occultation. These data produced such an accurate prediction that we were led to investigate just how well they could be used in a post-event analysis, especially since additional data were recorded the night after the occultation as well.

We refer to the method presented here as the *ephemeris method* for reasons that will become apparent. We make the basic assumption that stars do not move significantly over a time span of a few days and use a common set of field stars to define a reference system (in detector coordinates) across all frames. We can use the occulting body's ephemeris to set the scale in right ascension and declination. With this approach we do not have to reconcile two or more systems of celestial coordinates (the occulting body's ephemeris and that of an astrometric network), and we are immune to scale errors that must be present at some level in an astrometric network.

We shall first describe the method for determining the placement of the observed chord relative to the center of the occulting body from astrometric data. The next section describes the observations and details of the astrometric and photometric calibration for the Tr60 occultation (McDonald and Elliot 1992). Finally, we present a discussion of the error and considerations for application of this method to future occultations.

3.2 Overview of the Ephemeris Method

The method outlined here can be applied to CCD stare frames, CCD strip scans or photographic plates. Some of the frames (or plates) should contain the occulting body and occulted star both before and after the occultation event. Additional frames, without the occulting body, can be used to reduce the error in the occulted star center, but this is not typically the leading source of error. Also, for best results (highest precision) the mean center of the occulting body observations should be as close to the occulted star center as possible.

This chapter deals solely with the reduction of stare frames. This analysis could be applied to strip scans, but the low frequency errors in the star positions (Dunham *et al.* 1991) would have to be removed first. Strip scan data used for the occultation prediction were not used in this analysis because of a field distortion found in the data (Dunham, personal communication).

The ephemeris method is based on three assumptions. The first is that the field stars used for the common reference system are fixed (over the time scale of the observations–a few days). The second assumption is that the occulting body's motion can be used to set the scale in right ascension and declination. The ephemeris does not have to be correct in terms of absolute coordinates because we are only interested in relative positions. The final assumption is that displacements of observed positions of the stars and occulting body relative to the mean centers (the centers of the stars without displacing effects such as refraction and aberration) can be removed by a linear registration. We will break up the sources of these displacements into two categories: (i) known effects such as refraction, diurnal aberration, annual aberration, and general relativistic bending, and (ii) unknown, non-linear effects such as field distortion of the telescope, detector distortion, non-uniform thermal distortion or significant chromatic differential refraction.

In the following discussion, we use the term *registration* of a set of positions to a coordinate system to mean a least-squares fit that determines the linear transformation coefficients [which we shall also call *registration coefficients*; see Eq. 3.2 below].

This analysis is based on the construction of a common reference system–the *detector network*, which is the weighted average of the centers of each field star chosen for the reference system. Even if some frames are missing reference stars (due to poor seeing, or inconsistent centering causing stars at the edges to be lost), the mean frame can still be constructed. Each frame is linearly registered to the detector network to transform the occulted star and occulting body centers to a common reference system. The origin of this system is shifted to be the weighted mean center of the occulted star. Next, the scale and center of the detector network are related to celestial coordinates through a linear registration of the occulting body centers to the ephemeris. This allows us to determine the right ascension and declination of the occulted star in the coordinate system defined by the body's ephemeris. From here, we can determine the closest approach of the occulting body to the star and therefore, the placement of the occultation chord relative to the center of the body's shadow.

3.3 Description of the Method

In this section we present the method in detail. First, one establishes a set of stars that are common to all N_f frames and determines their centers by a suitable procedure. To be definite, we shall refer to CCD data and the row and column center of the nth star in the kth frame as (r_{nk}, c_{nk}). For photographic plates, one might choose a different

notation. For the kth frame, the row and column coordinates of the occulted star are denoted by (r_{*k}, c_{*k}), and those for the occulting body (in many cases, a "planet") by (r_{pk}, c_{pk}).

3.3.1 Creating the Detector Network

A common coordinate system for all the frames is needed, so a detector network is created from the weighted average position for each of the selected field stars. We weight the data by frame, since the frames are not necessarily the same quality due to varying observing conditions (seeing, airmass). For the data used here, the errors in the star positions appear to be the same for a single frame, independent of stellar magnitude (over the magnitude range of 12.6 to 18.7 from a yellow photographic emulsion, kindly supplied by A. Klemola). For this case, the weights, w_{rk} for the rows and w_{ck} for the columns, are derived from a registration of each frame to an unweighted detector network. For the nth star we find its coordinates in the unweighted detector network by the weighted averages (with all the weights set equal to 1):

$$\bar{r}_n = \frac{\sum_{k=1}^{N_f} w_{rk} r_{nk}}{\sum_{k=1}^{N_f} w_{rk}}$$
$$\bar{c}_n = \frac{\sum_{k=1}^{N_f} w_{ck} c_{nk}}{\sum_{k=1}^{N_f} w_{ck}} \qquad (3.1)$$

Then each frame is registered to the unweighted detector network, so that the reciprocal of the variance of the row and column residuals from the least-squares fit can be used as the row and column weights for each frame, and Eq. 3.1 is used a second time. The result is the detector network.

For each frame, the row and column positions of the network stars are registered to the detector network to determine the registration coefficients, a.

$$r_{rnk} = a_{1k} + a_{2k} r_{nk} + a_{3k} c_{nk}$$
$$c_{rnk} = a_{4k} + a_{5k} r_{nk} + a_{6k} c_{nk} \qquad (3.2)$$

The observed row and column centers for the occulting body and occulted star are transformed to the detector-network coordinate system with the registration coefficients found in Eq. 3.2. The resulting occulting body coordinates for the kth frame are denoted

by (r_{rpk}, c_{rpk}). Similarly, the occulted star coordinates in this detector-network system are (r_{r*k}, c_{r*k}).

3.3.2 Relating the Mean Frame to Celestial Coordinates

Since the row-column coordinates of the detector are in a plane, we convert the celestial coordinates of right ascension and declination (RA, α, and Dec, δ) to those in a plane tangent to the celestial sphere (assumed parallel to the detector). The optical axis of the telescope intersects the mean-frame coordinate system at the center of the detector which correspond to celestial coordinates (α_o, δ_o). Here we introduce the *tangent plane*, as defined by Smart (1977), that has the coordinate ξ parallel to RA and η parallel to Dec. The conversion equations between (α, δ) and (ξ, η) are (Smart 1977):

$$\xi = \frac{\cos\delta \sin(\alpha - \alpha_o)}{\sin\delta_o \sin\delta + \cos\delta_o \cos\delta \cos(\alpha - \alpha_o)}$$
$$\eta = \frac{\cos\delta_o \sin\delta - \sin\delta_o \cos\delta \cos(\alpha - \alpha_o)}{\sin\delta_o \sin\delta + \cos\delta_o \cos\delta \cos(\alpha - \alpha_o)} \qquad (3.3)$$

As previously mentioned, we use the body's ephemeris to establish the (α, δ) system. The ephemeris should be topocentric (*i.e.*, it included effects of geocentric parallax) and include a correction for light travel time, but may or may not contain corrections for diurnal and annual aberration (see Sec. 3.4, "Application to the Tr60 Occultation"). Due to our third assumption (that the effects of refraction, diurnal aberration, annual aberration and other displacements of the star centers can be removed by a linear registration), these corrections can either be included or not, since they will not make a difference in the resulting relative position of the occulting body and occulted star.

We generate right ascension and declination of the occulting body (α_{ek}, δ_{ek}) from the ephemeris at the midtimes t_k, of the frames where the subscript "e" stands for ephemeris. From (α_{ek}, δ_{ek}) we use Eq. 3.3 to calculate the tangent-plane coordinates (ξ_{ek}, η_{ek}) for the occulting body as given by the ephemeris. The registration of these tangent-plane coordinates to the occulting body's positions in the detector-network coordinate system provide the transformation to celestial coordinates (as defined by the ephemeris of the body).

We center this transformation on the occulted star. To do this we form the weighted average row and column position in the detector-network system. We denote this center by $(\langle r_{r*k} \rangle, \langle c_{r*k} \rangle)$, and it is computed with the weights (w_{rk}, w_{ck}). This shift of origin does not change the solution; it only simplifies later equations (Eqs. 3.5 and 3.8).

We perform a linear least-squares fit of the body observations in the detector-network system to the ephemeris positions and solve for the registration coefficients (b), see Eq. 3.4. This least-squares fit is performed with the appropriate weights, (w_{rk}, w_{ck}).

$$\begin{aligned}\xi_{ek} &= b_1 + b_2\left(r_{rpk} - \langle r_{r*k}\rangle\right) + b_3\left(c_{rpk} - \langle c_{r*k}\rangle\right) \\ \eta_{ek} &= b_4 + b_5\left(r_{rpk} - \langle r_{r*k}\rangle\right) + b_6\left(c_{rpk} - \langle c_{r*k}\rangle\right)\end{aligned} \tag{3.4}$$

Given the registration parameters of Eq. 3.4, the tangent plane coordinates of the occulted star can be easily calculated:

$$\begin{aligned}\xi_* &= b_1 + b_2\left\langle r_{r*k} - \langle r_{r*k}\rangle\right\rangle + b_3\left\langle c_{r*k} - \langle c_{r*k}\rangle\right\rangle = b_1 \\ \eta_* &= b_4 + b_5\left\langle r_{r*k} - \langle r_{r*k}\rangle\right\rangle + b_6\left\langle c_{r*k} - \langle c_{r*k}\rangle\right\rangle = b_4\end{aligned} \tag{3.5}$$

Now we can calculate the right ascension and declination of the occulted star using the transformation from tangent plane to celestial coordinates given by Smart (1977):

$$\begin{aligned}\tan(\alpha_* - \alpha_o) &= \frac{\xi_*}{\cos\delta_o - \eta_* \sin\delta_o} \\ \tan\delta_* &= \frac{\sin\delta_o + \eta_* \cos\delta_o}{\cos\delta_o - \eta_* \sin\delta_o}\cos(\alpha_* - \alpha_o)\end{aligned} \tag{3.6}$$

This is the end result of our astrometric reductions. From here, the shadow path can be determined by the star's right ascension and declination and the planet's ephemeris (the same one used in the registration above).

3.3.3 Calculating the Impact Parameter and Time

To calculate the impact parameter (or closest approach distance between the star and occulting body) we define a Cartesian coordinate system (*fgh*), with its origin at the center of the Earth, with *f* pointing in the direction of increasing right ascension and *h* pointing to the occulted star (Elliot *et al.* 1993). We construct the *fgh* coordinates of any object by creating its *XYZ* position from the object's right ascension, declination and distance, *D*, and then rotating the *XYZ* coordinates to *fgh*. The rotation matrix to convert from *XYZ* to *fgh* is a function of the right ascension and declination of the occulted star (Elliot *et al.* 1993). The conversion from the (ξ, η) plane to the (f, g) plane for an object at a distance D is $f = D\xi$ and $g = D\eta$ when the same center, (α_o, δ_o,) is used as the origin for each coordinate system.

To find the geocentric impact parameter, we convert a geocentric planet ephemeris (with a light-travel time correction) to *fgh* coordinates. In this coordinate system, we define the impact parameter, p, as the minimum distance between the center of the

occulting body's shadow and the observer. In the *fgh* system, $f_o(t)$ and $g_o(t)$ are the coordinates of the observer (Elliot *et al.* 1993), and $f_p(t)$ and $g_p(t)$ are the coordinates of the center of the occulting body's shadow as a function of time. The impact parameter is given by:

$$p = \mathrm{Min}\left\{\sqrt{\left[f_o(t) - f_p(t)\right]^2 + \left[g_o(t) - g_p(t)\right]^2}\right\} \tag{3.7}$$

The minimization denoted by Eq. 3.7 gives the impact parameter, and the time of the minimum is the predicted closest approach time. The latter can be compared with the midtime of the occultation light curve as a test of the astrometric solution.

3.3.4 Errors

Here we calculate the errors in the impact parameter and occultation midtime, according to the assumptions of our astrometric reduction procedure. We begin with the errors expressed in the tangent plane—derived from Eq. 3.5, in which ξ_* and η_* are each expressed as a sum of three terms. There is no correlation between the offset term (b_1) and the slope terms (b_2 and b_3) due to the choice of $(\langle r_{r*k}\rangle, \langle c_{r*k}\rangle)$ as an offset for the registration. Also, the two slope terms are assumed to be uncorrelated because they are in orthogonal directions. We denote the variance of the sample means $\langle r_{r*k}\rangle, \langle c_{r*k}\rangle$ by $\sigma^2\left(\langle r_{r*k}\rangle\right), \sigma^2\left(\langle c_{r*k}\rangle\right)$. Taking the appropriate partial derivatives, we find that the variances $\sigma^2(\xi_*)$, $\sigma^2(\eta_*)$ are:

$$\begin{aligned}
\sigma^2(\xi_*) &= \sigma^2(b_1) + b_2^2\sigma^2\left(\langle r_{r*k}\rangle\right) + b_3^2\sigma^2\left(\langle c_{r*k}\rangle\right) \\
\sigma^2(\eta_*) &= \sigma^2(b_4) + b_5^2\sigma^2\left(\langle r_{r*k}\rangle\right) + b_6^2\sigma^2\left(\langle c_{r*k}\rangle\right)
\end{aligned} \tag{3.8}$$

We can gain some understanding of these errors by considering a case where the ξ axis is perfectly aligned with the row axis so that $b_3 = b_5 = 0$. We work only with the equation for ξ, since the η result is completely analogous. Using the equations for linear-least squares (Clifford 1973), we can write an expression for the variance of b_1 in Eq. 3.8 in terms of the row weights, w_{rk}, the measurements of the occulting body's position, $\xi_e(t_k)$, and the scale factor in radians per pixel, b_2. First, we define the ephemeris position in the detector-network system:

$$r_{re}(t_k) = \frac{\xi_e(t_k)}{b_2} + \langle r_{r*k}\rangle \tag{3.9}$$

The variance of the sample mean of the star and the equivalent quantity for the occulting body (this is equal to the variance of the residuals from the ephemeris

registration expressed in units of pixels instead of radians) are given in Eqs. 3.10 and 3.11. These are the variances based on the scatter; internal errors can be calculated from the weights alone, by Eq. 3.31 of Bevington (1992). Note the denominators differ because there is one less degree of freedom for the occulting body than the star because a line was fit through the data, whereas for the star only a mean was determined.

$$\sigma^2\left(\left\langle r_{r*k}\right\rangle\right) = \frac{\sum_{k=1}^{N_f} w_k\left(r_{r*k} - \left\langle r_{r*k}\right\rangle\right)^2}{(N_f - 1)\sum_{k=1}^{N_f} w_k} \tag{3.10}$$

$$\sigma^2\left(\left\langle r_{rpk}\right\rangle\right) = \frac{\sum_{k=1}^{N_f} w_k\left(r_{rpk} - r_{re}(t_k)\right)^2}{(N_f - 2)\sum_{k=1}^{N_f} w_k} \tag{3.11}$$

It is possible that all the frames do not have usable positions for both the occulting star and occulted body (for example, if the occulting body passes too close to a field star in one night's data). If this is the case, then the number of frames, N_f, for the star and occulting body will not be the same, and care is required to implement Eqs. 3.10 through 3.12 with the proper sums.

The error in the offset term, b_1 is

$$\sigma^2(b_1) = b_2^2\sigma^2\left(\left\langle r_{rpk}\right\rangle\right)\left\{\frac{N_f\sum_{k=1}^{N_f} w_{rk}\left(r_{rpk} - \left\langle r_{r*k}\right\rangle\right)^2}{\sum_{k=1}^{N_f} w_{rk}\sum_{k=1}^{N_f} w_{rk}\left(r_{rpk} - \left\langle r_{r*k}\right\rangle\right)^2 - \left[\sum_{k=1}^{N_f} w_{rk}\left(r_{rpk} - \left\langle r_{r*k}\right\rangle\right)\right]^2}\right\} \tag{3.12}$$

If we denote the factor in curly braces by γ_r^2, then we can write (for our ideal case) equations for the variance in both ξ_* and η_*:

$$\begin{aligned}\sigma^2(\xi_*) &= b_2^2\left[\gamma_r^2\sigma^2\left(\left\langle r_{rpk}\right\rangle\right) + \sigma^2\left(\left\langle r_{r*k}\right\rangle\right)\right] \\ \sigma^2(\eta_*) &= b_6^2\left[\gamma_c^2\sigma^2\left(\left\langle c_{rpk}\right\rangle\right) + \sigma^2\left(\left\langle c_{r*k}\right\rangle\right)\right]\end{aligned} \tag{3.13}$$

Eq. 3.13 shows how the errors in the measured occulting body and occulted star positions translates into errors in ξ_* and η_*. Both terms in each equation partake of a common scale factor (b_2 or b_6), and the variance in the sample means add quadratically. However, we see that the γ factors enhance the variance due to the error in the measured body

positions, increasing as the distance between the mean of the body positions is more distant from the star.

The error in the impact parameter is the error of the star position projected onto a line connecting the star at the time of closest approach to the center of the occulting body. If θ is the position angle of the star relative to the center of the body (measured from North through East) at the time of closest approach, then the error in the impact parameter (in kilometers) is given by Eq. 3.14, where d is the distance (in kilometers) from the observer to the occulting body.

$$\sigma(p) = D\sqrt{\sigma^2(\xi_*)\sin^2\theta + \sigma^2(\eta_*)\cos^2\theta} \tag{3.14}$$

Similarly, the timing error is the error component perpendicular to this, divided by the shadow velocity, v, at the midtime of the occultation:

$$\sigma(t_o) = \frac{D}{v}\sqrt{\sigma^2(\xi_*)\cos^2\theta + \sigma^2(\eta_*)\sin^2\theta} \tag{3.15}$$

3.4 Application to the Tr60 Occultation

For the Tr60 occultation by Triton, 20 CCD frames of the star field were taken on the nights of 1993 July 8-11 with the 61-in astrometric reflector at the USNO Flagstaff Station. The detector is a Tektronix, thinned, back-side illuminated, 2048x2048 CCD with an image scale of about 0.325 arcsec per pixel (field of view equal to 11 arcmin). These frames were exposed through a broadband red filter (USNO designation A2-1, with a passband of 6600-8300 Å). Typical exposure times for the frames were 60 seconds (longer exposures could not be taken because Neptune would saturate).

Images with known systematic errors were not included in the analysis. The data selection process removed centers of either field stars, Tr60, or Triton from the analysis; sometimes entire frames were removed. Triton centers were removed either because of high residuals in the ephemeris registration (this was the case for 2 centers) or because Triton was merged with a field star (18 of the Triton centers from July 10 were not included in the analysis for this reason). More detailed modeling of the two sources may provide accurate astrometry and photometry, but for now these data are not included. Two field stars were not included in the analysis because they were too close to the edge of the CCD (less than 20 pixels ≈ 7 arcsec) and showed high residuals in the registration. One frame was removed on the basis of photometry, since the magnitude difference between Tr60 and Triton was not consistent with the other frames from that night. Frames with thin cirrus as evidenced by inconsistent photometry, or field stars not

identified on all frames were also left out of the reduction. To reduce the effects of refraction and telescope flexure, the observations occurred within 1 hour of the meridian; see Table 3.1. There are 44 field stars that comprise the detector network (see Figure 3.1), common to all the 74 useful frames (Table 3.1).

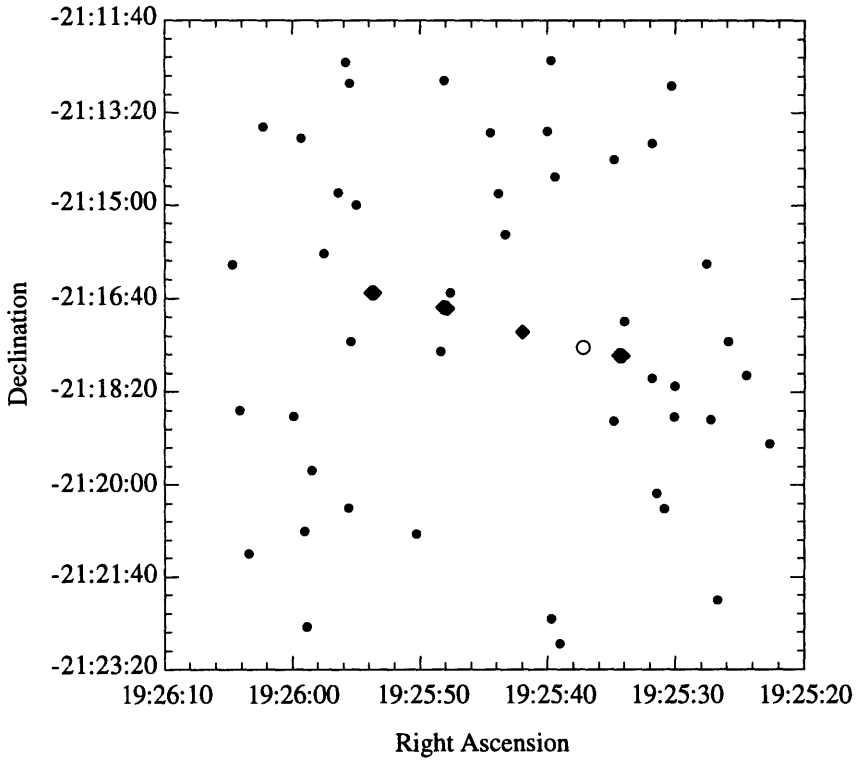

Figure 3.1 Tr60 field. The star field of the USNO stare frames is shown schematically. The 44 field stars used to construct the mean frame coordinate system are indicated by filled circles. The occulted star, Tr60, is shown by the open circle. The motion of Triton across the field is indicated by the diamonds for the first and last observation from each night. The usable observations on the third night covered a shorter time span, hence there is no noticeable motion from the first to the last observation. The USNO frames were all centered to within 3 arcsec. All coordinates are J2000.

Table 3.1 Tr60 Astrometric Data, RMS Error and Intensity Ratio

Date	# Frames	Min. HA	Max. HA	Tr60		Triton		Intensity Ratio
	(Tr60/Triton)	(hrs.)	(hrs.)	Row Error[a] $\sigma(\langle r_{r*k} \rangle)$	Col Error[a] $\sigma(\langle c_{r*k} \rangle)$	Row Error[a] $\sigma(\langle r_{rpk} \rangle)$	Col Error[a] $\sigma(\langle c_{rpk} \rangle)$	(Tr60/Triton)
1993 07 08	20/18	–0.72	0.62	0.022	0.059	0.016	0.040	0.5175 ± 0.0006
1993 07 09	20/20	–0.66	0.90	0.027	0.051	0.030	0.059	0.5267 ± 0.0005
1993 07 10	18/2	–0.81	0.53	0.065	0.076	0.069	0.091	0.5112 ± 0.0030
1993 07 11	16/16	–0.94	0.14	0.074	0.056	0.062	0.075	0.4824 ± 0.0009

[a] Errors are for an individual frame based on the scatter. Internal error agrees well with error from scatter. Units are pixels and the mean focal plane scale is about 0.325 arcsec/pixel.

3.4.1 Astrometry

Before we can apply our astrometric method to the data, we must calculate centers for the field stars, Triton and Tr60. This is done by putting the flattened frames through a series of IRAF scripts that use the functions in the DAOPHOT package (Stetson 1987) to perform numerical point-spread-function (PSF) fitting of the observed stars. First, the routine "daofind" is used to identify all stellar images on the frame that are within a given range of brightness (neither too faint to be in the noise, nor too bright to be in the non-linear regime of the detector). This program convolves the data with a Gaussian function, and then examines the convolved data for local maxima. Approximate centroids, as well as the roundness and sharpness of the image are calculated. These last two parameters are used to eliminate bright pixels, cosmic rays, and extended objects from the star list.

Next, aperture photometry of the stars identified by "daofind" is performed with "apphot". An IRAF script selects stars for the PSF which (i) are neither too bright nor too faint, (ii) are not near the edge of the frame, and (iii) do not have nearby neighbors. This selection is done on the basis of the aperture photometry and "daofind" results. The numerical PSF is fit to all identified stars with the DAOPHOT function "nstar" that uses a least-squares procedure to simultaneously fit stars that are close together. The result is the row and column center (r, c), instrumental magnitude, and error in the instrumental magnitude for each object. The resulting lists are edited to include only: (i) the occulted star, (ii) the occulting body, and (iii) the detector-network stars. Since the errors in the centers were independent of magnitude for the network stars, the weighting given by Eq. 3.1 was used.

We used the DE211 ephemeris to define the motion of the Neptune system's center of mass and the NEP016 model (Jacobson *et al.* 1991) to define the motion of Triton relative to the center of mass of the system. Triton's ephemeris was topocentric and included a correction for light travel time, but no adjustment was added for the apparent displacement due to diurnal aberration, annual aberration, and refraction.

One could add the effects of aberration and refraction to the ephemeris, but Table 3.2 shows that the unmodeled contribution of these effects is negligible. Values of the maximum image displacements are given in Table 3.2. For each effect we have selected the frame that would have the maximum image displacement and have calculated (i) mean displacements of the images for the frame, and (ii) the maximum part of the effect that would not be modeled by the linear registration of Eq. 3.2. For the effects of diurnal aberration, annual aberration, and monochromatic refraction, the appropriate angle over

which to propagate the unmodeled terms is half of the detector field of view. The mean image displacements due to chromatic terms in atmospheric refraction do not affect us, but the differential displacements due to this effect cause unmodeled trends in the positions of network stars that depends on their color. We have measured the colors for 13 of the 44 stars and have calculated the image displacements for a hypothetical star with the mean color. The maximum displacement (determined for the star with the most extreme difference in color and for the frame with the greatest hour angle) has been entered in Table 3.2. Although these image displacements would not be removed by the linear registration of Eq. 3.2, most are much smaller than the maximum given in the table, and they should be of random magnitude over the network. The signature of these errors would be a systematic trend of the registration residuals as a function of hour angle, but this trend was not apparent. From the entries in Table 3.2 we conclude that the linear approximation for these effects would not introduce significant errors into our analysis.

Table 3.2 Maximum Image Displacements in the USNO Frames

Effect	Mean for Frame (arcsec)	Not Modeled (arcsec)
Diurnal Aberration	0.26	$3.4\ 10^{-7}$
Annual Aberration	21.	$2.7\ 10^{-5}$
Refraction (monochromatic)	75.	$6.6\ 10^{-4}$
Refraction (chromatic)	0.015	$8.6\ 10^{-4}$

However, if one still wanted to add the effects of aberration and refraction to the ephemeris, care is needed to do this properly. First one needs to calculate the amount of the displacement of the Triton center on each frame, then the displacement added to the ephemeris is the weighted average displacements of each individual frame. This is needed to be consistent with the Triton centers in the detector network coordinate system. Each star's center in the detector network coordinate system has a net displacement (due to the effects in Table 3.2) equal to the weighted average of that star's displacement on all the frames.

The residuals from registering the Triton centers to the ephemeris are shown in Figure 3.2. The figure shows the residual of each Triton center as a function of its location in the detector network. The residuals have been multiplied by a factor of 100. Note that no systematic trends are evident. The weighted RMS residual is 0.001 arcsec in the ξ direction and 0.003 arcsec in the η direction.

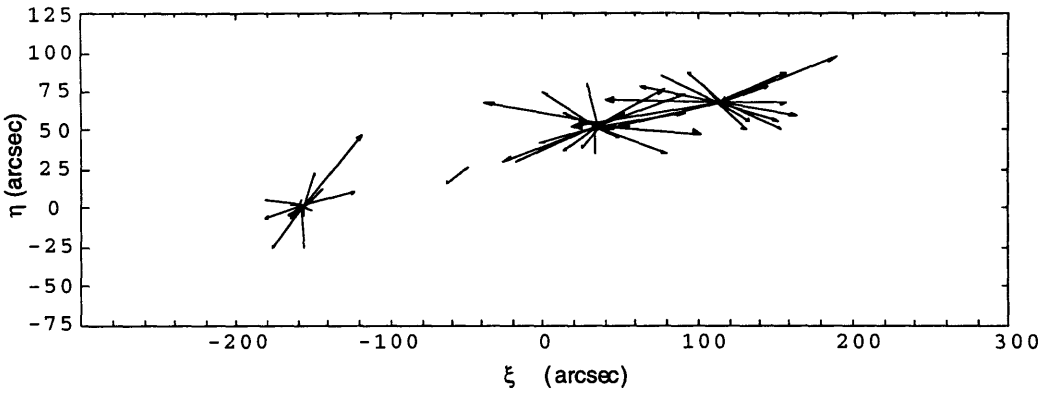

Figure 3.2 Triton registration residuals. The residuals in arcsec (multiplied by a factor of 100) from the registration of the Triton centers to the ephemeris are displayed. Each residual is indicated by a line whose origin is the Triton position for that frame.

The standard error of the Tr60 center and the equivalent for the Triton centers (as expressed in the error discussion) are listed for each night's observations in Table 3.1. As seen in the table, there is a nightly variation of the data quality. These numbers also show that the scatter in the Triton position is not inflated due to scattered light from Neptune.

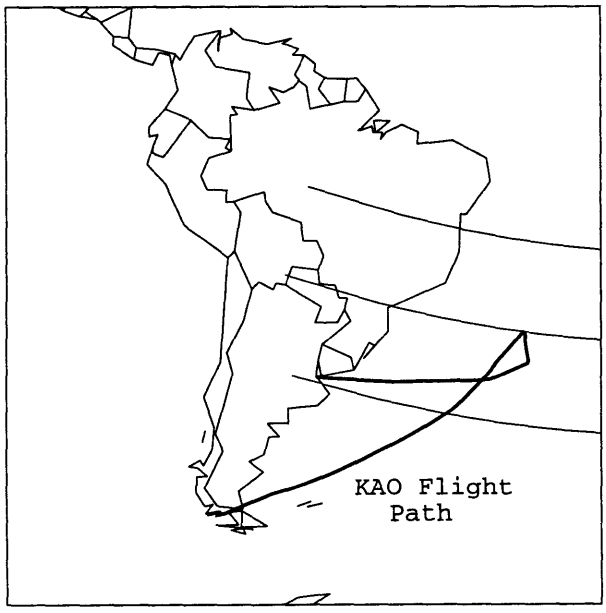

Figure 3.3 Triton's shadow path and the KAO. The northern limit, centerline and southern limit of Triton's shadow are shown as they crossed South America. The flight of the Kuiper Airborne Observatory, indicated by the bold line, starts at Punta Arenas, Chile and ends in Buenos Aires, Argentina. Occultation series images were obtained for 35 minutes around the occultation time on the south-bound leg of the flight.

Using the method described above, we derived a minimum distance for the KAO from the center of the shadow of 359 ± 133 km (0.017 ± 0.006 arcsec); the center of Triton's shadow was north of the KAO. Figure 3.4 shows the path of the star relative to Triton as seen from the KAO. As an independent check of the astrometric solution's

accuracy, we can compare the observed midtime of the occultation with the closest approach time from astrometry. For this event, the astrometric closest approach time was 2.2 seconds before the midtime from the light curve. This time difference is less than the formal error in the timing (3.1 sec) and translates to 60 kilometers (using Triton's shadow velocity of 27.37 km/s for the KAO), which is less than the formal error on the miss distance. The latitudes probed at the half-light level of immersion and emersion are also listed in Table 3.3. The full set of longitudes and latitudes probed by this occultation are displayed in Figure 3.5.

Table 3.3 Tr60 Occultation Circumstances

Impact Parameter for the KAO(km)	359 ± 133
Time Difference[a] (s)	2.2 ± 4.1
Impact parameter f component (km)	77 ± 111
Impact parameter g component (km)	-350 ± 134
shadow velocity for the KAO (km/s)	27.37
Immersion half-light longitude (deg.)	$74.0^{+2.2}_{-2.6}$
Emersion half-light longitude (deg.)	$231.1^{+3.8}_{-4.4}$
Immersion half-light latitude (deg.)	$-22.5^{+1.8}_{-1.5}$
Emersion half-light latitude (deg.)	$3.9^{+3.4}_{-3.9}$

[a]Light curve occultation midtime minus astrometric closest approach time.

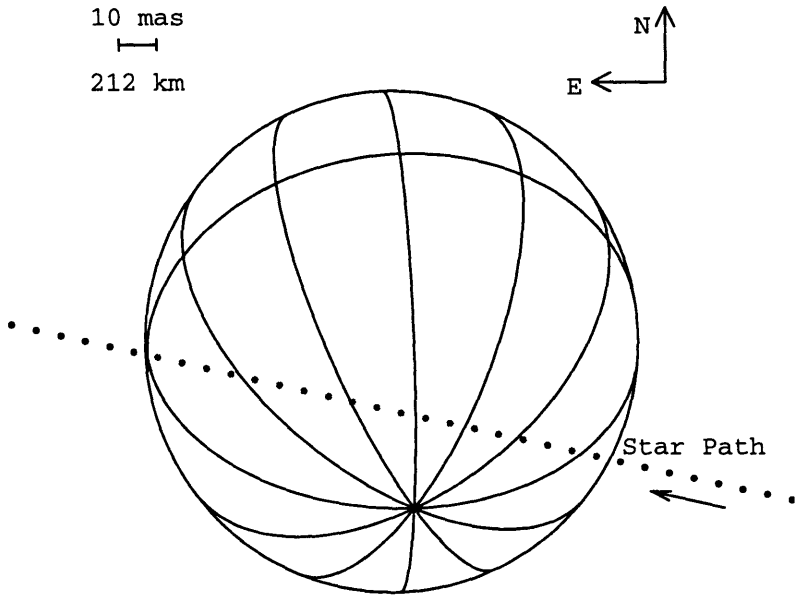

Figure 3.4 Triton as seen from the KAO. The path of the star as it is occulted by Triton is indicated at 5-second intervals. Triton's south pole is visible. The uncertainty in the star path is about 0.006 arcsec, or roughly half the scale bar.

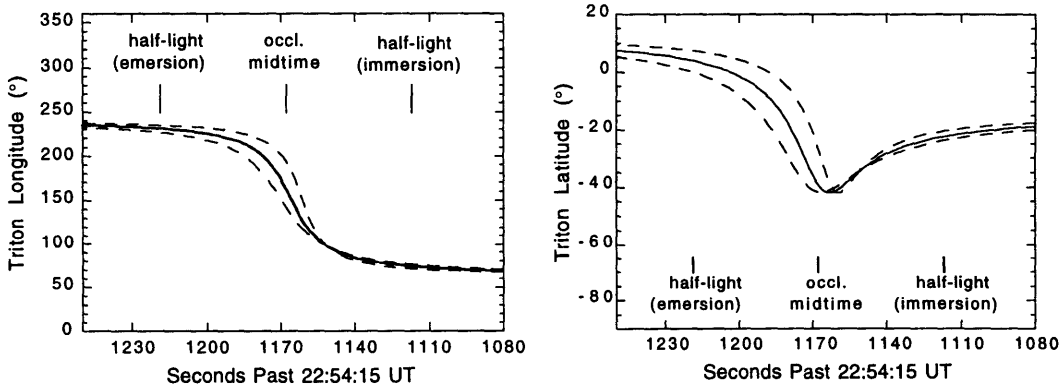

Figure 3.5 The longitude and latitude on Triton probed by this stellar occultation. The left panel shows the longitude of Triton that was probed as a function of time and the right panel shows the Triton latitude probed. The dashed lines indicate the ±1-standard-deviation limits on the latitudes probed. The time axis is reversed to be consistent with the path of the star in the previous figure. The midtime of the occultation, along with the half-light immersion and emersion times from the light curve are indicated. The occultation probed the southern hemisphere during the midtime of the occultation.

Figure 3.6 is a plot in the tangent plane of the residuals from the registration of the field stars to a secondary astrometric network supplied by A. Klemola (1993, personal communication). This network was a re-reduction (using the ACRS network) of plates

taken to search for Neptune candidates (Klemola and Mink 1991) originally reduced with the Perth 70 catalog. The residuals have been multiplied by a factor of 100 so that they are visible in the figure. Note that there are no obvious systematic trends in the residuals. Since we are concerned with only relative positions, systematic errors in the absolute position (which may not be apparent in this figure) are not relevant. The standard deviation of these residuals are 0.18 arcsec in the ξ direction and 0.13 arcsec in the η direction.

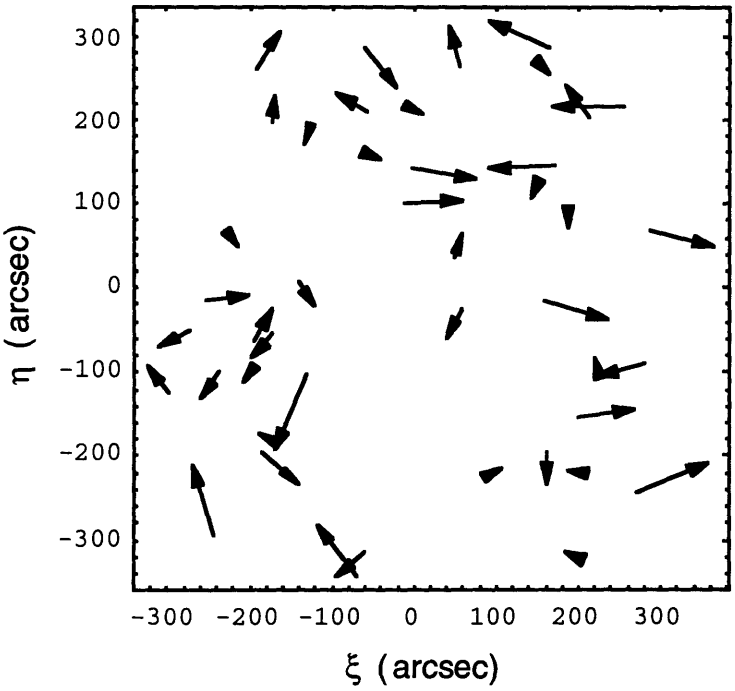

Figure 3.6 The residuals from registering the weighted mean frame to a secondary astrometric network. The residuals have been multiplied by a factor of 100. Each of the standard stars are indicated in the figure by their (ξ, η) components, and their residual components are indicated by the arrow.

3.4.2 Photometry

The accurate analysis of an occultation light curve relies not only on an astrometric calibration but on a photometric one, too. The photometric calibration involves determining the relative magnitudes of the occulted star and occulting body to define the zero-flux level of the light curve. For the Tr60 occultation, the relative magnitudes of the objects were derived from the same USNO data on which the astrometric solution is based. There were other sources of photometric data, but due to non-linearities in other detectors, these data are the best source for the photometric calibration.

The flux ratios of Tr60 to Triton on a nightly basis are listed in Table 3.1 and are displayed in Figure 3.7. There is variability in the relative intensities, either from variability in Triton as a function of rotational phase or from the variability of Tr60. To get the intensity ratio at the occultation time, we linearly interpolated using the last three nights of data (as defined by the midtime of the light curve). This photometric

determination of the relative intensities involves a different instrument and filter than the occultation observations. The effective wavelength of each system (KAO and USNO) was determined from the quantum efficiency of each detector and the filter (no filter was used for the KAO observations).

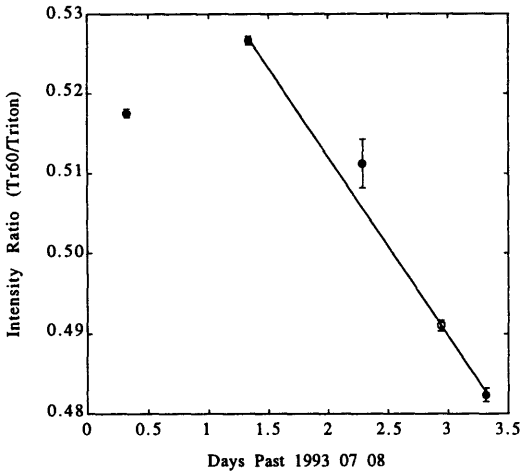

Figure 3.7 The relative intensity of Tr60 and Triton as a function of time. The filled circles indicate the intensity ratio for each night's observations with an error bar given by the standard error of the sample mean. There were only two good Triton observations on the third night, hence the error bar is larger. Also shown in the figure is the best fit line to the observations from the last three nights. The open circle represents the adopted intensity ratio measured with the USNO system for the time of the occultation.

The effect of refraction on the effective wavelength was ignored. The constant of refraction changes by less than 1% over the wavelength of the filter used at the USNO filter. At the altitude of the KAO, the atmospheric pressure is lower than sea level by about a factor of 5, and the change in refraction over the wavelengths of the instrument (the NASA/Ames Portable CCD) sensitivity is only 1%. R and I photometry of Tr60 ($R = 13.39 \pm 0.02$; $I = 13.82 \pm 0.02$; D. M. Chamberlain personal communication) and Triton (Buratti *et al.* 1994) provided the slope of the intensity ratio with wavelength from the effective wavelength of the USNO observations (0.65 μm) to the effective wavelength of the KAO observations (0.67 μm); see Table 3.4. The R and I magnitudes for Tr60 are approximately Kron-Cousins (M. Buie, personal communication).

Table 3.4 Tr60 Photometry

Dataset	effective λ (μm)	Intensity Ratio (Tr60/Triton)
USNO	0.67	0.4910 ± 0.0007
KAO	0.65	0.4895 ± 0.0012[a]

[a] derived from the USNO intensity ratio and the effective wavelengths.

3.5 Discussion

The method outlined in this chapter to determine the closest approach distance between a star and a body passing close by has been applied to the 1993 Triton occultation, and we find consistency between the closest approach time predicted by the astrometry and that derived from the occultation light curve. To the level of accuracy presented, we find no systematic problems with either the analysis or the data. Much of this is due to the high astrometric quality of the telescope and detector, as well as the practice of observing only when the objects are near transit.

Now we consider the sources of formal error. Note that choosing the occulted star for the origin of the detector-network coordinate system simplifies the error analysis, so that only the errors in the offset terms of the registration and the scatter of the star center (the two parts of Eq. 3.13) contribute. For this dataset, we are limited by the error in the registration coefficients ($\sigma(b_1) = 0.005$ arcsec and $\sigma(b_4) = 0.006$ arcsec), not the scatter in the Tr60 center (0.001 arcsec in ξ and 0.002 arcsec in η). Therefore, more observations of the star would not significantly improve the solution. Improving the precision of the solution could have been accomplished by (i) more observations of Triton (to reduce the registration coefficient error), which cannot be increased arbitrarily because the occulting body only spends a finite amount of time in the same field with the occulted star, and (ii) arranging the observations so that the mean Triton position was closer to the Tr60 position. If the mean Triton position were coincident with the Tr60 position, then the γ factor in Eq. 3.13 would have been unity and the error in the minimum separation would have been reduced from 0.006 to 0.003 arcsec. For this analysis, the effective mean Triton position was further from the Tr60 position than a simple (unweighted) average would indicate, because the first two nights' data (both recorded before the event) were of the highest quality.

Outer solar system bodies such as Triton and Pluto are on the same 11 arcminute field as a given candidate star for about one week at opposition. However, less remote bodies generally will move through the field more quickly, decreasing the window of opportunity for obtaining this critical calibration data. For the most accurate results, the observations should be taken both before and after the occultation, so that we can interpolate to derive the closest approach distance (rather than extrapolate) and to minimize the γ factor in Eq. 3.13.

This method provides the following two advantages in comparison to the standard astrometric reduction technique which is commonly used for occultation predictions (Wasserman *et al.* 1979). First, no astrometric network is needed. With CCD data, the

field is generally small enough that primary astrometric networks do not have a sufficient number of standard stars. Eliminating the need for the dense astrometric network saves significant time and effort. Second this method is immune to scale and rotation errors in an astrometric network that result from the random errors in the star positions and any systematic differences between the stellar reference frame and that of the ephemerides. We do not expect to find significant scale errors in the planetary motion (which sets the scale) as defined by ephemerides, because this error would accumulate over time and an offset of the body from its ephemeris would be noticed.

This method has the disadvantage that it cannot be used for all occultations. If the occulting body has a linear path across the detector, then the motion of the body can set the scale only in the direction of motion, and an astrometric network is needed to define the perpendicular scale. This "*compromise*" method was used in the 1994 March 9 occultation by Chiron (Elliot *et al.* 1995); see Appendix III for details.

Over time, this ephemeris method can be employed to determine a "catalog" of star positions in the reference frame of planetary ephemerides. This catalog could then be used to investigate differences between the reference system of ephemerides and stellar reference frames. Toward this end, we present three positions for Tr60 (all in J2000) based on three different astrometric reductions, see Table 3.5. These positions come from the ephemeris method and from astrometric reductions of plates (Klemola 1993, personal communication) for two separate primary astrometric networks: the ACRS and Perth 70. The coordinates of the detector-network stars are not given here because the right ascension and declination of these stars were not determined as accurately as Tr60 since Triton did not pass close to these other stars. Many of the stars would be outside of Triton's path, and the image scale would have to be extrapolated to their locations, which introduces errors.

Table 3.5 Tr60 Positions (J2000 FK5)

Reference System	RA	Dec
Triton ephemeris	19 25 37.227	–21 17 32.66
ACRS network	19 25 37.256	–21 17 32.70
Perth 70 network	19 25 37.205	–21 17 32.73

For the most precise determination of an occultation chord location, it is best to have well spaced, multiple chords. However, with occultations by small bodies it is not always possible to have multiple observers in the shadow path (due to the uncertainties

of the prediction, even a week in advance). Useful information can be derived from these single-chord occultation observations with the ephemeris method presented here, if there are quality astrometric data of the occulted star and occulting body both before and after the occultation.

4. Multiple-Chord Occultation Astrometry

For the Tr148A and Tr148B occultations, multiple occultation chords were observed. We shall use these chords (which are a one-dimensional scan across Triton's shadow) to accurately reconstruct where on Triton each chord probed.

First, we construct the shadow plane (also known as the *fg* plane). The origin of this plane is the center of the Earth and it is perpendicular to the line-of-sight to the star. See Elliot *et al.* (1993) for the definition of the *fgh* coordinate system. The $\hat{h}$ direction points to the occulted star and we assume the star is infinitely far away such that the unrefracted rays of light are all parallel to $\hat{h}$. The $\hat{f}$ direction points in the direction of increasing right ascension and the $\hat{g}$ direction completes the right-handed system. For this event, the $\hat{h}$ direction is defined by the coordinates of the blended star as determined by the Carlsberg Automatic Meridian Circle (J2000 $\alpha_* = 19^h41^m00^s.376$; $\delta_* = -20°51'41''.20$, B. Argyle, personal communication).

We used the DE211 ephemeris [supplied by JPL's Navigation Ancillary Information Facility (Acton 1990)] and the NEP016 model (Jacobson *et al.* 1991) to calculate a light-time corrected J2000 Triton ephemeris in celestial coordinates. The ephemeris is converted from right ascension, declination and distance (α, δ and D) to J2000 XYZ rectangular coordinates:

$$\begin{aligned} X &= D\cos\alpha\cos\delta \\ Y &= D\sin\alpha\cos\delta \\ Z &= D\sin\delta \end{aligned} \tag{4.1}$$

The XYZ coordinates are rotated to *fgh* using the matrix (Elliot *et al.* 1993) in Eq. 4.2. The resulting Triton shadow-plane coordinates $f_p(t)$ and $g_p(t)$ would define the center of the occultation shadow if there are no errors in the ephemeris and star position. We know the star position is not correct since we are using the coordinates of the blended star. We will solve for an offset to account for any errors in the star position or Triton ephemeris.

$$R_1 \equiv R_{XYZ\to fgh} = \begin{bmatrix} -\sin\alpha_* & \cos\alpha_* & 0 \\ -\cos\alpha_*\sin\delta_* & -\sin\alpha_*\sin\delta_* & \cos\delta_* \\ \cos\alpha_*\cos\delta_* & \sin\alpha_*\cos\delta_* & \sin\delta_* \end{bmatrix} \tag{4.2}$$

Next, we calculate the position of the observer in the shadow plane $f_r(t)$ and $g_r(t)$. The subscript r stands for receiver, following the notation of Elliot *et al.* (1993). The geodetic coordinates of the observing site are converted to J2000 XYZ rectangular

coordinates and then to *fgh* coordinates. Table 4.1 shows the WGS84 coordinates of the observing sites as measured by a GPS receiver. The errors for the IRTF, Lick, Lowell and WIRO sites are the scatter of a set of observations. For the KAO immersion and emersion coordinates, the error is the estimated precision from a single measurement (E. W. Dunham, personal communication). This may be an underestimate because of the variable bias inserted into the GPS signal.

Table 4.1 Geodetic Observatory Coordinates from GPS (WGS84)

Site	Longitude (°:':")	σ(long.) (arcsec)	Latitude (°:':")	σ(lat.) (arcsec)	Altitude (m)	$\sigma_{alt.}$ (m)
IRTF	-155:28:20.	2.0	19:49:34.	3.0	4182.	75.
KAO[a]	-157:30:50.	1.0	32:36:10.	1.0	13004.	30.
KAO[b]	-157:42:55.	1.0	32:32:28.	1.0	12949.	30.
Lick	-121:38:38.9	0.2	37:20:17.7	0.2	1241.	7.
Lowell	-111:32:10.6	0.2	35:05:48.7	0.3	2209.	5.
WIRO	-105:58:38.1	0.6	41:05:50.0	0.6	2956.	21.

[a]immersion
[b]emersion

The position of the observer relative to the shadow center at a time t is given by Eq. 4.3, where f_o and g_o account for error in the planet's ephemeris or star's coordinate. The subscript p stands for the ephemeris position and p' stands for the corrected position.

$$f_{p'r}(t) = f_r(t) - \left(f_p(t) - f_o\right)$$
$$g_{p'r}(t) = g_r(t) - \left(g_p(t) - g_o\right) \tag{4.3}$$

At a given stellar-flux level the observers are probing the same pressure level in Triton's atmosphere. We choose the half-light level (when the occulted star's flux is down by 50%) to be our reference level and calculate $f_{p'r}$ and $g_{p'r}$ at the times of half-light. The immersion and emersion times at the half-light level are derived from isothermal model fits (assuming no extinction) to the occultation light curves, see Table 4.3 for the fitted half-light times. The isothermal model is an extension of Elliot and Young (1992) to include the flux contribution from the far limb and will be presented in Chapter 5.

To establish the closest approach distance of an observer from the center of the shadow, we fit a model of Triton's figure to the positions of the observer relative to the shadow center ($f_{p'r}$ and $g_{p'r}$) at the immersion and emersion half-light times. We assume a

spherical model for the figure of Triton's atmosphere at the half-light level. Other options for the figure of Triton include an oblate spheroid. The oblate model was not used based on an estimate of the planetary atmosphere's oblateness. Assuming Triton is a Maclaurin spheroid (an incompressible fluid of constant density), then the oblateness is $5q/4$ where q is the ratio of its centrifugal acceleration to its gravitational force (Hubbard 1984). This gives a difference between the equatorial and polar radii of 0.6 km–too small to be detected by these occultation timings.

The free parameters in the fit are the shadow-plane half-light radius, and an offset (in f and g) for each of the stars. The fit is weighted using the formal errors from the half-light timings (see Table 4.3) because the light curves are of different quality. The fitted half-light radius is 1428.5 ± 3.2 km.

From the fit, we find the fainter star to be 0.35 arcsec north and 0.15 arcsec east of the brighter one. See Table 4.2 for the offset in kilometers relative to the CAMC position. Add the offset to the blended star position to get the individual star's position. The declination (g) offsets are systematically north of the CAMC position. This could be due to: (i) an error in the Triton ephemeris, (ii) an error in the CAMC measurement, (iii) a disagreement between the coordinate systems of the star's coordinate and the ephemeris, or (iv) all the above.

Table 4.2 Tr148A and Tr148B Offsets from CAMC Position

	Tr148A	Tr148B
f_0	-2329.2 ± 2.6	5156.1 ± 5.8
g_0	9.4 ± 6.0	3388.7 ± 27.1

We trace the path of the observer through the shadow and establish the closest approach distance of the observed chord from the center of Triton–the impact parameter. The shadow-plane radius $\rho(t)$ is:

$$\rho(t) = \sqrt{f_{p'r}(t)^2 + g_{p'r}(t)^2} \tag{4.4}$$

and the impact parameter is the minimum of $\rho(t)$.

We define a line joining the immersion and emersion location of the observer relative to Triton with slope m and intercept b, and substitute it into Eq 4.4:

$$\rho(t) = \sqrt{f_{p'r}(t)^2 + \left[mf_{p'r}(t) + b\right]^2} \tag{4.5}$$

The minimum shadow-plane radius is calculated from the minimization of Eq. 4.5 with respect to $f_{p'r}(t)$. If the observer's path in the shadow plane were not linear [see Elliot *et al.* (1993) for an example], the minimum shadow-plane radius would be found by another method. The resulting impact parameters are given in Table 4.3, along with the half-light radius residual for each site and the velocity of the occultation shadow relative to the observer (the shadow velocity). Also given in the table are the immersion and emersion half-light times from isothermal model fits and the formal error of the times.

Table 4.3 Tr148 Astrometric Solution

Site	Star	UT[a] (mm:ss) after 07 hr at 50% flux		Timing Error	Impact Parameter	Im. Resid.	Em. Resid.	Vel.
		Immersion	Emersion	(s)	(km)	(km)	(km)	(km/s)
IRTF	B	33:16.29	35:09.81	0.08	147.9 ± 25.3	0.5	-0.2	25.03
KAO	A	38:37.00	40:17.96	0.14	682.9 ± 5.7	-2.0	-3.2	24.80
Lick	A	36:41.97	37:56.42	0.21	1089.4 ± 5.7	1.6	4.3	24.95
Lick	B	31:08.60	32:46.86	0.79	706.2 ± 25.3	-10.9	-16.9	24.95
Lowell	B	30:28.78	32:21.91	0.36	264.4 ± 25.3	-2.0	13.6	24.92
WIRO	A	36:13.67	37:01.18	0.74	1306.8 ± 5.7	-0.8	12.3	24.88

[a] on 1995 August 14

The residuals, displayed in Table 4.3, show no systematic behavior that would suggest a change in the model (such as including timing offset at some stations, or changing the figure). The larger residuals for the Lick occultation of Tr148B are a result of the weighting. The "goodness" of the fit is estimated by the chi-squared, where the y_i are the data and the $y(x_i)$ are the model points, making the quantity in square brackets the residual:

$$\chi^2 = \sum \left\{ \frac{1}{\sigma_r^2} \left[y_i - y(x_i) \right]^2 \right\} \tag{4.6}$$

The variance in the radial position of the observer σ_r^2 is the sum of the squared error in the GPS positions (assumed to be 0.03 km) and the radial component of the timing error squared translated to kilometers by the shadow velocity:

$$\sigma_r^2 = \sigma_{GPS}^2 + \left(\sigma_t \vec{v} \cdot \hat{r} \right)^2 \tag{4.6}$$

The radial component of the timing error dominates the variance, with a root-mean square (RMS) value of approximately 30 km. The chi-squared for the fit is 8.77 and the number

of degrees of freedom is 7. The probability of a random set of data having a χ^2 greater than or equal to this is 27%. This is a good fit of the data.

We re-fit the light-curve timings to the circular figure of Triton without the IRTF observations (since they are controlling the weighted solution) to see how robust the solution is. The solutions agreed within their errors and the impact parameter for the IRTF differed from the adopted solution by only 0.5 km. In this fit, the location of Tr148B relative to Tr148A is established by the lower signal-to-noise ratio Lick (Tr148B) and Lowell light curves. The IRTF residuals are +9.2 km for immersion and –4.3 km for emersion with an uncertainty of 4.7 km. The immersion residual is ~2σ significance and the emersion is consistent with the spherical model.

The longitudes and latitudes probed on Triton by each chord (at the time of half-light) are given in Table 4.4. The longitude and latitude are calculated by rotating the shadow plane (*fg*) coordinates to the *x'y'z'* system. This is the same as the *xyz* system defined in Elliot *et al.* (1993). We will denote it with primed coordinates because the unprimed coordinates *x* and *y* will be used in Chapter 5. The $\hat{z}'$ direction is aligned with the north pole of Triton and the $\hat{x}'$ direction is defined by the intersection of the satellite's equatorial plane with the Earth's equatorial plane (J2000.0) at the ascending node of the Earth's equator. The rotation matrix depends on *U* (the longitude of the projection of $\hat{h}$ onto the *x'y'* plane) and *B* (the angle between the north pole of the satellite and the *fg* plane); see Elliot *et al.* (1993). Let *W* be the angle along the satellite's equator from the $\hat{x}'$ axis to the prime meridian; see Figure on p. 394 in Seidelmann (1992). The location of Triton's pole and prime meridian at event time is given in the Explanatory Supplement to the Astronomical Almanac (Seidelmann 1992, see p. 413).

Let γ be the angle along the satellite's equator from the $\hat{x}'$ axis to the location (on the limb) probed by the occultation, then the longitude is γ-W; see Figure 4.1. The latitude is the arcsine of the z' coordinate of the star relative to Triton.

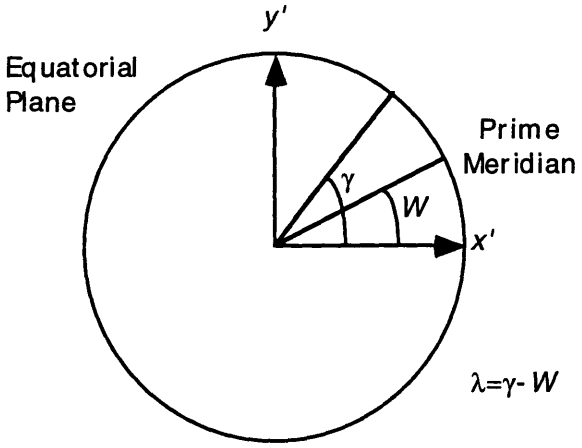

Figure 4.1 The equatorial plane of Triton. The angle along the equator to the prime meridian is *W* and we define γ [$\tan^{-1}(y'/x')$] to be the angle from the *x'* axis to the location of the star in the *x'y'* plane. The longitude is the difference between γ and *W*.

Table 4.4 Triton Longitude and Latitude Probed at Half-Light

Site	Star	Immersion		Emersion	
		Longitude (deg.)	Latitude (deg.)	Longitude (deg.)	Latitude (deg.)
IRTF	B	81.8	–6.0	271.0	13.6
KAO	A	110.5	–27.0	244.6	–9.0
Lick	A	132.5	–36.5	227.5	–22.0
Lick	B	63.6	9.8	291.8	27.7
Lowell	B	78.1	–2.7	274.6	16.4
WIRO	A	153.1	–40.7	212.8	–30.5

The astrometric solution is depicted in Figure 4.2 with a globe of Triton as seen from Earth at the event time. The gray circle represents the half-light radius observed in the shadow plane. This is about a scale height smaller than the half-light radius in the planet-plane due to refraction (Baum and Code 1953). The six chords of the Tr148A and Tr148B occultations are displayed.

The perpendicular distance between the extreme occultation chords spans 2013 km on Triton (74% of the globe; from the Lick Tr148B chord 706 km north of Triton's center to the WIRO chord 1307 km south of Triton's center). The mean separation between chords is about 400 km. This is good spatial coverage for a small body occultation.

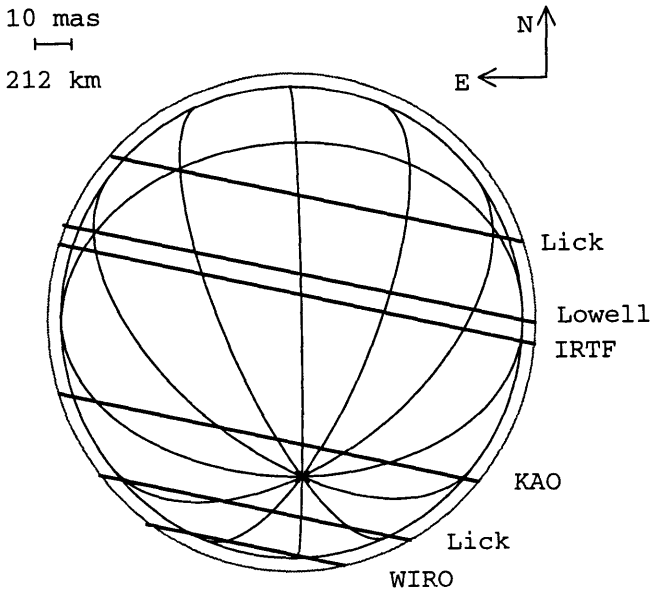

Figure 4.2 Triton's globe with the six occultation chords. The three northernmost chords were occultations of the fainter star, Tr148B, and the three southernmost chords were occultations of Tr148A. The south pole of Triton is visible. The solid line is the surface of Triton (surface radius = 1352. km), and the gray line is the fitted half-light radius.

5. Isothermal and Power-Law Thermal Gradient Model Fits

This chapter is the first of three which present the analysis of the stellar occultation data to learn about the atmosphere of Triton. There are two standard analysis techniques for retrieving profiles of atmospheric temperature, pressure and number density from an occultation light curve. They are: (i) analytical model fitting and (ii) numerical inversions. This chapter presents the results of isothermal and power-law thermal gradient model fits to the occultation light curves (Elliot and Young 1992). According to current theoretical models (Yelle *et al.* 1991; Strobel *et al.* 1996), the atmosphere of Triton in the altitude range probed by stellar occultations is not isothermal (because of heat conducted down from the ionosphere), so the results of these isothermal model fits should not be over interpreted. To be specific, the derived temperature is an equivalent isothermal temperature, not necessarily the actual temperature of the atmosphere. The same is true of the scale height.

Despite this caveat, isothermal model fits can be very informative when used as the basis of comparisons, to detect differences in the equivalent scale height as a function of the sub-occultation point on Triton and over time. We shall show that isothermal model fits are also useful for calibrations (both astrometric and photometric). From a comparison of impact parameters derived from different methods, we will show the far-limb flux is contributing to the light curve. Finally, a thermal-gradient model will be fit to the highest SNR data.

5.1 Far-Limb Flux

In this section, we demonstrate that the flux contribution from the far-limb must be included to accurately model Triton's atmosphere. First, we describe the stellar occultation process and define the term "far-limb" flux. Elliot and Young (1992), hereafter referred to as EY92, describe the processes that affect the observed flux of an occulted star and we will expand their development to explicitly treat the far-limb flux contribution.

The basic process is depicted in Figure 5.1. Parallel rays of starlight are incident on the planet from the left, with the observer located in the shadow plane a distance D from the planet plane. Both the shadow plane and planet plane are perpendicular to the incident light rays (which are parallel to the x-axis). The coordinate r is the radius in the

planet plane measured from the center of the occulting body (in this case Triton). The coordinate y is the observer's location in the shadow plane; the absolute value of y is the shadow-plane radius ρ. As seen in Figure 5.1, the observer can receive flux from two regions of the limb: the near and far. The near-limb flux received by the observer at y has not crossed the x axis, while the far-limb flux has been refracted across the x-axis.

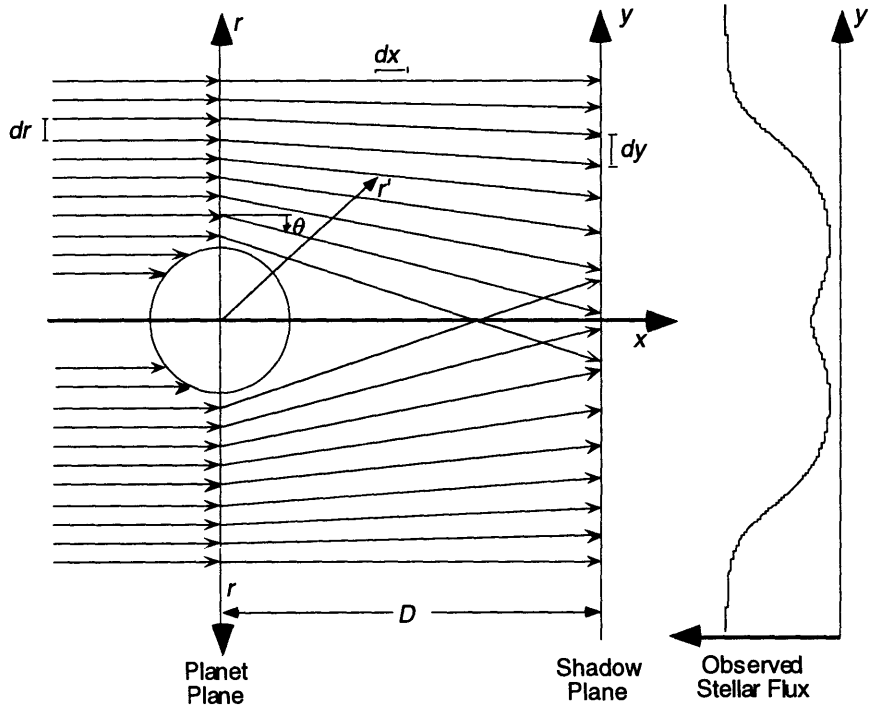

Figure 5.1 Stellar occultation by a planetary atmosphere. Starlight incident from the left encounters a planetary atmosphere where refraction bends the light rays. The refracted light, dimmed by the spreading of the rays, is observed in the shadow plane. The resulting occultation light curve is seen on the left. Light that has crossed the x-axis constitutes the far-limb flux. [After Elliot and Olkin (1996)].

Starlight with a closest approach to the planet r is bent by the refraction angle $\theta(r)$, measured negative toward the planet. At any point in the atmosphere, the light ray is a distance r' from the center of the plane where $r'^2 = r^2 + x^2$. We have assumed the refraction angle is small.

The total bending of the ray is the integral of the curvature over its path (Wasserman and Veverka 1973), where $K(r)$ is the curvature, n_I is the index of refraction of the atmosphere and $\nu(r)=n_I(r)-1$ is the refractivity. We assume that $n_I(r)$ is approximately equal to 1.

$$\theta(r) = \int_{-\infty}^{\infty} K(r)\cdot dx = \int_{-\infty}^{\infty} \frac{1}{n_I}\frac{dn_I}{dr}\cdot dx \approx \int_{-\infty}^{\infty} \frac{r}{r'}\frac{d\nu(r')}{dr'}dx \qquad (5.1)$$

The starlight at the observer is dimmed by (i) the spreading of the light due to refraction and (ii) extinction (scattering and/or absorption) of the starlight with line-of-sight optical depth τ_{obs}. The observed flux is also affected by geometric focusing; the starlight is focused by the ratio of the planet-plane radius to the shadow-plane radius $r/|\rho(r)|$ as the annulus of light at r is compacted into a smaller area–the annulus with radius ρ–due to refraction. From EY92 we have the following equation for the flux received by the observer from the near-limb of the planet $\zeta(r)$.

$$\zeta(r) = \frac{r}{\rho(r)}\left|\frac{dr}{d\rho(r)}\right| e^{-\tau_{obs}(r)} \tag{5.2}$$

The planet-plane radius r is related to the shadow-plane radius ρ by the refraction angle θ and the distance from the observer to the planet D (assuming θ is a small angle):

$$y(r) = r + D\theta(r) \tag{5.3}$$

Now that we have expressions for $\zeta(r)$ and $y(r)$, we can formulate the observed flux from both limbs. The observed flux from the near limb as a function of y is $\zeta(y) = \zeta(r[y])$. Assuming the atmosphere is spherically symmetric, the far-limb flux at y is equal to the near-limb flux at $-y$ and the observed flux from both limbs is:

$$\phi(\rho) = \zeta(y) + \zeta(-y) \tag{5.4}$$

At the smallest values of ρ, the observer is within the evolute of a central flash (Elliot *et al.* 1977) and there are more contributions to the observed flux (flux is received from all the perpendicular limb points). We will not address the flux within the evolute because it is not relevant to the occultation data presented here. The central flash of the IRTF light curves is a result of focusing, not within the evolute. The size of the evolute is about equal to the difference between the equatorial and polar radii (Elliot *et al.* 1977). For Triton, this is approximately 0.6 km (see Chapter 4). We were well outside the evolute.

We need an expression for the flux as a function of time since that is the observable in an occultation. We have the flux as a function of ρ and can relate ρ to the time through the shadow velocity v, the impact parameter ρ_{Min} and midtime t_{Mid}:

$$\rho(t) = \sqrt{\rho_{Min}^2 + v^2(t - t_{Mid})^2} \tag{5.5}$$

The clear (no extinction) isothermal and power-law thermal-gradient models (Elliot and Young 1992) that we will fit in this chapter describe the observed flux in terms of the half-light radius r_H and energy ratio at that radius (these are the parameters of the least-

squares fit). The half-light radius is the radius at which the occulted star's flux has dropped by 50% and the energy ratio at the half-light radius λ_H is the ratio of r_H to the scale height at r_H. These parameters can be used to determine the equivalent isothermal temperature and number density and pressure profiles in the atmosphere (assuming hydrostatic equilibrium and the ideal gas law).

Occultation light curves are sensitive to the radius at the half-flux level of the occulted star and the density scale height of the atmosphere. We will look at the expression for the density scale height in an atmosphere in hydrostatic equilibrium. The density scale height is the vertical distance in the atmosphere in which the number density changes by a factor of e:

$$H_n(r) = -\left(\frac{1}{n(r)}\frac{dn(r)}{dr}\right)^{-1} \tag{5.6}$$

From the ideal gas law, we can relate the number density, n, to the pressure, p, and temperature, T, via Boltzmann's constant, k.

$$p(r) = n(r)kT(r) \tag{5.7}$$

We substitute Eq. 5.7 into 5.6 and see that for an isothermal atmosphere the pressure scale height and density scale height are equal.

$$H_n(r) = -\left(\frac{1}{p(r)}\frac{dp(r)}{dr} - \frac{1}{T(r)}\frac{dT(r)}{dr}\right)^{-1} = -\left(\frac{1}{H_p(r)} - \frac{1}{T(r)}\frac{dT(r)}{dr}\right)^{-1} \tag{5.8}$$

Using the assumption of hydrostatic equilibrium and ideal gas, we will substitute an expression for pressure into Eq. 5.8. Hydrostatic equilibrium describes the state in which a change in pressure dp over an interval dr balances the gravitational and centrifugal forces in that interval. Let G be the gravitational constant, M_p be the mass of the planet, and ω be the rotation rate of the atmosphere. The mean mass of the atmosphere is the product of the mean molecular weight μ in atomic mass units and the mass of one atomic mass unit m_{amu} in whatever units one is working (typically kg). With these definitions, we have the following expression for hydrostatic equilibrium:

$$dp(r) = -\left(\frac{GM_p}{r^2} - \omega^2 r\right)\mu(r)m_{amu}n(r)dr \tag{5.9}$$

Assuming the atmosphere is rotating at approximately the same rate as the planetary surface, we find the centrifugal force is much smaller than the gravitational force (by a factor of ~3000). We will ignore the contribution of the centrifugal force.

Dividing the equation of hydrostatic equilibrium by the ideal gas law, we get:

$$\frac{1}{p(r)}\frac{dp(r)}{dr} = -\frac{GM_p\mu(r)m_{amu}}{kT(r)r^2} \tag{5.10}$$

Substituting Eq 5.10 into Eq. 5.8, we get an expression for the number-density scale height in terms of mean molecular weight, temperature and temperature gradient.

$$H_n(r) = \left(\frac{GM_p\mu(r)m_{amu}}{kT(r)r^2} + \frac{1}{T(r)}\frac{dT(r)}{dr}\right)^{-1} \tag{5.11}$$

In general, the number-density scale height is a function of the temperature, temperature gradient and mean molecular weight. For isothermal atmospheres, the occultation observations give the ratio of the temperature to molecular weight. When we fit a non-isothermal atmosphere with an isothermal model, we are deriving the equivalent isothermal scale height. This is the scale height of an atmosphere (with constant molecular weight) that would produce a light curve with the same slope at half-light as the nonisothermal atmosphere (Elliot and Young 1992).

5.2 Comparison of Impact Parameters

The central-flash flux of an occultation light curve is sensitive to the impact parameter; therefore, we can establish the impact parameter by a least-squares fit of the Tr148B central-flash light curve (recorded at the IRTF). The central-flash flux is proportional to $2H/\rho$ (Elliot *et al.* 1977), where H is scale height. In addition to the central flash, the impact parameter controls the chord length and the residual flux level (the amount of stellar flux observed at the bottom of the light curve). These mechanisms for relating the light curve to the impact parameter are not as sensitive as the central-flash flux. Therefore, we cannot as accurately fit for the impact parameter in the other datasets.

Two different isothermal models were fit to the IRTF-PCCD light curve. One model included only the flux from the near-limb, and the other included flux from both the near and far limbs. The results include the fitted values for the impact parameter ρ_{Min}, half-light radius r_H and the energy ratio λ_H. Also given in the table are the scale height at the half-light radius, the equivalent isothermal temperature and the pressure at 1400 km from the center of Triton. We are quoting the pressure at 1400 km, since this is where the fractional error is near its minimum. The minimum radius probed by the near limb (r_{Min}) and the chi-squared per degree of freedom (χ^2_ν)–a measure of the goodness of fit–are given in the table. To calculate the χ^2_ν we need the uncertainty in the light curve flux. This was

estimated from the standard deviation of the flux from the blended Triton-Tr148 image immediately before and after the occultation.

To convert the refractivity to number density and then to pressure and temperature, we have assumed the atmosphere is pure N_2. The refractivity of N_2 at 0° C and 1 atm. is 2.98×10^{-4} (Peck and Khanna 1966) at a wavelength of 0.7 μm (the effective wavelength of the CCD observations). For the near-infrared observations with an effective wavelength of 2.2 μm, the refractivity of N_2 at 0° C and 1 atm. is 2.94×10^{-4} (Peck and Khanna 1966).

Table 5.1 Isothermal Fit Results of IRTF Data

Parameter	Near Limb Only Model	Two Limb Model
ρ_{Min} (km)	69 ± 4.8	142.6 ± 7.5
r_H (km)	1439.7 ± 1.4	1444.1 ± 1.6
λ_H	75.8 ± 3.3	75.1 ± 3.3
$H(r_H)$ (km)	19.0±0.8	19.2 ± 0.8
T_{iso} (K)	44.1 ± 1.9	44.4 ± 1.9
P_{1400} (μbar)	0.96 ± 0.08	1.22 ± 0.11
r_{Min} (km)	1364.5	1369.1
χ^2_ν	0.984	0.979

Both models assume no extinction and a deep atmosphere. The second assumption (deep atmosphere) means that the stellar flux was not cut off by the satellite's surface, but the atmosphere continued to arbitrarily small radii. This was done to eliminate discontinuous features from the model. Discontinuous features in a least-squares model fit can artificially decrease the error estimates by locking onto noise spikes. For the near-limb flux, the deep atmosphere assumption is valid since none of the chords probed to the solid surface (see Table 5.1), which is around 1352 km. The deepest probing chord reached a radius of 1369 km, about 17 km altitude. In reality, the far-limb flux is cut off by extinction and the solid surface, but this occurs at a level where the far-limb is contributing less than 0.4% of the flux. The best-fit two-limb model to the IRTF-PCCD light curve is presented in Figure 5.2. This figure shows: (top) the near-limb flux contribution, (middle) the far-limb flux contribution, and (bottom) the two-limb model and data.

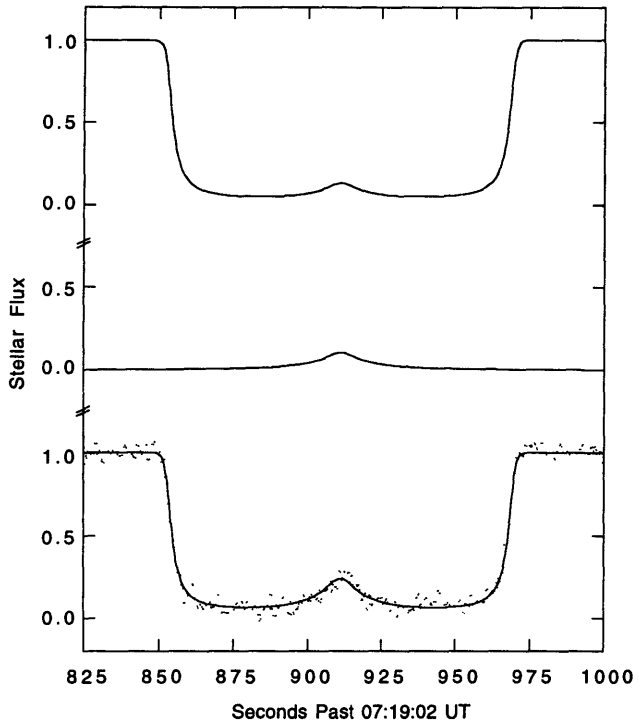

Figure 5.2 Isothermal model flux. The top curve is the stellar flux received from the near limb. The middle curve is the stellar flux received from the far limb. The far-limb flux contribution is close to zero everywhere except at the midtime. The bottom curve shows the two-limb model with the occultation data superposed.

In comparing the fit results of the near-limb and two-limb models, we see the energy ratio, equivalent isothermal temperature and scale height agree across models and both fits are good matches to the data (as evidenced by χ^2_ν close to unity). The value of the fitted impact parameter from the two-limb model agrees with that from the astrometric solution of Chapter 4, while the impact parameter from the one-limb model fit does not. Recall the astrometric calibration of the occultation data yielded an impact parameter of 147.9 ± 25.3 km. This is ~3σ larger than the fitted value from the near-limb model, but agrees well with the impact parameter for the two-limb model fit. This agreement between the fitted impact parameter and the astrometric solution is evidence that the far-limb contribution to the flux is needed.

We adopt 142.6 ± 7.5 km as the impact parameter of the IRTF station. It is consistent with the solution from the light-curve timings and has a smaller error. We shift the impact parameters accordingly for the other Tr148B chords, since the separations of the stations are well known (from GPS data). Table 5.2 gives the adopted impact parameters for the Tr148A and Tr148B observing sites.

Table 5.2 Tr148 Astrometric Solution

Site	Star	ρ_{Min} from multiple chords (km)	ρ_{Min} from isothermal fit (km)	Adjusted ρ_{Min} (km)	Adopted ρ_{Min} (km)
IRTF	B	147.9 ± 25.3	142.6 ± 7.5	-	142.6 ± 7.5
KAO	A	682.9 ± 5.7	-	-	682.9 ± 5.7
Lick	A	1089.4 ± 5.7	-	-	1089.4 ± 5.7
Lick	B	706.2 ± 25.3	-	700.9 ± 7.5	700.9 ± 7.5
Lowell	B	264.4 ± 25.3	-	259.1 ± 7.5	259.1 ± 7.5
WIRO	A	1306.8 ± 5.7	-	-	1306.8 ± 5.7

5.3 Photometric Calibration from Isothermal fit

The photometric calibration of an occultation light curve establishes the signal levels that correspond to the full- and zero- flux levels of the occulted star, as mentioned in Chapter 2. For the Tr148 events, we need to know the relative intensity of the two components in the blended star to determine the zero-flux level of either Tr148A or Tr148B.

The full signal level s_f (for both events) is the combined flux from Triton, Tr148A and Tr148B. The background signal level for an occultation of Tr148A (s_{bA}) is the combined flux from Triton and Tr148B. Similarly, the background signal level for an occultation of Tr148B (s_{bB}) is the combined flux from Triton and Tr148A.

In Chapter 2, we presented the intensity ratio of Tr148AB/Triton from post-event imaging. This section will establish the relative intensity of the two sources in the blended star from isothermal model fitting of the Lick observations which recorded the occultation of both stars. The stars are too close to derive separate photometry from ground-based imaging with current techniques, but could be resolved using the Hubble Space Telescope. With the relative intensity of the two sources, we can use the post-event photometry to calculate the background levels for the occultation light curves. A comparison of the backgrounds from post-event photometry and isothermal model fitting will be presented.

Fortunately, observers at Lick Observatory recorded the occultation of both components, allowing us to establish the relative brightness of the two stars, at least for the photometric system employed at Lick. A two-limb, clear, deep-atmosphere isothermal model was fit to both light curves to determine the full and background signal levels of the light curves, as well as the half-light radius, energy ratio and the midtime of

the event. The impact parameter was fixed at the adopted value. We get the intensity ratio r_2 (Tr148A/Tr148B) from the ratio of the full minus the background levels.

$$r_2 = \frac{s_f - s_{bA}}{s_f - s_{bB}} \tag{5.12}$$

From the visible observations recorded at the 0.9-m telescope at Lick Observatory, we get an intensity ratio (r_2) of 3.776 ± 0.151. For the infrared Tr148B light curve recorded at the 1.1-m telescope at Lick, the half-light radius and energy ratio had to be fixed in the fit because of the low SNR. The intensity ratio with the K' filter is 4.57 ± 0.48.

From the intensity ratios r_1 (Tr148/Triton) and r_2 (Tr148A/Tr148B) and the full signal level s_f, we can derive the background signal for the occultations:

$$\begin{aligned} s_{bA} &= \frac{s_f}{1+r_1}\left(1+\frac{r_1}{1+r_2}\right) \\ s_{bB} &= \frac{s_f}{1+r_1}\left(1+\frac{r_1 r_2}{1+r_2}\right) \end{aligned} \tag{5.13}$$

Using these equations and the photometry from Chapter 2, we found the background levels in column 4 of Table 5.3. The errors were propagated from uncertainties in s_f, r_1 and r_2. The third column in the table is the background level from the isothermal fit. Columns 5 and 6 give the difference of the background levels as a fraction of the error in the difference and as a percentage of the occulted star flux.

Table 5.3 Fitted and Calculated Background Levels

Obs.	Event	b_{fit}	b_{phot}	Δ^a/σ	Δ%
KAO	Tr60	0.00801 ± 0.00007	0.00781 ± 0.00004	2.5	4.4
IRTF[b]	Tr148B	83110. ± 53.	81886. ± 385.	3.2	10.2
IRTF[c]	Tr148B	11793 ± 22.	11658 ± 160	0.8	7.9
KAO	Tr148A	0.04495 ± 0.0002	0.0437 ± 0.0003	3.4	3.8
Lick	Tr148A	31070. ± 282.	30774. ± 230.	0.8	1.1
Lick	Tr148B	50795. ± 265.	50700. ± 233.	0.3	1.3

[a] $\Delta = \left(\frac{b_{fit} - b_{phot}}{f - b_{phot}}\right)$

[b] PCCD

[c] NSFCAM

The calibrations of the Lick light curve from the two methods agree to better than one standard deviation. The same is true for the IRTF-NSFCAM data. None of these data has any known photometric complications (CTE problems, vignetting *etc.*), so the agreement is not surprising.

For the other light curves, the methods disagree by more than two standard deviations and the fitted background levels are larger than that from photometry. There are known complications in extracting accurate photometry from these light curves (a CTE problem in the Tr60 data, significant scattered light in the KAO observations–both Tr60 and Tr148A, and vignetting in the IRTF-PCCD data). If we assume the photometry is correct (and that the fitted background is wrong), then there is more residual flux than predicted by the isothermal models. A reduction in residual flux can be explained by haze or a sharp thermal gradient. The only explanation for additional residual flux is that the temperature is decreasing with altitude in this region. This is unlikely given the warm temperature (100 K) measured near 400 km altitude by the UVS occultation (Broadfoot *et al.* 1989) and the cold surface temperature (38 K) measured by the shape of the N_2 band (Tryka *et al.* 1993).

The assumption that the photometric calibration is correct (and the fitted background is wrong) is inconsistent with the fitted impact parameter of the previous section. The impact parameter is sensitive to residual flux, so the fitted impact parameter would not have agreed with the astrometric solution if the fitted background level was incorrect by a few percent or more.

We conclude that the isothermal model fit provides a better estimate of the background than the post-event photometry for these three datasets. For the other light curves, the backgrounds are consistent and the error in the background from model fitting is about equal to or smaller than the error from the photometry. In all cases, we adopt the background from isothermal fits for the normalization of the light curves (see Figure 5.3 for the normalized light curves).

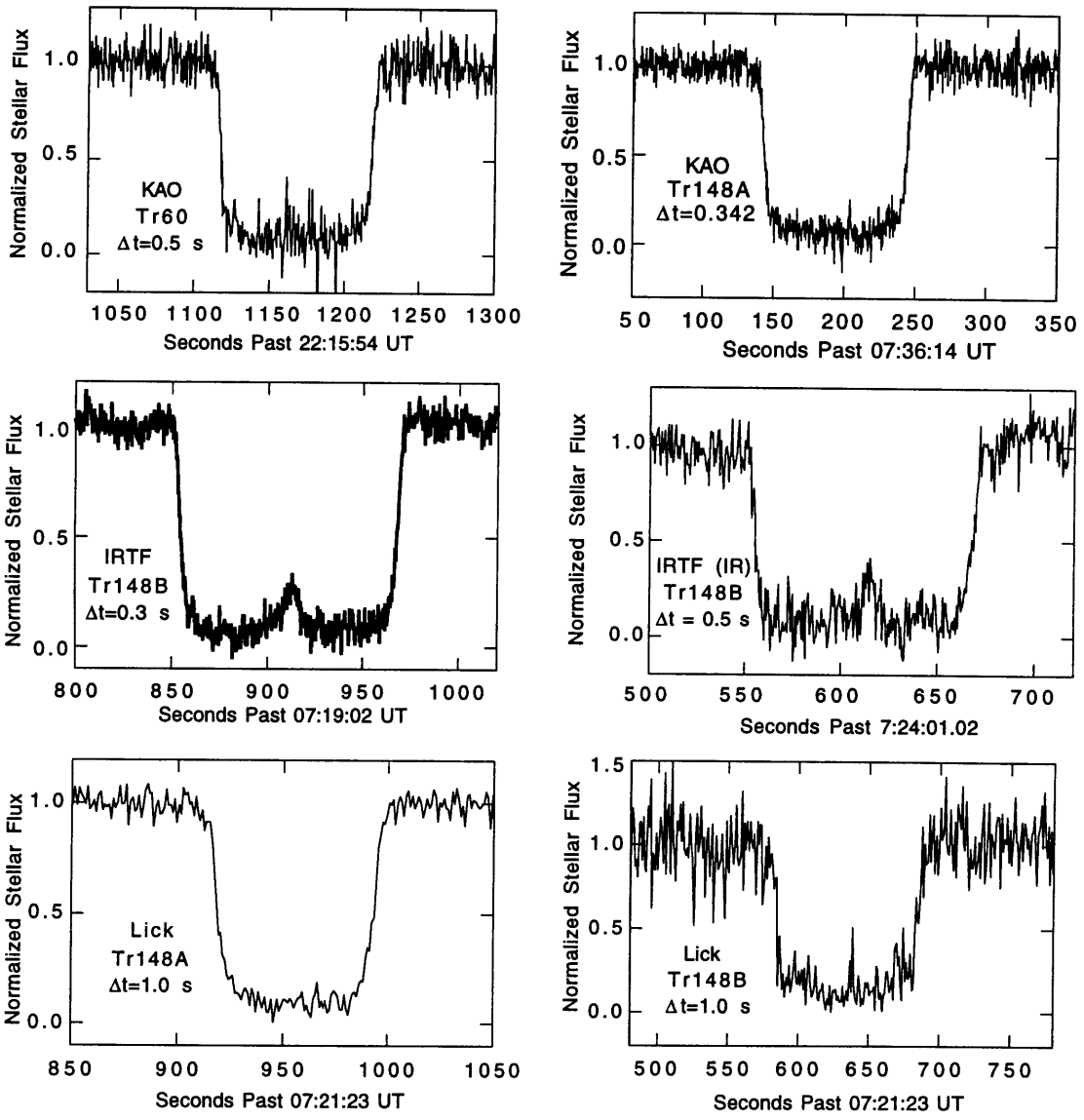

Figure 5.3 Normalized light curves. All light curves were normalized with the full and background level from isothermal model fits.

5.4 Spatial Variability in Triton's Atmosphere

Most of the Tr148 occultation light curves appear symmetric about the midtime of the event; however, the IRTF light curves (both visible and IR) are not. This can be seen by an offset of the event midtime relative to the central peak (Figures 5.2 and 5.3). Figure 5.4 shows the IRTF-PCCD light curve with the immersion and emersion sections of the light curves overlaid. The two panels correspond to the light curve at full resolution (0.3 seconds per point) and averaged by 4 (1.2 seconds per point). In the full-

resolution panel, the asymmetry is not evident until about 50 seconds past half light when the emersion points (triangles) are systematically higher than the emersion points (circles). At this time, the occultation is probing a radius of 1370 km on Triton–about 20 km altitude. In the lower panel with the averaged data, we see that the emersion points are systematically higher than the immersion points beginning near 10 seconds (corresponding to a radius of 1398 km) and the asymmetry in the central peak is more pronounced. No asymmetry is evident in the main drop and recovery of the light curve.

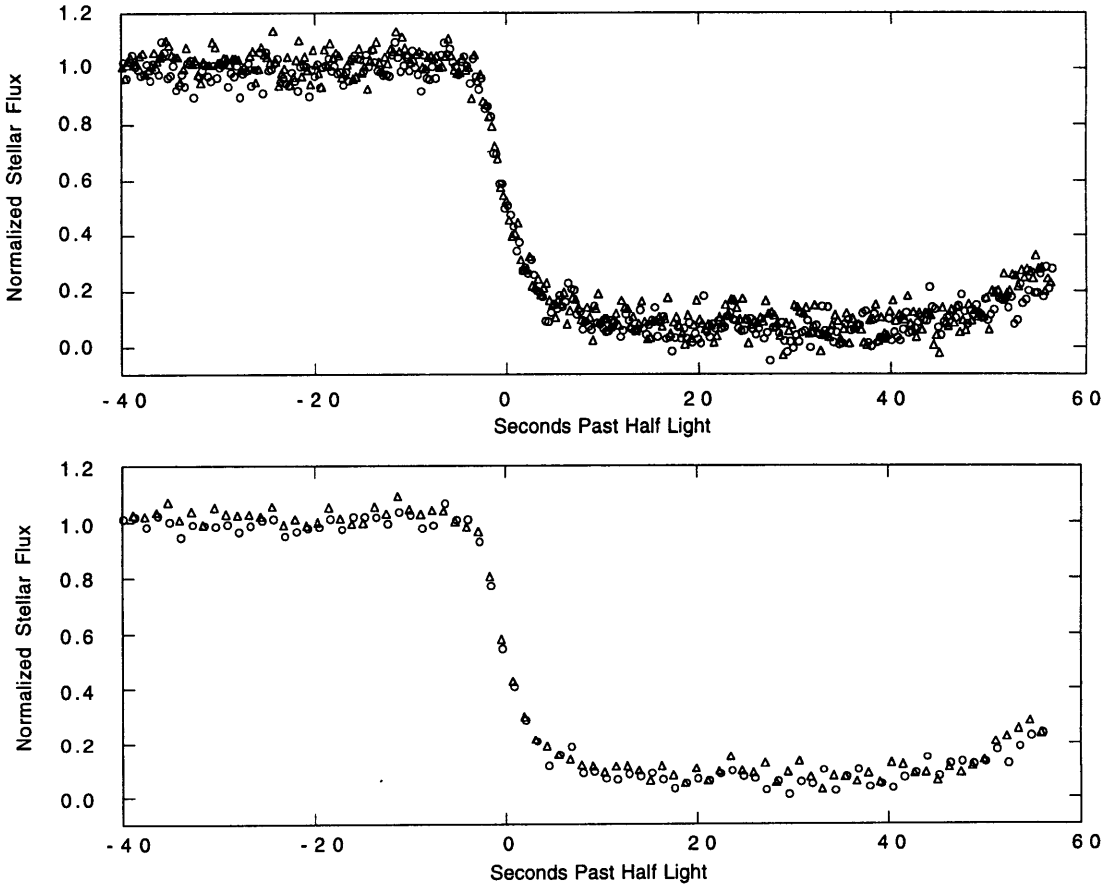

Figure 5.4 The immersion and emersion sections of the IRTF-PCCD light curve. Immersion (circles) and emersion (triangles) were determined by the midtime of the event given by an isothermal model fit. The horizontal axis is the time past half light (with a sign change of the emersion times so that the two curves overlay each other). The upper panel is at full resolution (0.3 seconds per point), while the lower panel is averaged by four so that each point corresponds to 1.2 seconds. One can see the asymmetry in the emersion points (triangles) being usually higher than the immersion points (circles), especially near the central flash.

The asymmetry could either be caused by extinction or a change in scale height. For now we will assume that it is not extinction. We address the issue of extinction in

Chapter 8. The scale height could change due to a change in composition, temperature or temperature gradient (Eq. 5.11). We will perform separate fits of the immersion and emersion chords to estimate the extent of the asymmetry.

The isothermal, two-limb model discussed above was fit to the normalized immersion and emersion curves. The light curves were normalized with the background level from the isothermal model fits and the midtime was fixed. With a fixed midtime (defining the center of Triton) and a fixed impact parameter (defining the chord length), the half-light radius is constrained.

For all fits with fixed impact parameters reported in this chapter, the errors in the fitted and derived parameters will include the uncertainty in the impact parameter. To do this, the light curve is fit three times (using the impact parameter at the nominal value and ± 1 standard deviation from nominal) to determine the additional error in the fitted parameters due to the imperfectly known impact parameter.

Table 5.4 shows the fit results to the individual chords. There is no asymmetry evident in the Tr148A light curves, but we see significant (more than 1σ) change in the scale height in the IRTF Tr148B data. The other two Tr148B light curves (Lowell and Lick) show an approximately 1σ change in scale height.

To establish the extent of this asymmetry we translate the change in scale height into a change of temperature, although the change in scale height could also be attributed to a change in composition or temperature gradient. The last row of the table shows the change in equivalent isothermal temperature between immersion and emersion. From the highest SNR data, the asymmetry is consistent with a change in temperature of 7K (~16%).

Some light curves show an asymmetry while others do not. This could be a result of the light curves probing different levels in Triton's atmosphere. To investigate this possibility, we weight the IRTF light curves so they probe the same radii as the KAO light curve. The weights are based on the number of samples per radius interval. The radius interval was chosen to be the distance probed during one integration by the reference light curve before there was significant refraction (the product of the shadow velocity and integration time). The number of samples per radius interval is calculated for each light curve (using the best fitting isothermal fit to define the atmospheric structure). As we sample deeper into the atmosphere, the refractivity increases and the number of samples per radius interval increases. In each bin (radius interval), the data are weighted by the ratio of the samples in that bin for the reference light curve to the samples in that

bin for the weighted light curve. Bins sampled more by the reference light curve (the KAO) will have a larger weight in the fit. Results of the weighted immersion and emersion fits are given in Table 5.5. The unweighted KAO light curve fit results are included for comparison.

Table 5.4 Immersion and Emersion Isothermal Fit Results

	IRTF (vis.) Tr148B	IRTF (IR) Tr148B	KAO Tr148A	Lick Tr148A	Lick Tr148B	Lowell Tr148B	WIRO Tr148A
Immersion:							
r_H (km)	1444 ± 2	1443 ± 5	1448 ± 4	1452 ± 5	1444 ± 15	1450 ± 7	1461 ± 9
λ_H	81.3 ± 2.6	85.8 ± 6.9	67.6 ± 3.2	70.2 ± 3.7	52.3 ± 10.3	93.6 ± 14.9	59.6 ± 9.5
$H(r_H)$ (km)	17.8 ± 0.6	16.8 ± 1.4	21.4 ± 1.0	20.7 ± 1.1	27.6 ± 5.5	15.5 ± 2.5	24.5 ± 3.9
T_{iso} (K)	41.0 ± 1.3	38.9 ± 3.1	49.1 ± 2.3	47.2 ± 2.5	63.7 ± 12.5	35.4 ± 5.6	55.2 ± 8.7
P_{1400} (μb)	1.2 ± 0.1	1.2 ± 0.3	1.5 ± 0.3	1.9 ± 0.5	1.5 ± 0.9	1.8 ± 0.9	2.8 ± 1.0
Emersion:							
r_H (km)	1444 ± 2	1444 ± 6	1448 ± 4	1452 ± 5	1450 ± 16	1453 ± 9	1462 ± 9
λ_H	69.4 ± 2.2	58.3 ± 4.0	67.7 ± 3.7	72.3 ± 4.0	41.3 ± 6.7	73.4 ± 10.7	55.7 ± 8.4
$H(r_H)$ (km)	20.8 ± 0.7	24.8 ± 1.7	21.4 ± 1.2	20.1 ± 1.1	35.1 ± 5.8	19.8 ± 2.9	26.3 ± 4.0
T_{iso} (K)	48.0 ± 1.5	57.1 ± 3.8	49.1 ± 2.7	45.8 ± 2.5	80.3 ± 13.0	45.1 ± 6.6	59.1 ± 8.9
P_{1400} (μb)	1.3 ± 0.1	1.4 ± 0.4	1.5 ± 0.3	1.8 ± 0.5	2.3 ± 1.2	1.9 ± 0.9	2.9 ± 1.0
ΔT_{iso} (K)	7.0 ± 2.0	18.2 ± 4.9	0.0 ± 3.5	-1.4 ± 3.5	16.6 ± 18.0	9.7 ± 8.6	3.9 ± 12.4

Even probing the same radii as the KAO curve, we see asymmetry in the IRTF fit results, indicating that the asymmetry is due to spatial variations and not variations with altitude. The temperature differences in the weighted fit are consistent with those from the unweighted fit. We infer that the asymmetry is present above 1378 km (the minimum radius probed by the KAO) and that it is localized because it is not seen in the southern-hemisphere chords.

Table 5.5 Weighted Immersion and Emersion Isothermal Fit Results

	IRTF (vis.) Tr148B	IRTF (IR) Tr148B	KAO[a] Tr148A
Immersion:			
r_H (km)	1444.4 ± 2.0	1446.6 ± 5.0	1447.9 ± 3.8
λ_H	77.4 ± 2.9	74.5 ± 7.1	67.6 ± 3.2
$H(r_H)$ (km)	18.7 ± 0.7	19.4 ± 1.8	21.4 ± 1.0
T_{iso} (K)	43.0 ± 1.6	44.7 ± 4.2	49.1 ± 2.3
P_{1400} (μb)	1.2 ± 0.1	1.4 ± 0.4	1.5 ± 0.3
Emersion:			
r_H (km)	1445.0 ± 2.2	1445.0 ± 5.7	1447.9 ± 4.2
λ_H	64.1 ± 2.3	56.0 ± 4.7	67.7 ± 3.7
$H(r_H)$ (km)	22.6 ± 0.8	25.8 ± 2.2	21.4 ± 1.2
T_{iso} (K)	52.0 ± 1.9	59.4 ± 5.0	49.1 ± 2.7
P_{1400} (μb)	1.3 ± 0.1	1.5 ± 0.4	1.5 ± 0.3
ΔT_{iso} (K)	9.0 ± 2.5	14.7 ± 6.5	0.0 ± 3.5

[a]unweighted KAO results for reference.

5.5 Results from the 1993 Stellar Occultation

The Tr60 stellar occultation observation provides a probe of Triton's atmosphere at a different time from the 1995 stellar occultation. A little more than two years past between these events. This provides a baseline to look for seasonal change, but it is short interval on the time scale of a Triton season (about 100 years).

Although the post-event astrometry for the Tr60 event has an error of only 6 milliarcsec (Olkin *et al.* 1996), this translates to 133 km at the distance of Triton. This large uncertainty in the impact parameter will inflate the error in the estimated scale height. To reduce this effect, we can fit for the impact parameter if we constrain the half-light radius. If there is a significant difference between the two solutions with the half-light radius fixed at the same value, then we will know that something in the atmosphere has changed. We fix the half-light radius at 1446 km, a value consistent with the Tr148 results and fit a clear, deep-atmosphere isothermal model to the light curve. The fitted impact parameter is 350 ± 15 km, which agrees with the impact parameter from the post-event astrometry (359 ± 133 km) and has smaller error. This is our adopted solution, see Figure 5.5 for the data, model and residuals. It has a scale height of 24.6 ± 2.8 km. To

test the sensitivity of the solution to the fixed half-light radius, we refit the light curve, fixing the impact parameter at the value given by the post-event astrometry and fit for the half-light radius. The results give a scale height of $24.7^{+2.8}_{-4.6}$ km, which is consistent with our adopted solution, but has a larger error because of the large uncertainty in the impact parameter.

In the Tr60 light curve, there are a few data points that are inconsistent with their neighbors. The formal error for these "outlier" points from the numerical PSF modeling is larger than the others, so we used the formal error to weight the data. The fits were performed on the unnormalized light curve and the background level was determined.

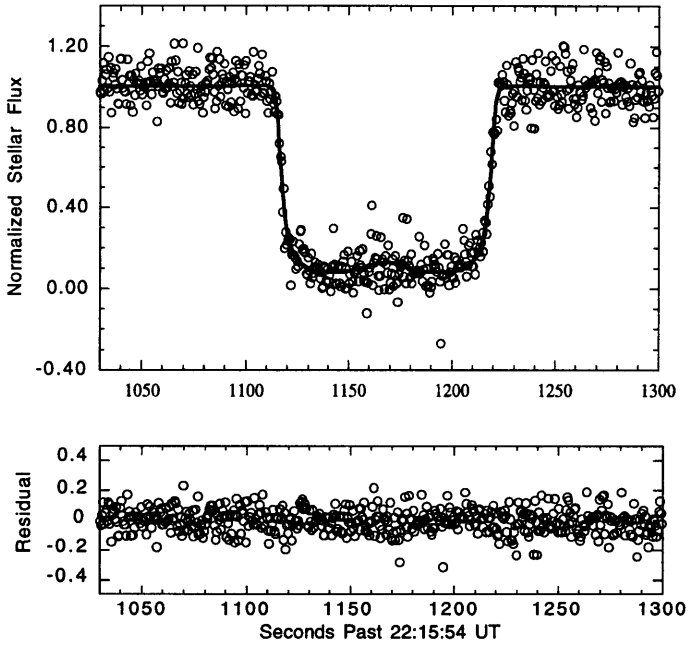

Figure 5.5 Tr60 light curve data, model and residuals. The isothermal model was fit to the unnormalized light curve, and the data, model and residuals were normalized from the fitted background level for display. The model had a fixed half-light radius and the data were weighted by the formal error from the PSF model fitting. The residuals in the lower panel are weighted. The least-squares fit gives an impact parameter consistent with the value from post-event astrometry.

The results from the isothermal model fit of the whole light curve, immersion and emersion are given in Table 5.6. The scale height and temperature are about one standard deviation higher than that determined for the highest SNR Tr148 light curves. The pressure at 1400 km derived from the isothermal fits of the 1993 light curve is consistent with the pressures derived from the 1995 light curves.

The minimum radius probed by this light curve is 1361 km. Although the IRTF-PCCD light curve has a smaller impact parameter than the Tr60 light curve, the larger scale height (determined by the fit) compensated for this.

We shall derive an upper limit on the pressure change between 1993 and 1995. The pressure at 1400 km in 1995 from the weighted average of the pressures measured at immersion and emersion for all the Tr148 light curves in Table 5.5 is 1.3 ± 0.5 μbar. The

change in atmospheric pressure between the 1993 observations and the 1995 observations is -0.2 ± 0.5 μbar (-0.09 ± 0.26 μbar/yr). This means there is a 99% probability (3σ) that the atmospheric pressure decreased by less than 1.7 μbar and increased by less than 1.3 μbar in this time interval (765 days).

Table 5.6 Tr60 Isothermal Fit Results

	Tr60 whole light curve	Tr60 immersion	Tr60 emersion
r_H (km)	1446.	1446.	1446.
λ_H	58.7 ± 6.6	60.6 ± 4.3	57.1 ± 4.8
$H(r_H)$ (km)	24.6 ± 2.8	23.8 ± 1.7	25.3 ± 2.1
T_{iso} (K)	56.6 ± 6.4	54.9 ± 3.92	58.3 ± 4.86
P_{1400} (μbar)	1.5 ± 0.1	1.5 ± 0.1	1.5 ± 0.1

5.6 Thermal Gradient Model Fits

Published models of Triton's atmosphere (Yelle *et al.* 1991; Krasnopolsky *et al.* 1993; Strobel *et al.* 1996) have a thermal gradient in the altitude range that we are probing by these stellar occultations. We fit the thermal gradient model of Elliot and Young (1992) to the two highest SNR 1995 Triton occultation light curves. The EY92 thermal-gradient model assumes that the temperature follows a power law of the form:

$$T(r) = T_0\left(\frac{r}{r_0}\right)^b \tag{5.14}$$

The least-squares solution is given in Table 5.7. All model parameters are given, including fitted and fixed parameters (the fixed parameters have no errors). Also, quantities derived from the model parameters are given, including the density scale height, temperature and pressure at 1400 km radius, and minimum radius probed by the near limb. The χ^2_ν is also given for the fits. For both fits, the χ^2_ν is near unity and similar to the value from the isothermal model fits.

Table 5.8 gives the correlation coefficients between fitted parameters from the least-squared fit. Correlation matrices are symmetric, so only the upper diagonal elements are given in Table 5.8. Most of the correlations are very small (less than 0.1).

The fitted values for the power-law index b from the IRTF-PCCD data is 1.3 ± 1.3. The power-law index is related to a temperature gradient through the following equation (Elliot and Young 1992):

$$\left.\frac{dT(r)}{dr}\right|_{r=r_0} = \frac{bT_0}{r_0} \tag{5.15}$$

At a radius of 1400 km, this power-law index translates to a temperature gradient of 0.04 ± 0.04 K/km. Hence, the IRTF-PCCD light curve does not show evidence of a significant thermal gradient.

The fitted values for the power-law index *b* from the KAO-Tr148A data was 9.5 ± 13.2. The uncertainty in the power law index from this light curve is large, supporting either a possible thermal gradient or an isothermal temperature profile. The SNR would have to be larger to discriminate between the two profiles.

Table 5.7 Power-Law Thermal Gradient Fits

Model Parameters	IRTF	KAO
background level	83135.5 ± 56.3	0.04557 ± 0.00054
background slope	-0.24 ± 0.06	$7.1\times10^{-6} \pm 6.4\times10^{-7}$
full-scale level	93949.0 ± 11.5	0.07749 ± 0.00003
midtime[a] (s)	911.00 ± 0.05	193.47 ± 0.09
r_H (km)	1445.3 ± 1.4	1449.3 ± 2.8
λ_H	74.3 ± 2.8	74.9 ± 12.1
b	1.3 ± 1.3	9.5 ± 13.2
ρ_{Min} (km)	142.6	682.9
v (km/s)	25.03	24.80
Δt (s)	0.300	0.342
Derived Quantity		
$H(r_H)$ (km)	20.4 ± 1.3	28.3 ± 16.35
T_{1400} (K)	44.9 ± 1.8	46.7 ± 10.5
P_{1400} (μbar)	1.3 ± 0.1	1.887 ± 0.567
r_{Min} (km)	1369.1	1378.0
Fit Information		
χ^2_ν	0.980	0.959

[a] seconds past start of the subframe series

Table 5.8 Correlation Matrix (IRTF-PCCD) Power-Law Thermal Gradient Fit

	background	slope	full scale	midtime	r_H	λ_H	b
background	1	–0.0007	0.0464	–0.0003	0.2156	0.5596	0.4805
slope	–	1	–0.0204	0.0482	–0.0023	0.0005	0.0021
full scale	–	–	1	–0.0021	0.1151	–0.0227	0.1180
midtime	–	–	–	1	–0.0001	0.0001	–0.0001
r_H	–	–	–	–	1	–0.0727	0.2736
λ_H	–	–	–	–	–	1	–0.2820
b	–	–	–	–	–	–	1

5.7 Adopted Isothermal Model Solutions

In this chapter, we have presented many model fitting results. In this section, we identify our adopted model fits for each dataset and present the values for all model parameters. Some derived quantities are also given in the tables (scale height, equivalent isothermal temperature, pressure at 1400 km radius, and the radius probed at the midtime). The least-squares fits were carried out with the impact parameter fixed at its adopted value. The additional error in the model parameters and derived quantities due to the uncertainty in the impact parameter was determined by running two additional least-squares fits for each adopted solution: one with the impact parameter fixed at the value one standard deviation higher than nominal and another with it fixed at the value one standard deviation lower. The change in the model parameters and derived quantities was then propagated into the errors reported in the tables.

For the symmetric light curves (the Tr148A light curves), the adopted isothermal model fits are the fits to the whole light curve (Table 5.9). The WIRO light curve was normalized by W. Hubbard, therefore, the background level, background slope and full-scale level were not fit. Fitting for these parameters gives a similar solution. The full-scale level corresponds to the full-scale level in a one second integration time. Therefore, the full-scale level of the WIRO data was fixed at 1.25 ($1/\Delta t$). A sample correlation matrix is given in Table 5.10.

Table 5.9 Adopted Isothermal Fit For Symmetric Light Curves

Model Parameter	KAO	Lick A	WIRO
background level	0.0450 ± 0.0002	31070. ± 282	0.
background slope	$7.1\times10^{-6} \pm 6.4\times10^{-7}$	0.880 ± 0.601	0.
full-scale level	$7.746\times10^{-2} \pm 2.7\times10^{-5}$	57713. ± 73.	1.25
midtime[a] (s)	193.480 ± 0.091	956.15 ± 0.12	97.45 ± 0.51
r_H (km)	1447.9 ± 3.5	$1452.0^{+4.8}_{-5.0}$	1462.5 ± 7.8
λ_H	67.7 ± 4.2	71.3 ± 4.9	56.2 ± 5.7
b	0.	0.	0.
ρ_{Min} (km)	682.9 ± 5.7	1089.4 ± 5.7	1306.8 ± 5.7
v (km/s)	24.80	24.95	24.88
Δt (s)	0.342	1.0	0.8
Derived Quantities			
$H(r_H)$ (km)	21.4 ± 1.3	20.4 ± 1.4	26.0 ± 2.7
T_{iso} (K)	49.1 ± 3.0	46.5 ± 3.2	58.5 ± 5.9
P_{1400} (μbar)	$1.5^{+0.3}_{-0.2}$	$1.8^{+0.5}_{-0.4}$	$2.9^{+1.0}_{-0.9}$
r_{Min} (km)	1378.0	1399.3	1425.1
Fit Information			
χ^2_ν	0.959	0.848	0.870

[a] seconds past start of the subframe series

Table 5.10 Correlation Matrix from Isothermal Fit of Lick-Tr148A Light Curve

	background	slope	full scale	midtime	r_H	λ_H
background	1	–0.0194	–0.0367	–0.0015	0.2270	0.8280
slope	–	1	0.3531	0.0974	0.0550	–0.0172
full scale	–	–	1	0.0359	0.1569	–0.0277
midtime	–	–	–	1	0.0054	–0.0016
r_H	–	–	–	–	1	0.0537
λ_H	–	–	–	–	–	1

For the asymmetric light curves, the adopted solutions are the separate immersion and emersion solutions (see Table 5.4).

5.8 Conclusions from Isothermal Model Fits

In summary, we have found that the far-limb flux is contributing to the occultation light curve for the IRTF. Also, for single chord occultations, if the chord exhibits a central flash (that is not suppressed by extinction), then the impact parameter can be accurately derived from model fitting. For our photometric data affected by scattered light from Neptune, a CTE problem, or vignetting, the zero-flux level of the occulted star can be determined by a model fit. From the separate immersion and emersion fits of the IRTF data, we see asymmetry in the scale height of Triton's atmosphere. The asymmetry is consistent with a temperature decrease of ~7 K from immersion to emersion. The atmospheric pressure at 1400 km derived from the 1993 occultation are consistent with those from the 1995 stellar occultation. Finally, from a power-law thermal gradient model of Triton's atmosphere, we find the two highest SNR light curves are both consistent with an isothermal model and the thermal gradient at 1400 km radius from the IRTF-PCCD data is 0.04 ± 0.04 K/km.

6. Numerical Inversions

In this chapter, we present results of numerical inversions of the occultations to retrieve atmospheric pressure and temperature profiles. From inversions we can derive the pressure and temperature directly from the observed flux without assuming an atmospheric model, only that the atmosphere is spherically symmetric and in hydrostatic equilibrium.

6.1 Method

Published methods for inverting an occultation light curve make assumptions that are invalid for a small planet (Wasserman and Veverka 1973; French *et al.* 1978). This section outlines a numerical inversion method that does not rely on these assumptions. In particular we will not assume the scale height is much smaller than the radius of the occulting body. Also, we include the effect of focusing on the observed flux. Certain assumptions are still included. The assumptions relative to the derivation of the refractivity profile include:

1. The atmospheric refractivity $\nu(r)$ varies only with radius.
2. Extinction is not significant in the dimming of the stellar flux.
3. Geometric optics apply (diffraction theory is not necessary).
4. The star is a point source.
5. The refraction angle is small.
6. General relativistic bending of the starlight is not significant.
7. There is no ray crossing.

Further, those assumptions relevant for establishing the number density, pressure and temperature profiles from the refractivity are: (i) the atmospheric composition is known and uniform, and (ii) the atmosphere is in hydrostatic equilibrium.

The most significant assumption in application of this method to the Triton occultation light curves is that there is no ray crossing. We are observing the far-limb flux; therefore, the light rays are crossing. This assumption is important because it is used to relate the change in flux to a given radius level. For these data, there are two regions contributing to the observed flux near the midtime. The inversion method does not have any inherent way to partition the change in flux between the two limbs. For these data,

we will estimate the far-limb flux contribution (using an isothermal model) and remove this from the light curve before inverting. The sensitivity of the results to the far-limb flux estimate will be presented.

The following method was developed by J. L. Elliot (unpublished notes). The normalized near-limb flux $\zeta(r)$ for a clear atmosphere is related to the shadow-plane radius ρ and the planet plane radius r by EY92:

$$\zeta(r) = \frac{r}{\rho(r)}\left|\frac{dr}{d\rho(r)}\right| \tag{6.1}$$

This can be restated as:

$$\zeta(r)\rho(r)\Delta\rho(r) = r\Delta r \tag{6.2}$$

To invert the light curve, we divide the atmosphere into shells; see Figure 6.1. Let the index k refer to quantities at the middle of the kth shell and the index $(k+1/2)$ refer to quantities on the lower boundary of the kth shell. The shells start in the atmosphere where the inversion begins with $k=1$. If we let $\zeta_k=\zeta(r_k)$ and $\rho_k=\rho(r_k)$, then we re-write Eq. 6.2:

$$\zeta_k\rho_k\Delta\rho_k = r_k\Delta r_k \tag{6.3}$$

Assuming r varies linearly over the shell, we have:

$$r_{k+1/2}^2 - r_{k-1/2}^2 = 2\zeta_k\rho_k\Delta\rho_k \tag{6.4}$$

If we know the radius at the top of the first shell $r_{1/2}$, then we have the following summation for the lower-boundary radius given the flux (the shadow-plane radius is given by Eq. 5.5):

$$r_{k+1/2} = \sqrt{r_{1/2}^2 + 2\sum_{i=1}^{k}\zeta_i\rho_i\Delta\rho_i} \tag{6.5}$$

The refraction angle θ is given by Eq. 5.3 (rearranged) where D is the distance from the observer to the occulting body:

$$\theta_{k+1/2} = \frac{\rho_{k+1/2} - r_{k+1/2}}{D} \tag{6.6}$$

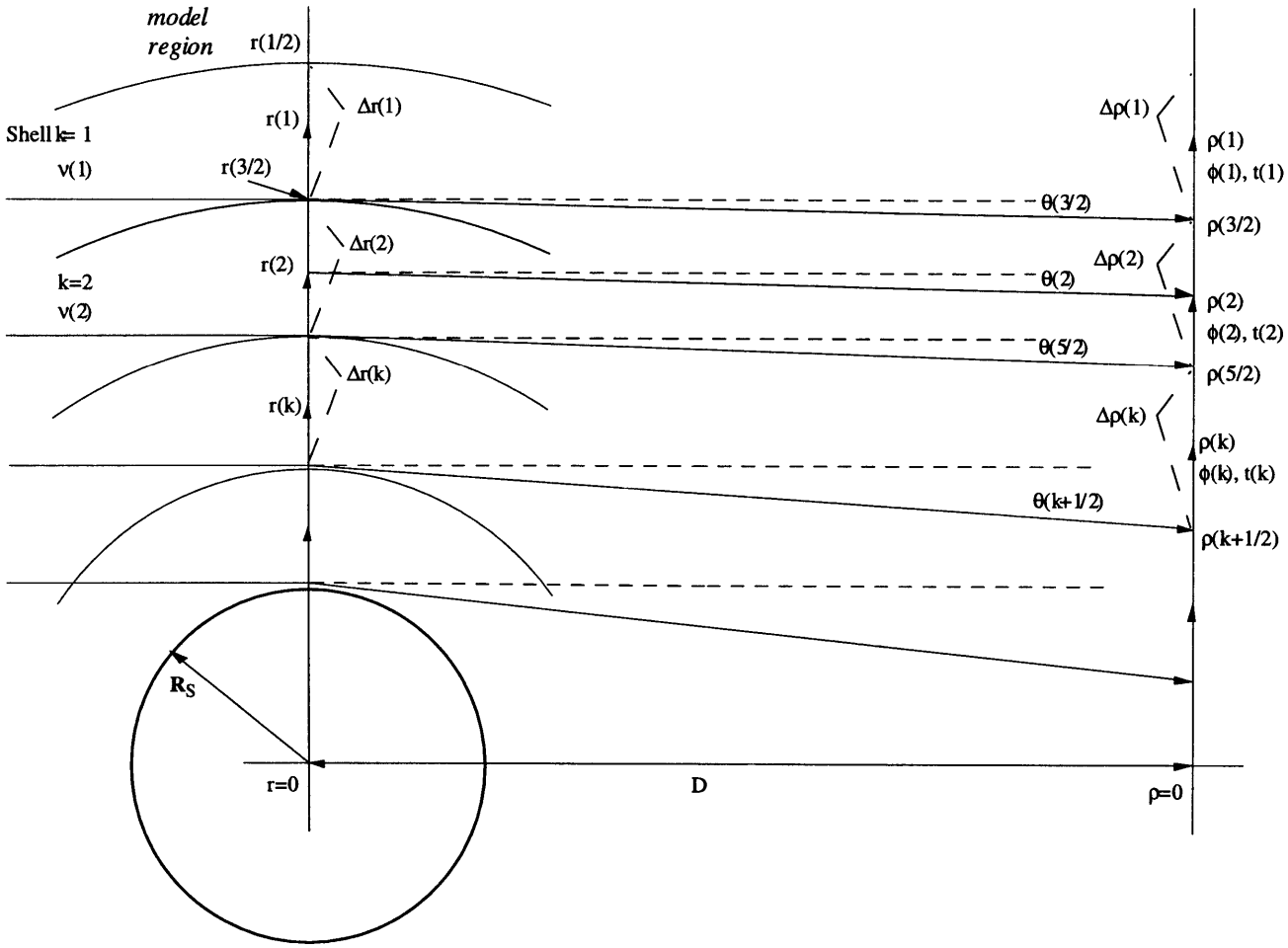

Figure 6.1 Atmospheric shells for the numerical inversion. The atmosphere is divided into spherical shells of uniform thickness. The integer indices refer to quantities at the midpoint of a shell, while conditions at the boundary are given by half indices. An isothermal model is fit to the occultation data above half-light to describe the upper part of the atmosphere [above the radius $r(1/2)$].

Because of noise, the flux ζ_k is occasionally negative. To avoid problems with negative flux, we bin the data, so that the shells correspond to at least a minimum radius interval Δr_S. This is significant only at the lower-flux levels of the light curve.

To derive the equation for the refractivity as a function of radius and refraction angle, we follow the method of Wasserman and Veverka (1973), without the large planet approximations. This gives:

$$\nu(r_{k+1/2}) = -\frac{1}{\pi}\left[I_\nu(r_{1/2}, r_{k+1/2}) + \sum_{j=1/2}^{k} \cosh^{-1}\left(\frac{r_j}{r_{k+1/2}}\right)\Delta\theta_j \right] \tag{6.7}$$

where

$$I_\nu(r_{1/2}, r_{k+1/2}) = \int_{\theta(r_{1/2})}^{0} \cosh^{-1}\left(\frac{r'}{r}\right) d\theta(r') \tag{6.8}$$

The summation in Eq. 6.8 refers to the contribution of the refractivity in the region of the inversion and I_ν is the contribution outside of the shells. The number density is derived from the refractivity, Loschmidt's number L and the refractivity of the gas at standard temperature and pressure ν_{STP}. We assume the composition is constant when we assume ν_{STP} does not vary with r.

$$n(r) = \frac{L\nu(r)}{\nu_{STP}} \tag{6.9}$$

The equation for the surface pressure is derived assuming hydrostatic equilibrium.

$$p(r_{k+1/2}) = -\frac{L\mu m_{amu} G M_p}{\pi \nu_{STP} r_{k+1/2}}\left[I_p(r_{1/2}, r_{k+1/2}) + \sum_{j=1/2}^{k}\left[\cosh^{-1}\left(\frac{r_j}{r_{k+1/2}}\right) - \sqrt{1-\left(\frac{r_{k+1/2}}{r_j}\right)^2} \right]\Delta\theta_j \right] \tag{6.10}$$

where I_p is the contribution above the first shell

$$I_p(r_{1/2}, r_{k+1/2}) = \int_{\theta(r_{1/2})}^{0}\left[\cosh^{-1}\left(\frac{r'}{r}\right) - \sqrt{1-\left(\frac{r}{r'}\right)^2} \right] d\theta(r') \tag{6.11}$$

The temperature is derived from the pressure and number density using the ideal gas law.

The integral equations (6.8 and 6.11) are evaluated by fitting an isothermal model to Triton's atmosphere above the section of the light curve to be inverted. We use Eqs. 2.2 and 4.5 of EY92 to get the refraction angle and radius above the inversion region. Fitting an isothermal model part way to define the initial conditions for the inversion was

shown to be an effective method by French *et al.* (1978). Unless otherwise stated, an isothermal model is fit to the half-light level, then the light curve is inverted below half-light. We begin the inversion at the half-light level so there is a sufficient data interval for the model fit to converge.

6.2 Tests of the Method

In this section, we demonstrate this inversion method retrieves an accurate temperature profile from a small body light curve. We start by applying the method described above to a synthetic isothermal light curve (without noise). The synthetic data were constructed from the model of EY92. The method retrieved the temperature profile to within 0.5% (or about 0.25 K).

Next, we added noise to our synthetic data. The random noise was added to make the light curve have a SNR per sec near that of the IRTF visible light curve. Figure 6.2 shows the retrieved and actual temperature profiles for the inversion of the noisy data. French *et al.* (1978) present the fractional error in scale height and pressure from a numerical inversion and give scaling equations to apply their results to other data. We used their scaling equations to derive the error in the inversion results.

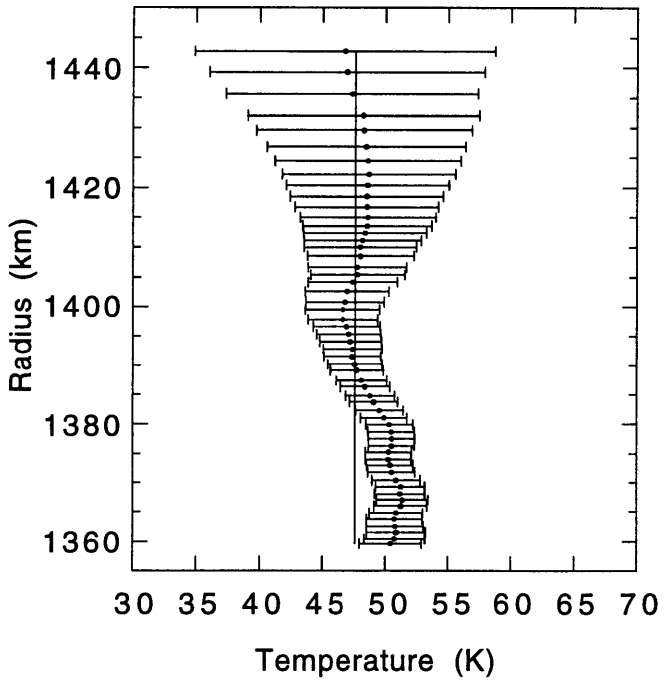

Figure 6.2 The retrieved and actual temperature profiles for an isothermal atmosphere. The solid line is the actual temperature profile of the data. The solid circles are the results from an inversion of noisy data (to simulate the IRTF-PCCD light curve). The retrieved temperature profile agrees to within one standard deviation with the actual profile above 1380 km radius.

Next, we will invert perfect (noiseless) synthetic data with a thermal gradient. Using the nominal Voyager model (Strobel *et al.* 1996), we constructed a synthetic light curve (see Chapter 7 for details). The inversion was carried out with two different initial

conditions: (i) using an isothermal model to define the atmosphere outside the retrieved region and (ii) using a model with a thermal gradient (Elliot and Young 1992). The retrieved and actual temperature profiles are shown in Figure 6.3. The profile represented by the dotted line used an isothermal model above the inversion level, and the profile represented by the dashed line used a power-law thermal-gradient model above the inversion level. The retrieved temperature profiles approaches the actual profile (solid line) at the lower radii for either case. For the Triton data, the error in the temperature profile at the start of the inversion is larger than the systematic error introduced by the choice of initial conditions.

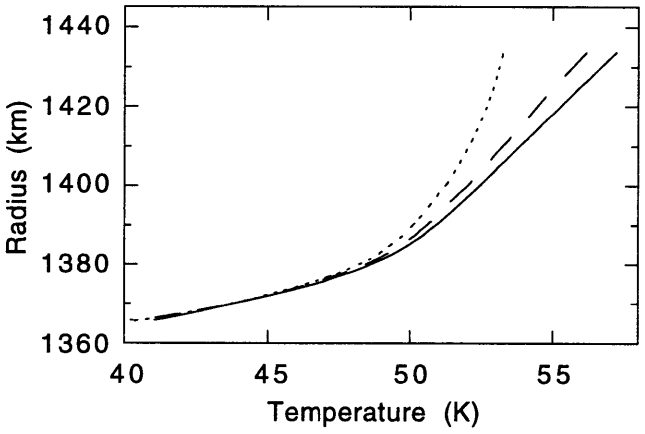

Figure 6.3 The retrieved and actual temperature profiles for an atmosphere with a thermal gradient. The solid line is the actual temperature profile. The dotted and dashed lines are the retrieved profiles for the isothermal and non-isothermal upper atmosphere models. The profiles agree at the lower levels, but disagree at higher radii due to the initial conditions.

We would prefer to fit a thermal gradient model to the upper level of the light curve but, with real (noisy) data the least-squares fit will not converge with a thermal gradient model (for example, fitting the half-light radius, energy ratio and power-law index of EY92) when fitting only to half light. Instead, an isothermal model is used.

6.2 Application To Triton Events

The highest SNR light curves were inverted using the method described above. The estimated far-limb flux (based on an isothermal model fit) was removed from the normalized light curve. The light curves were normalized using the background level defined by an isothermal model fit. To estimate the sensitivity of the results to the background level and far-limb flux model, we inverted the IRTF-PCCD light curve with different assumptions. The results of these inversions are shown in Figure 6.4. Five values of the background level were used in the normalization: (i) the nominal value, (ii) the nominal value plus one standard deviation from the formal error of the isothermal fit, (iii) the nominal value plus 1% of the occulted star's flux, (iv) the nominal value plus 2%

of the occulted star's flux, and (v) the nominal value plus 5% of the occulted star's flux. Only every fourth error bar is included to eliminate clutter in the figure. The curves fall within one standard deviation of the nominal inversion above 1390 km.

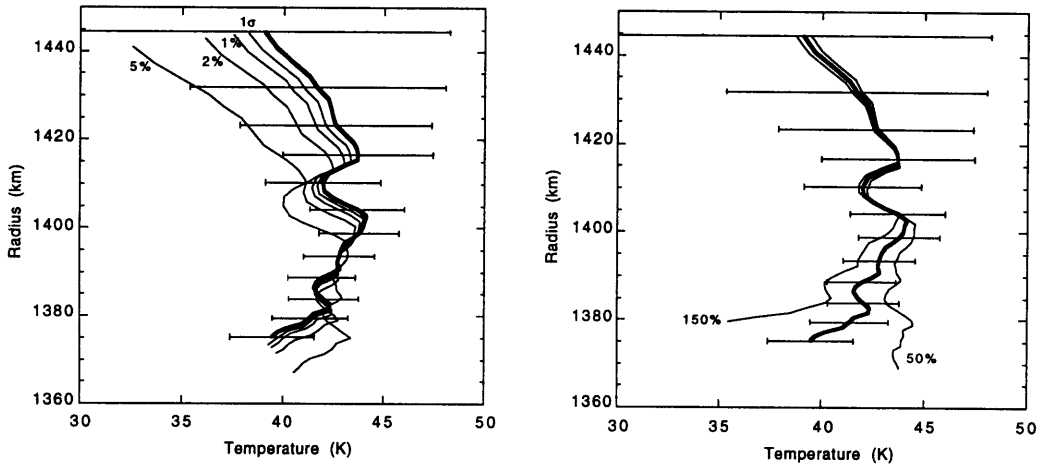

Figure 6.4 The sensitivity of numerical inversions to background calibration and the far-limb flux contribution. In both panels, the nominal inversion is the heavy line (an error bar is shown on every fourth point). On the left, the other four curves correspond to the nominal background level increased by 1σ, and 1%, 2% and 5% of the unocculted star's flux. On the right, the two thin lines correspond to subtracting 50% of the model far-limb flux, and 150% of the model far-limb flux, instead of the nominal value (100%).

The sensitivity to the far-limb flux removal was tested by inverting the IRTF-PCCD light curve for different amounts of far-limb flux (50%, 100% and 150% of nominal). The results are in the right panel of Figure 6.4. At the lowest levels, the solutions diverge. At these radii, the contribution of the far-limb flux is most significant. At 1390 km, a 50% error in far-limb flux model will causes a 2 K temperature difference. Because of the sensitivity of the solutions to both the background level and far-limb flux removal, we will stop the inversions at a radius of 1390 km.

The temperature profiles from the numerical inversions of the highest SNR light curves are shown in Figure 6.5. The nominal Voyager model of (Strobel *et al.* 1996) is shown for comparison. All the light curves, except the IRTF, are consistent with the temperature profile of the nominal Voyager model. The IRTF temperatures are consistently colder by more than 5K at the lowest radii and the temperature profile is consistent with an isothermal model.

Figure 6.5 shows why the isothermal model fits of Chapter 5 matched the data so well. While most of the chords are consistent with the nominal Voyager model, the error

bars are large enough to accommodate an isothermal model in most cases also. Higher SNR data are required to decrease the error bars, so we can retrieve a more definitive temperature profile.

The retrieved pressure profiles are shown in Figure 6.6. Below 1410 km, all the pressure profiles (except the IRTF-PCCD) are higher than the nominal Voyager model. For the IRTF-PCCD chords, the retrieved pressure is less than the model pressure at the largest radii, and less than the model at the lowest radii. In both the temperature and pressure profiles, there is no significant difference between the 1993 and 1995 results.

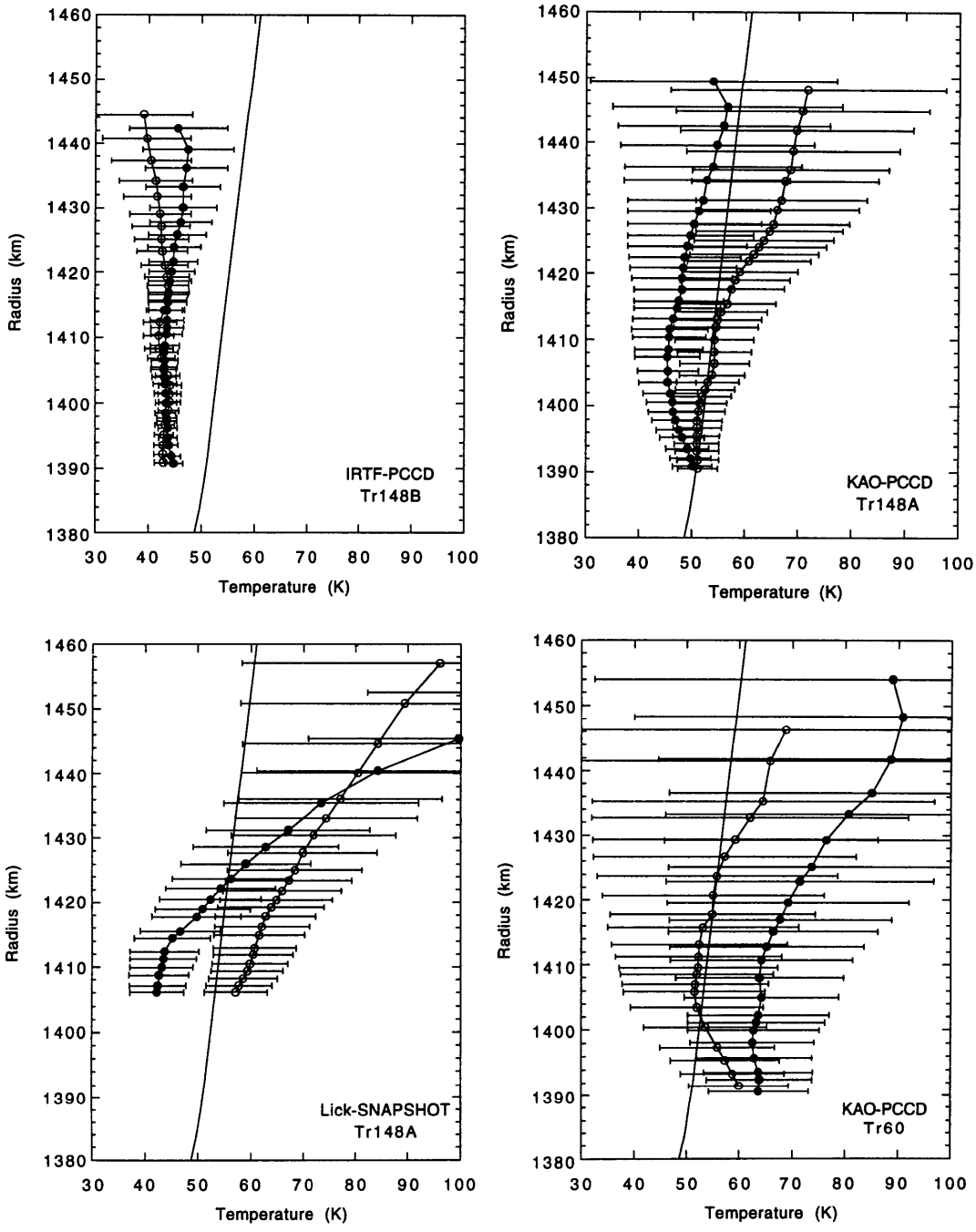

Figure 6.5 Temperature profiles. The immersion and emersion temperature profiles from 4 datasets are shown. The immersion results are depicted by open circles and emersion by solid circles. The error bars are one standard deviation. The solid line is the nominal Voyager model (Strobel *et al.* 1996). All temperature profiles, except for the IRTF-PCCD, are consistent with the model.

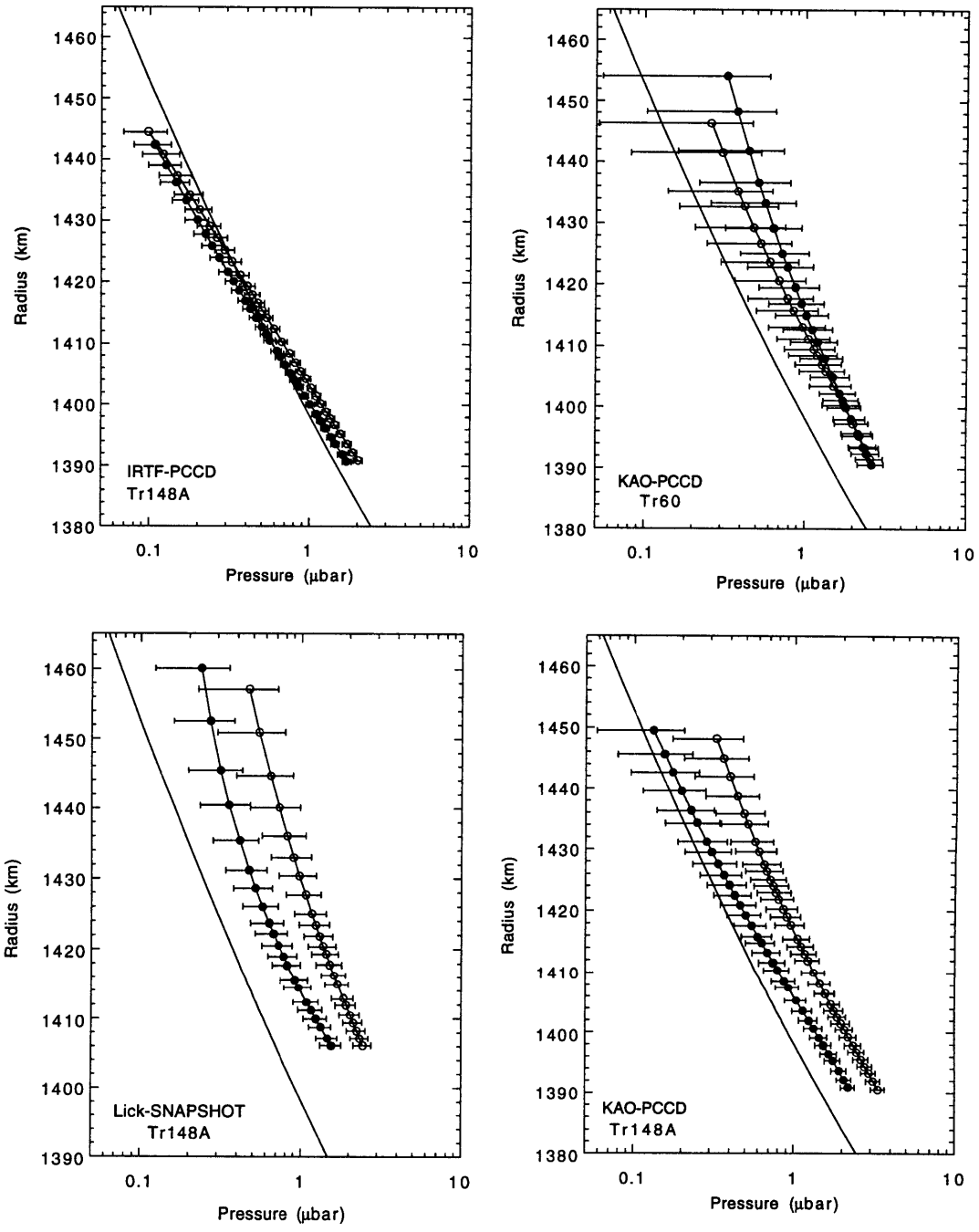

Figure 6.6 Pressure profiles. The immersion and emersion pressure profiles from four datasets are shown. The immersion results are depicted by open circles and emersion by solid circles. The error bars are one standard deviation. The solid line is the nominal Voyager model (Strobel *et al.* 1996). At the lowest radii, all pressure profiles are higher than the model.

In the last chapter, we showed there was a difference between the immersion and emersion chords in the IRTF light curve. Why do we not see the asymmetry in the

temperature and pressure profiles for these chords? The asymmetry is the most obvious near the central flash and at the lowest flux levels. We stopped the inversion above this radius because of the sensitivity to the far-limb flux removal and the background subtraction. Figure 6.7 shows the IRTF light curve as a function of radius probed (instead of time).

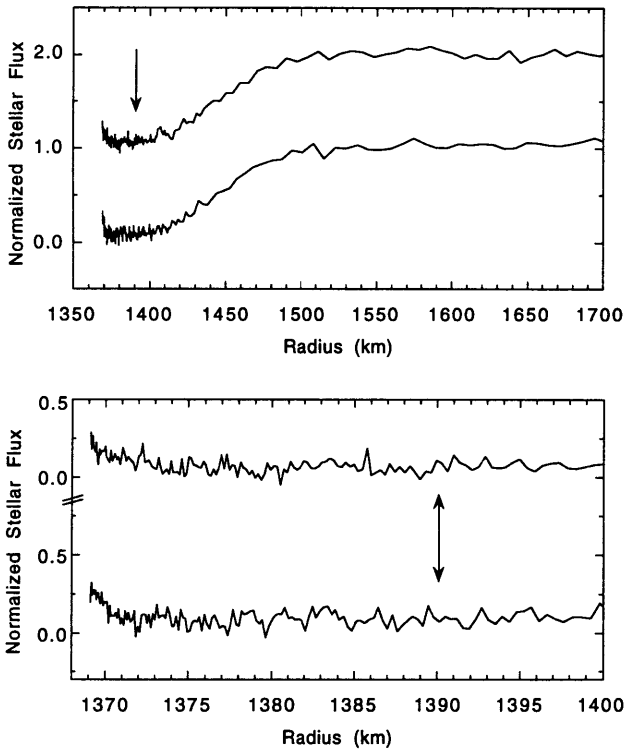

Figure 6.7 The IRTF light curve vs. radius in Triton's atmosphere. In both panels, the immersion chord is offset by (+1.0) relative to the emersion, for display purposes. The top panel shows the light curve from the minimum radius probed (1369 km) to 1700 km where the stellar flux is 1.0. The lower panel is an expansion of the region from 1369 km to 1400 km. The asymmetry is evident in the slope of the central flash (near 1370 km). This is significantly below the lowest radius included in the inversion, indicated by arrows. Equal intervals in time correspond to smaller intervals in radius as the atmosphere becomes denser. This is a result of the differential refraction.

To ensure that there is no bias in the inverted solutions due to the initial conditions, we inverted the IRTF-PCCD immersion light curve using initial conditions based on the Strobel *et al.* (1996) model. The Strobel *et al.* model was converted to a synthetic light curve (with no noise added) using the impact parameter, shadow velocity and integration time of the IRTF-PCCD data. This immersion section of this synthetic light curve (only data above half-light) was fit using a clear, isothermal, deep-atmosphere model. From this model fit, we derived the initial conditions for the numerical inversion (the radius and refraction angle at the start point of the inversion–half-light) and the atmospheric structure above the inversion region (as needed in Eqs. 6.8 and 6.11). This was repeated using a power-law thermal gradient model (Elliot and Young 1992). The resulting temperature and pressure profiles are given in Figure 6.8.

At the beginning of the inversion (half light) the retrieved temperature and pressure profiles are close to the Strobel *et al.* model, but at lower radii the temperature

and pressure profiles with the three different initial conditions converge. At the lowest levels, the retrieved profiles are not influenced by the initial conditions of the inversion. Even using initial conditions based on the Strobel *et al.* model, we do not retrieve the model temperature and pressure profiles. Specifically, the atmospheric pressure is greater than the model at the lowest level shown in the figure, where the inversion is least sensitive to initial conditions (and before the inversion is sensitive to the background calibration and far-limb flux removal).

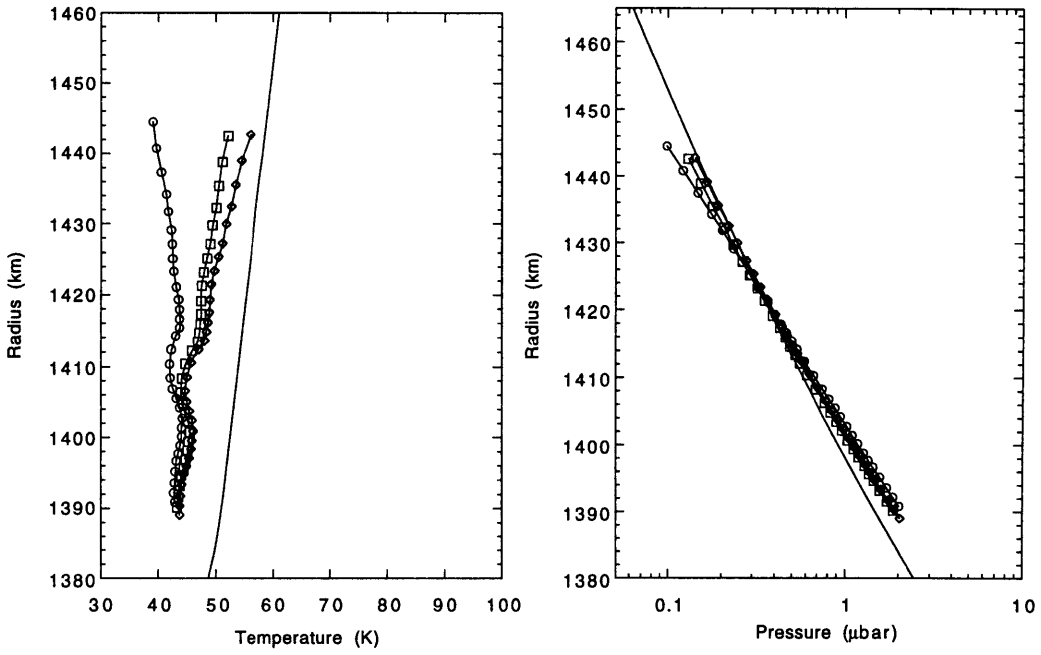

Figure 6.8 Temperature and pressure profiles using Strobel *et al.* model for initial conditions. The nominal immersion profiles (using an isothermal model fit of the data to get the initial conditions) are depicted by open circles. The profiles from the inversion with initial conditions based on the isothermal and power-law thermal gradient fits of the synthetic light curve (based on the Strobel *et al.* model) are depicted by the squares and diamonds. The solid line is the nominal Voyager model (Strobel *et al.* 1996). Error bars are not shown (to eliminate clutter in the figure), but the figures are on the same scale as Figures 6.5 and 6.6, so one can refer to them for an estimate of the one standard deviation errors.

7. Comparison with a Physical Model

In this chapter we compare these stellar occultation data to a model of Triton's atmosphere (based on Voyager data). The model we shall use for comparison is Strobel *et al.* (1996), hereafter S96 (we use the term "the nominal Voyager model" to represent the nominal Strobel *et al.* model and the term "S96 model" to represent the radiative-thermal conduction model of Strobel *et al.* with non-nominal values for the input parameters). We could transform the model into an occultation light curve, and visually compare the model and observed light curves. This technique would be useful only for investigating large differences, and we can do better. Instead, we will use a least-squares fit of the model to the occultation data to estimate physical parameters and their errors. This is a more rigorous method for comparing a physical model and occultation data. We expect the physical model fits to give a more accurate description of the atmospheric structure than the isothermal models, since it should be a better description of the atmosphere.

This will be a good test of the model, since it is based on observations that determine conditions at higher and lower altitudes. In the S96 model, the heat input into Triton's upper atmosphere is adjusted to match the isothermal temperature derived from the UVS solar occultation (~100 K). The heat is conducted downward from the ionosphere. There is radiative cooling by CO and HCN. The S96 radiative-thermal conduction model stops at an altitude of 8 km, where the troposphere model of Yelle *et al.* (1995) is attached. The temperature and pressure at the surface (r_S=1352 km) in the nominal model are specified at 38 K and 14 μbars with the temperature following the adiabatic lapse rate in the lowest 8 km (0.125 K/km) to give a temperature of 37 K at the tropopause. Unlike the models we fit in Chapter 5, the temperature profile of the S96 model is not a simple analytic function. Therefore, we need a new method for fitting this model to the occultation data.

First, we describe the method for fitting a physical (non-analytical) model to the occultation light curve. Next, we address what we can learn from such a comparison and the sensitivities to different model parameters. Finally, we apply the method to Triton occultation data.

7.1 The Method

The first step is to determine model parameters for fitting. This entails understanding the model to determine which parameters change the atmospheric profile in

the microbar region. It is critical that the physical model is as complete a description of the atmosphere as possible since the formal errors from least-squares fitting do not account for systematic errors in the model.

For each free parameter in the fit, a set (or grid) of model atmospheric profiles are needed. The profiles contain the number density $n(r)$ and its first and second derivatives ($dn(r)/dr$, $d^2n(r)/dr^2$) with radius. If there are n grid points and m model parameters, then n^m model atmospheres are needed.

The n^m profiles of number density and derivatives are converted to a refractivity $\nu(r)$ with Loschmidt's number, L, and the appropriate refractivity at standard temperature and pressure, ν_{STP}.

$$\begin{aligned} \nu(r) &= \frac{\nu_{STP}}{L} n(r) \\ \frac{d\nu(r)}{dr} &= \frac{\nu_{STP}}{L} \frac{dn(r)}{dr} \\ \frac{d^2\nu(r)}{dr^2} &= \frac{\nu_{STP}}{L} \frac{d^2n(r)}{dr^2} \end{aligned} \tag{7.1}$$

Interpolation functions of the refractivity and its derivatives are formed. Given a radius and values for the atmospheric parameters, the refractivity and its derivatives can be calculated from the interpolation functions. From a given atmospheric profile, we calculate the observed flux in the shadow plane $\phi(\rho)$, using the equations in Elliot and Young (1992) with an extension to include the far-limb flux. See Chamberlain (1996) for a complete description of how to convert a grid of atmospheric profiles into a model occultation light curve.

This method of physical model fitting was tested with synthetic light curve data. A grid of atmospheric refractivity profiles was created from the two-limb, clear-atmosphere isothermal models presented in Chapter 5. From the grid of profiles, model atmospheres were constructed using the method outlined above and compared with synthetic data based on the isothermal models. We found agreement between the models and synthetic data to about 0.15% of the occulted star flux, which is much below the noise level in the best data.

7.2 What we can learn

What do we expect to learn from a physical model fit? From isothermal model fitting of occultation light curves, we establish the radius at a given flux level (typically half light) and the scale height of the atmosphere. The radius defines a reference level for

the system and the scale height is related to the mean molecular weight, temperature and temperature gradient in the atmosphere (see Eq. 5.11).

From a physical-model fit, we would expect to derive similar parameters. For example, the atmospheric pressure (or density) at a specified level is similar to the half-light radius. Finding a parameter similar to the scale height depends on the specific model. Potential parameters for fitting include the mean molecular weight or parameters directly controlling the temperature and temperature gradient in the atmosphere. Such parameters may include the concentration of molecules contributing to the radiative transfer, or parameters controlling the amount of heat input. However, as in the analytic models, we can not discriminate between a change in molecular weight, temperature and temperature gradient without outside information. For example, in a fit for molecular weight, the result will be correct only if the temperature and temperature gradient in the model are correct. Otherwise, the fitted molecular weight will be biased by the errors in the thermal structure, and these errors will not be reflected in the formal error from the fit, since this is a systematic error. In the next section, we discuss specific parameters of the S96 model.

7.3 Sensitivities

When searching for model parameters that can be constrained by the occultation data, it is necessary to choose parameters that affect the observed flux. If a parameter is known exactly by other means, then it can be fixed. The parameters of the S96 model that are candidates for fitting include: (i) heating from the precipitation of magnetospheric electrons, (ii) CO mixing ratio, (iii) surface temperature, (iv) surface pressure, and (v) mean molecular weight. We briefly discuss each of these and indicate if the parameters are similar to either scale height or half-light radius in the analytic models.

The temperature in Triton's upper atmosphere (~100 K between 500-700 km altitude) determined from the Voyager UVS occultation data (Broadfoot *et al.* 1989) is higher than one would expect based on heating from the Sun alone (Stevens *et al.* 1992). Stevens *et al.* (1992) demonstrate that power input from Neptune's magnetosphere can provide the extra heat. The nominal amount of magnetospheric power dissipation needed to match the Voyager UVS occultation data is 1.4×10^{8} W. The actual amount of magnetospheric power dissipation is uncertain (Krasnopolsky and Cruikshank 1995) and could vary with time, so this is a potential parameter for fitting. A change in the magnetospheric power dissipation would affect the thermal gradient, and therefore the number density scale height.

The CO mixing ratio is another parameter of the model that could be fit. The partial pressure of CO is 7% of the partial pressure of N_2 at 38K, so we would expect this molecule to be present in the atmosphere. Voyager observations set an upper limit of 0.01 on the mixing ratio of CO (Broadfoot *et al.* 1989). Cruikshank *et al.* (1993) detected the (2-0) CO overtone band, and derived a model with the CO and N_2 ices intimately mixed. From this model, they established that there was 0.1% CO in the intimate mixture. Using Raoult's law, this gives an atmospheric mixing ratio of 7×10^{-5}. Changes in the amount of CO in the atmosphere will affect the temperature and temperature gradient by changing the cooling rate. These differences would be seen as a change in scale height with the analytic model.

The surface temperature has been established at $38.0^{+2.0}_{-1.0}$ (Tryka *et al.* 1993) from the shape of the N_2 ice band, but even this small uncertainty in temperature translates into a large uncertainty in surface pressure. The ±1 standard-deviation range of temperatures translates to a surface pressure of 10-58 μbars for vapor pressure equilibrium of N_2 (Brown and Ziegler 1980). The surface pressure has been predicted to change with varying season due to changing insolation (Hansen and Paige 1992; Spencer and Moore 1992). This makes surface pressure a good parameter for fitting. A temperature change would cause a scale height change in the analytic models, while a pressure change would show up as a change in half-light radius.

With the physical model, we cannot simply change the temperature in the region we are probing, but we can mimic a temperature change through the mean molecular weight. If we fit for molecular weight and found a value different from the nominal Voyager model, this would indicate either a temperature difference, temperature gradient difference or a mean molecular weight difference. We cannot rule any of these out.

From the above discussion, magnetospheric heating, CO mixing ratio, surface pressure and molecular weight are four potential free parameters for the least-squares fit. Next, we examine these parameters to see if we could detect changes in these parameters with stellar occultations. Light-curve flux is related to the first and second derivative of number density through the refraction angle and its derivative (EY92). If the density derivatives at the microbar pressure levels are sensitive to changes in a parameter, then the light curves will be sensitive to changes in that parameter also. In Figure 7.1, we show the number density and its derivatives for different values of surface pressure and different values of mean molecular weight. Figure 7.2 shows the density and its derivatives for different values of the CO mixing ratio and magnetospheric heating. The model

atmospheres are displayed from the surface radius [assumed to be 1352 km (Davies *et al.* 1991)].

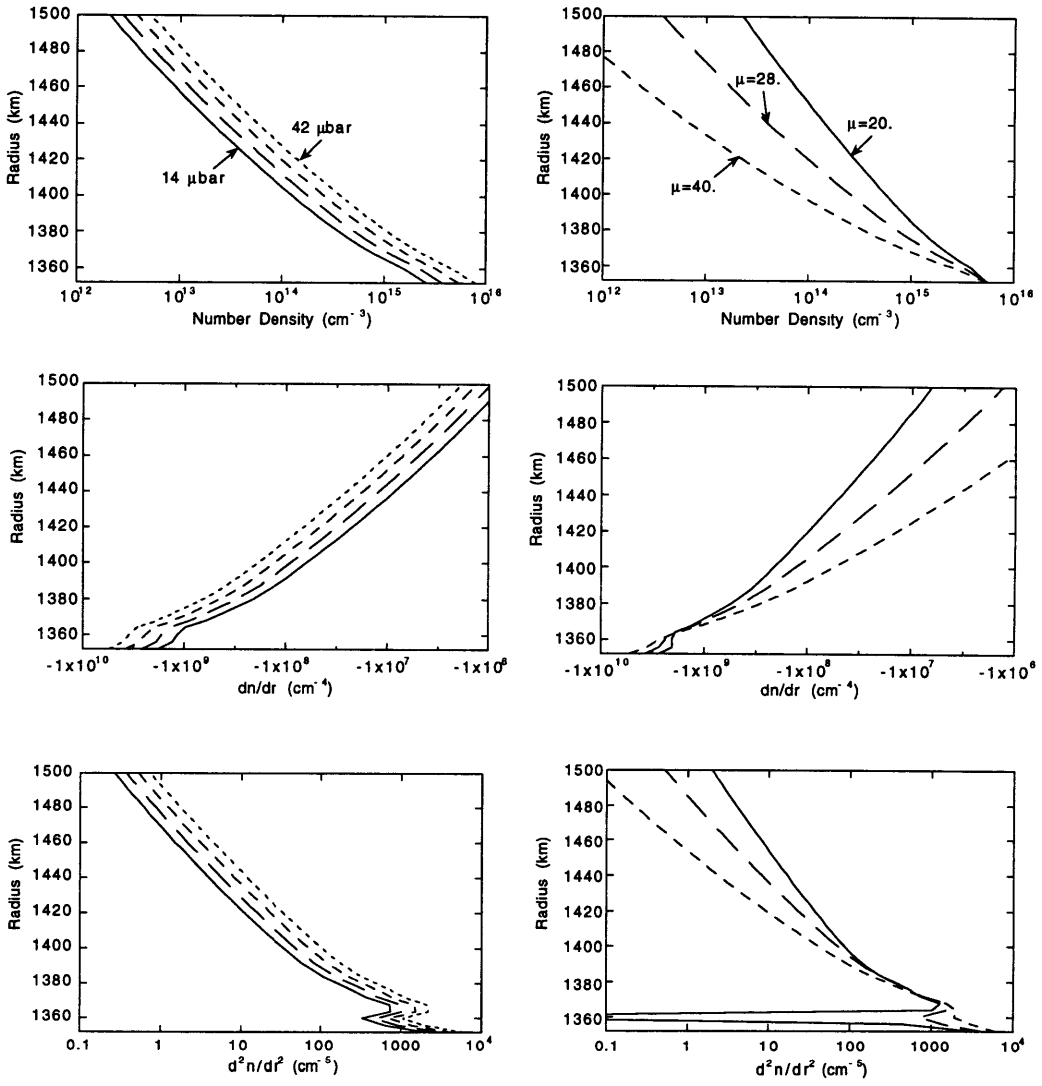

Figure 7.1 Density and density derivatives for surface pressure and molecular weight. Four values of surface pressure (14, 20, 29 and 42 μbar) are shown on the right. Three values of molecular weight (20, 28 and 40) are shown on the left. The occultation light curves will be sensitive to these parameters because the density derivative profiles are affected by changes in the parameters.

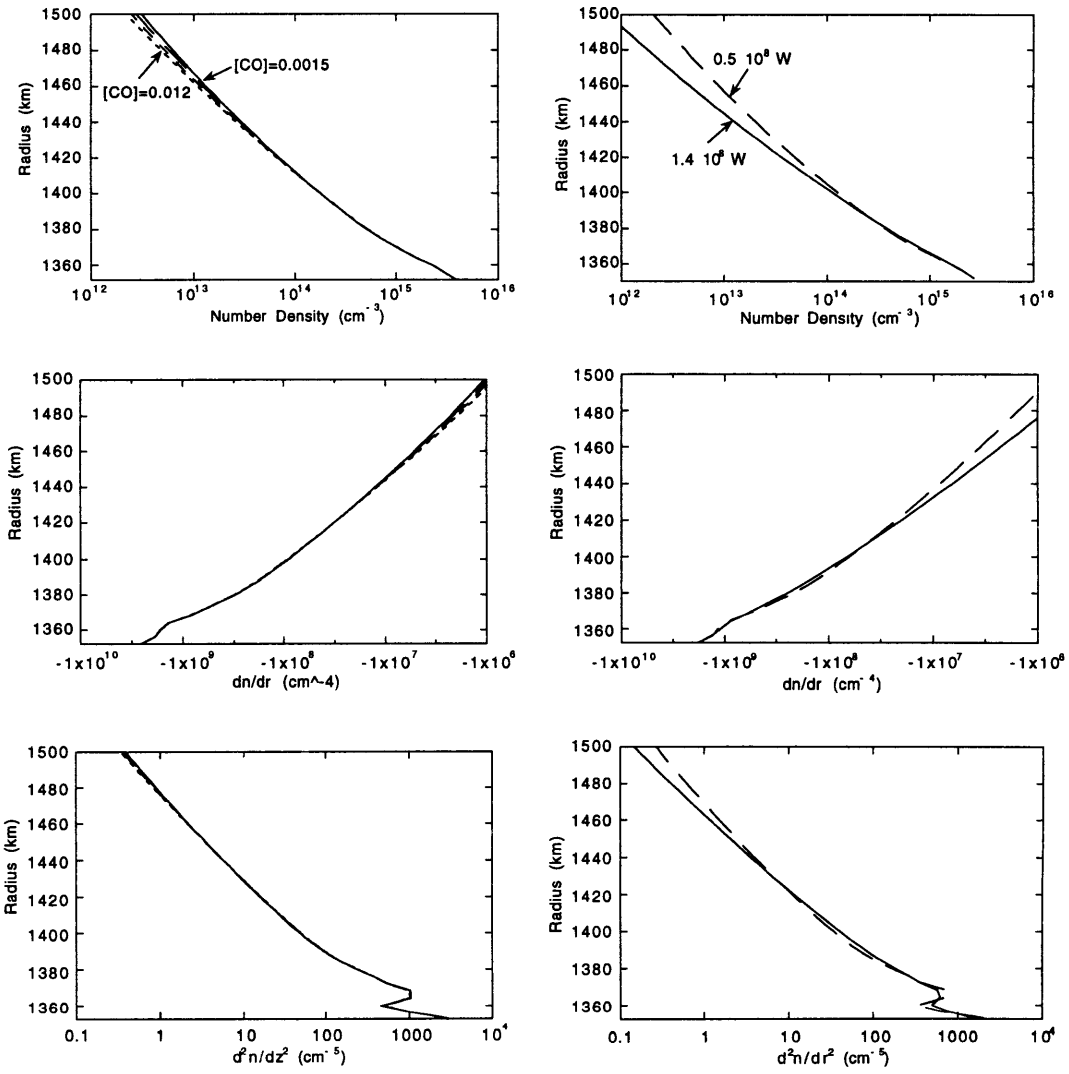

Figure 7.2 Density and density derivatives for CO mixing ratio and magnetospheric power dissipation. Four values of CO mixing ratio (0.0015, 0.003, 0.006, 0.012) and two values of magnetospheric power dissipation (0.5×10^8 W and 1.4×10^8 W) are displayed on the left and right. These two values of magnetospheric power dissipation correspond to a temperature at 400 km altitude of 69 and 100 K. The occultation light curves will not be sensitive to the CO mixing ratio because the density derivatives in the microbar pressure region do not vary with the CO mixing ratio. The occultation light curves will not be as sensitive to the magnetospheric heating as the surface pressure or molecular weight because the density derivatives do not vary as strongly. Any change in magnetospheric heating would be masked by uncertainties in the surface pressure.

From the variation of the density derivatives we can see that surface pressure and molecular weight are the best model parameters for fitting. In fitting for mean molecular weight, we are not including all the effects from having another molecular component in the atmosphere. In particular, any new constituent is assumed to be radiatively inert to cause minimum changes to the radiative-thermal conduction model, and we are not changing the refractivity of the atmosphere from the pure N_2 case.

7.4 Application to Occultation Data

In this section, we present results of the physical model fitting for both atmospheric pressure and molecular weight, but first we will discuss some assumptions in the implementation that are specific to Triton and this model. We assume that refraction is the only process dimming the starlight. Extinction of the starlight could be added, but the fit results do not suggest it is necessary. Also, the effects of general relativistic bending of the starlight due to Triton (or Neptune) have been neglected. It is the differential bending of the starlight over the height of the atmosphere that is important and this change is 0.07 km from Triton and 0.007 km from Neptune at the distance of Earth. This is much less than the bending due to atmospheric refraction, which is approximately one scale height, 20 km, at the half-light radius (Baum and Code 1953) and increases with depth. We also assume the composition is constant, and we use the refractivity of N_2 at standard temperature and pressure to convert the number density to refractivity.

The S96 atmospheric profiles (provided by X. Zhu) describe the atmosphere from a radius of 1352 km to 2156 km, with an increment of 4 km. The atmosphere above 1800 km contribute less than one part in 10^5 to the dimming of the occulted star, so we used only the atmosphere below this radius in our fits (to speed up the computation).

We performed physical model fits to the same light curves inverted in Chapter 6– the highest SNR occultation data from the Tr148 event and the one light curve from the Tr60 occultation. The light curves were fit for the background and full flux levels, a slope, midtime and either one or two physical parameters. The impact parameter was fixed at the adopted value. Initially, we fit for the pressure at 1400 km with the mean molecular weight fixed at 28. The atmospheric density (and density derivative) profiles used in this fit are shown in Figure 7.1. The pressure of these profiles at 1400 km was 0. 92, 1.30, 1.86 and 2.65 μbar. The results are given in Table 7.1. Although the occultation did not probe to the surface, we can estimate the surface pressure using the S96 model to relate the pressure at 1400 km to the pressure at the surface.

Table 7.1 Physical Model Fits

Occultation	Light Curve	P_{1400} (μbar)	Surface Pressure (μbar)	Molecular Weight	χ^2_ν (Phy. fits)	χ^2_ν (Iso. fits)
Tr60	KAO	1.97 ± 0.09	30.8 ± 1.4	28.0	0.669	0.674
Tr148B	IRTF-PCCD	1.95 ± 0.10	30.5 ± 1.7	28.0	1.043	0.979
Tr148A	KAO	1.73 ± 0.14	27.0 ± 2.3	28.0	0.959	0.959
Tr148A	Lick	2.03 ± 0.19	31.9 ± 3.1	28.0	0.844	0.848
Tr60	KAO	1.72 ± 0.32	26.8 ± 5.1	27.2 ± 1.4	0.669	0.674
Tr60[a]	KAO	1.95 ± 0.09	30.5 ± 1.5	29.05	0.670	0.674
Tr148B	IRTF-PCCD	2.39 ± 0.13	37.7 ± 2.1	30.4 ± 0.4	1.017	0.979
Tr148B[b]	IRTF-PCCD	1.83 ± 0.07	28.6 ± 1.1	30.5 ± 0.4	0.979	0.979
Tr148A	KAO	1.92 ± 0.23	30.1 ± 3.8	29.0 ± 0.8	0.958	0.959
Tr148A	Lick	2.34 ± 0.36	36.8 ± 5.8	29.1 ± 0.8	0.843	0.848

[a]fixed molecular weight.

[b]fitted impact parameter, see text.

The physical model provided a good fit to the KAO and Lick (Tr148A) light curves. The χ^2_ν for these fits are equal to the values from the isothermal fits (the χ^2_ν for the adopted isothermal fits to each dataset are given in column 7 of Table 7.1 for reference). The IRTF light curve, however, is not fit as well by the physical model. In particular, there is a significant mismatch between the data and model at the central flash. Figures 7.3 and 7.4 show the data and best-fitting physical model and best-fitting isothermal model for the KAO and IRTF-PCCD light curves.

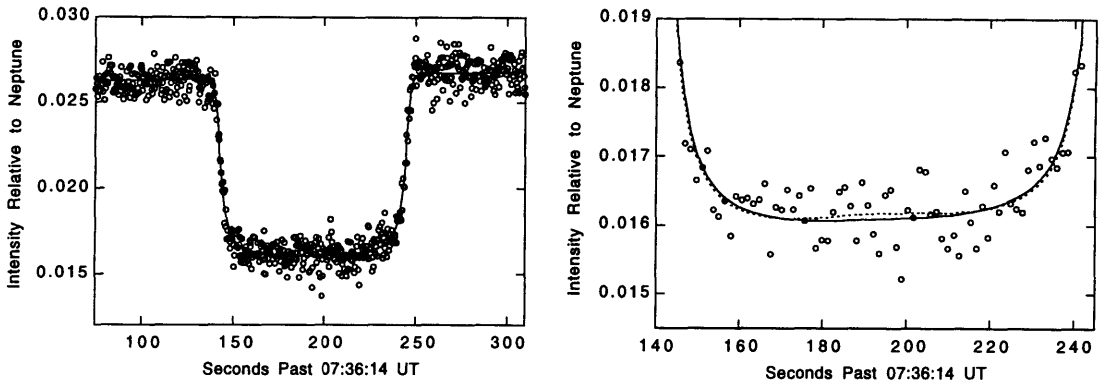

Figure 7.3 KAO light curve data and models. In both panels, the data (circles), isothermal model (dotted line) and physical model (solid line) are displayed. The data and models are averaged by 4. Both models provide a good fit to the data. The right panel is an enlargement of the lower section of the light curve.

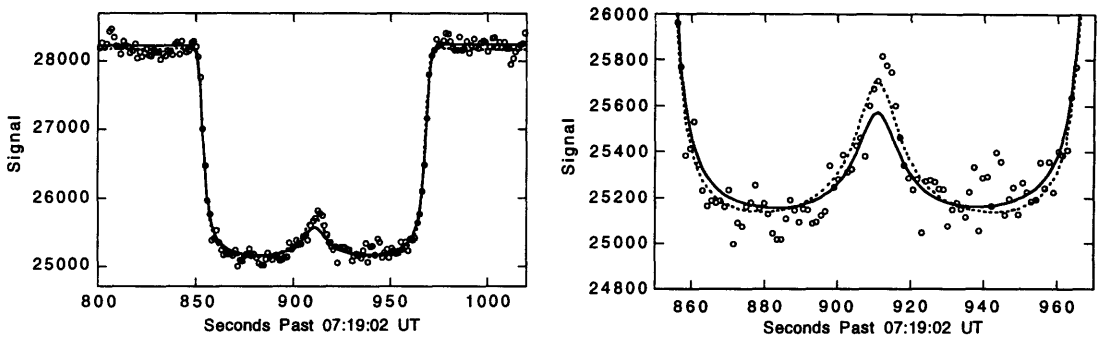

Figure 7.4 IRTF light curve data and models. In both panels, the data (circles), isothermal model (dotted line) and physical model (solid line) are displayed. The data and models are averaged by four. The right panel is an enlargement of the lower section of the light curve. The best fit physical model does not match the central peak flux of the data. The difference between the isothermal model and the physical model is much larger than in the KAO data (Figure 7.3). Any deviation of the two models is made larger by the focusing with smaller shadow-plane radius.

As seen in the figure, the central-flash peak is not fit well by the physical model. In an attempt to improve the fit to the central flash, we extended the model to fit for molecular weight, since the central-flash flux is sensitive to the scale height and impact parameter (and the scale height is a function of molecular weight). We expanded our number of fitted parameters from one to two. This required more S96 model profiles. For each of the four surface pressures, two more profiles were added to the grid. These

new profiles had a mean molecular weight of 20 and 40. In these fits we are fitting for the surface pressure, and the pressure at 1400 km was derived from the model. The fit results are the same regardless of whether one is fitting for the pressure at 1352. km (the surface) or at 1400 km because the model strictly relates the two. Table 7.1 shows the fitted values of the surface pressure and molecular weight. Again, we get good fits to the KAO and Lick data, but not the deeper probing IRTF-PCCD data.

In an attempt to match the IRTF-PCCD data another fit was performed. This time the impact parameter, surface pressure and molecular weight were allowed to be free parameters. This fit had a better match to the central-flash flux, as can be seen by the lower χ^2_ν (Table 7.1). However, the fitted value of the impact parameter is two standard deviations away from the astrometric solution. It is unlikely that the astrometric solution is 2σ from the real impact parameter. The half-light times define the length of the occultation chord. Table 7.2 shows the change in chord length if the Tr148B chords are shifted by 52.2 km as the physical model fit would imply. The chord length of the more central chords is affected less. Column 3 of the table gives the change in chord length converted to seconds of time, and column 4 translates that to the number of standard deviations given the error in the chord timing presented in Chapter 4. For all chords, this is more than one standard deviation change from the astrometric solution. The nominal astrometric solution is driven by the IRTF timings since the astrometric solution was derived from a weighted fit and the IRTF times have the smallest error. However, even without these times (as mentioned in Chapter 4), the astrometric solution changes by less than 1 km. The impact parameter from the physical model fit is not consistent with the light curve timings; therefore, this solution is not credible.

Table 7.2 Chord Length Difference

Light Curve	$\Delta\rho$ (km)	Δt (sec)	$\Delta t/\sigma_t$
IRTF	8.9	0.36	3.2
Lick	56.4	2.3	2.0
Lowell	17.7	0.71	1.4

Returning the light curves that were well fit by the physical model, we shall compare the pressure at 1400 km from 1993 and 1995. Using the weighted average pressure from the KAO-Tr148A and Lick-Tr148A fits, we determine a pressure at 1400 km representative of the atmosphere during the 1995 occultation. For the nominal molecular weight (28), the observed change in surface pressure between 1993 and 1995 is

-2.1 ± 3.7 μbar (-1.0 ± 1.8 μbar/yr). If the mean molecular weight of the atmosphere is close to 29 μbar, then the observed change in surface pressure is 1.6 ± 5.0 μbar. In either case, there is no detectable change in surface pressure between the two events.

We can place limits on the seasonal change per year. For the nominal molecular weight, Triton's surface pressure is increasing by less than 4.4 μbar/yr and decreasing by less than 6.3 μbar/year. These are 3σ limits.

7.5 Conclusions from the Physical Model Fitting

We have described a method for fitting a physical model to stellar occultation data and applied this to the highest SNR 1993 and 1995 Triton occultation data using the method of Strobel *et al.* (1996). We demonstrated that the occultation light curves are most sensitive to a change in the model of surface pressure and mean molecular weight. The mean molecular weight parameter can indicate a change in molecular weight, temperature or temperature gradient since we are only sensitive to scale height.

The physical model fit the KAO and Lick-Tr148A occultation light curves as well as the isothermal models. But the IRTF-PCCD light curve was better fit by the isothermal model than the physical model. This is consistent with the isothermal temperature profile derived from numerical inversions for this data, and the power-law thermal gradient fit of Chapter 5 that showed the temperature structure to be isothermal. This data has the highest SNR and small differences in the atmospheric structure will be amplified at the central flash due to focusing; therefore, this data is more sensitive to the atmospheric structure than the other data.

The pressure derived from the model fits is consistently higher than the nominal S96 model (based on Voyager data). This is also consistent with the numerical inversion results. The implications of the higher pressure will be addressed in Chapter 8.

From the stellar occultation observations (which span only two years), we see no evidence of seasonal change in the region probed by these occultation observations (microbar pressure level, about 20 to 100 km altitude). Using the Strobel *et al.* model to relate the conditions at this level to the surface, we limit the increase in surface pressure to be less than 4.4 μbar/yr (3σ) and the decrease in surface pressure to be less than 6.3 μbar/yr (3σ).

8. Discussion

8.1 Atmospheric Pressure near 1400 km radius

From two analysis methods (numerical inversions and physical model fits), we have shown the pressure in Triton's atmosphere near 1400 km radius (~50 km altitude) to be larger than that of the nominal Voyager model (Strobel *et al.* 1996). Are the isothermal model fits also consistent with a higher pressure than the nominal Voyager model? To make this comparison, we fit an isothermal model to synthetic data made from the nominal Voyager model to derive the equivalent isothermal temperature and pressure. The equivalent isothermal temperature and pressure will be sensitive to the radius level probed, so four different light curves were constructed to simulate the four highest SNR light curves (using the impact parameter, shadow plane velocity, and integration time of the datasets). The pressure at 1400 km derived from the isothermal model fits of the synthetic data is presented in Table 8.1. The pressures determined from the observed light curves are also presented (from Tables 5.4 and 5.6). As we found with the other analysis methods, the pressure at 1400 km is consistently higher than that of the nominal Voyager model.

Table 8.1 Pressure at 1400 km from Isothermal Fit of Data and Model[a]

		P_{1400}		
Observatory	Event	Immersion	Emersion	NVM[a]
KAO	Tr60	1.5 ± 0.1	1.5 ± 0.1	0.68 ± 0.02
IRTF[b]	Tr148B	1.2 ± 0.1	1.3 ± 0.1	0.50 ± 0.02
KAO	Tr148A	1.5 ± 0.3	1.5 ± 0.3	0.76 ± 0.01
Lick	Tr148A	1.9 ± 0.5	1.8 ± 0.5	0.81 ± 0.01

[a]Nominal Voyager Model (NVM). The error in the pressure from the fits to the NVM are a result of the mismatch between the real atmospheric structure and the isothermal form assumed (no noise was added to the model).

[b] PCCD

Using all three analysis methods, we see a greater atmospheric pressure than predicted by the nominal Voyager model near 1400 km. There are three possible explanations for this difference: (i) the atmospheric pressure has increased between 1989 and these stellar occultations, (ii) the surface radius is larger than the value adopted in the model, and (iii) the atmospheric structure at the microbar level is not properly modeled.

Any combination of these could explain the observational results. We will discuss each of these possibilities.

First, we will address the issue of seasonal change. There are "minor" and "major" seasons on Triton due to the complex motion of Triton's subsolar point (Trafton 1984). Currently, Triton is experiencing a major summer in the southern hemisphere (between the 1993 and 1995 stellar occultation observations, Triton's subsolar point has moved in latitude from -48° to -49°). The motion of Triton's subsolar point is most extreme during a major season. Figure 8.1 shows the motion of the subsolar point (Trafton 1984) from the year 1900 to 2100.

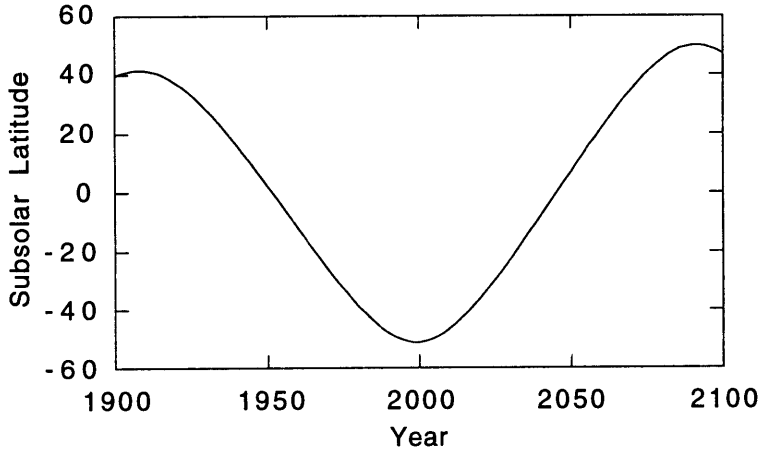

Figure 8.1 The motion of the subsolar point on Triton. Currently Triton is in the middle of a "major" summer. Within 100 years of the current time, the subsolar point on Triton will be at its furthest north and Triton will be in a "major" winter.

The atmospheric pressure on Triton has been predicted to change due to the changing illumination and the surface frost coverage. The extent of the seasonal variation is not well constrained. Some models predict a ten-fold decrease in surface pressure during the 1990's (Spencer 1990), while others (Hansen and Paige 1992; Spencer and Moore 1992) predict a ten-fold or more change in pressure over a seasonal cycle. Although the atmospheric change over a season is periodic, over the short time span (relative to the seasonal cycle) of six years, the atmospheric change would be approximately linear.

Figure 8.2 shows the surface pressure measured at three times (the Voyager encounter in 1989 and the stellar occultations in 1993 and 1995). If the difference between the pressure in the model and the occultation data were due to seasonal change, we would expect the measurements to fall on a line. A clear linear relationship is not evident.

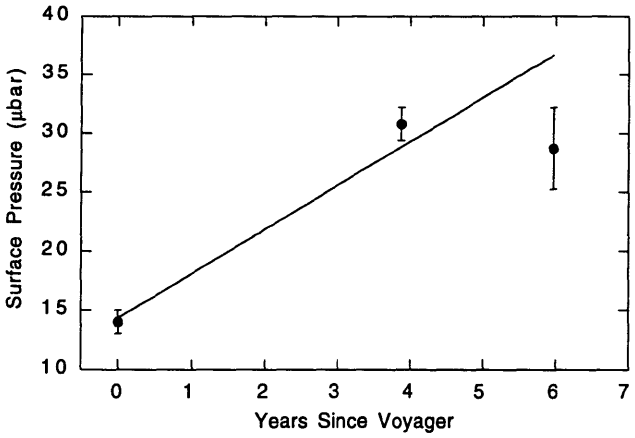

Figure 8.2 Surface pressure as a function of time. The surface pressure as determined by an isothermal model fit to the RSS occultation data (Gurrola 1995) is given at time 0 (1989 Aug. 25). The other two points are the surface pressure determined from the physical model fits to the Tr60 and Tr148 occultation with a mean molecular weight of 28. The line is a linear trend weighted by the formal errors.

The next explanation we consider for the increased pressure relative to the model is an underestimate of the surface radius. While the RSS occultation observation determined the surface pressure, it did not define the surface radius very precisely and analysis of the RSS data in conjunction with the UVS occultation data has yielded conflicting values for the surface radius (Gurrola *et al.* 1992). The nominal Voyager model assumes a surface radius of 1352 km while the best-fitting S96 model reaches a pressure of 14 μbars at a radius of 1363 km. If the surface radius were increased by 11 km, the nominal Voyager model and our stellar occultation data would agree. Is this within the uncertainty of the surface radius determination?

The surface radius of Triton was determined several different ways (different datasets and different methods). From limb measurements of Voyager imaging data, the surface radius was determined to be 1350 ± 5 km (Smith *et al.* 1989). Davies *et al.* (1991) established a surface radius of 1352.6 ± 2.4 km based on imaging data. Finally, Gurrola *et al.* (1992) reported that the chord length of the RSS occultation gives a radius of 1359.6 km with an uncertainty of 0.6Δ, where Δ is the cross-track uncertainty of the spacecraft. Coupling this with the UVS solar occultation gives 1351 ± 6 km and with the UVS stellar occultation gives 1342 ± 8 km. From these different determinations, we see there is some uncertainty in the surface radius of Triton. But most solutions would not be consistent with a radius of 1363 km. An underestimate of Triton's surface radius may not be the sole explanation for the pressure difference, although it could be part of the answer.

The last explanation for the larger surface pressure is that the atmospheric model does not correctly describe Triton's atmosphere in the microbar region. The model is based on UVS solar occultation data, which probed much higher altitudes (500 km altitude), and the RSS measurements of the surface pressure. The lower boundary conditions are set to be the temperature at the tropopause and the surface pressure. The

behavior in between these two regions is determined by heat conduction down from the ionosphere and radiative transfer by CO and HCN. If this model does not accurately describe the atmospheric physics from the surface to the region that the occultation is probing, then our derived surface pressure would be incorrect. We see evidence that the model is not correct when looking at the temperature profile in the 50-100 km altitude range. The strong thermal gradient predicted by models (Krasnopolsky *et al.* 1993; Strobel and Summers 1995; Strobel *et al.* 1996) is not present in our highest SNR data and the lower SNR light curves are inconclusive on the thermal gradient. We shall discuss the thermal structure of Triton's atmosphere in the next section.

8.2 Triton's Thermal Structure near 1400 km radius

From our three different analysis methods, the temperature structure of our highest SNR occultation light curve (IRTF-PCCD) is isothermal. This was demonstrated in Chapter 5 when we fit for a power-law model of the temperature profile and found a power-law index that was consistent with zero. We must ask the question: Does the uncertainty in the power-law index allow for the temperature gradient of Strobel *et al.*? To answer this, we constructed a synthetic light curve from the Strobel *et al* model and fit the same power-law thermal gradient model. We used the S96 model with a surface pressure of 29 μbars with the nominal molecular weight and simulated IRTF PCCD data (impact parameter, integration time, velocity and SNR). The least-squares fit gives a power-law index of 11.5 ± 2.1. If the gradient were in the occultation data, we should be able to see it. However, when we fit for the power-law index in the actual IRTF-PCCD light curve (Chapter 5), we get $b=1.3 \pm 1.3$, indicating that the gradient of the physical model is not in the occultation data.

This is consistent with the numerical inversion results that showed an isothermal temperature profile for this same dataset. The temperature profiles from the numerical inversion of the other occultation light curves are consistent with either an isothermal model or the temperature gradient of nominal Voyager model.

Finally, we have shown that the Strobel *et al.* model does not match the IRTF-PCCD data near the central flash. We propose that this is due to the thermal gradient. To demonstrate this, we fit the IRTF-PCCD data with a power-law thermal gradient model with the power-law index set to 11.5 to mimic the thermal gradient of the Strobel *et al.* model. We could not get a good fit to the central-flash flux using this model which only differs from the isothermal model that fit the data by the power-law thermal gradient. The same central-flash flux mismatch was evident. From this, we conclude that

the IRTF-PCCD data is not matched by the physical model because of the thermal gradient.

The thermal gradient in the nominal Voyager model is mainly due to heat conducted down from about 400 km altitude. The model thermal gradient could be less if: (i) the amount of heat into Triton's upper thermosphere has decreased since the Voyager observations, (ii) the heat is being input at a higher altitude, or (iii) the concentration of radiatively important species are different than modeled. Besides changing the radiative-thermal conduction model, the temperature structure in the microbar region could be different than modeled if there was more vigorous convection near the surface extending the altitude of the tropopause.

In summary, all three analysis methods show that the highest SNR Triton occultation data are consistent with an isothermal temperature structure and not the thermal gradient predicted by atmospheric models.

8.3 Composition

In the physical model fits for molecular weight, we consistently found a molecular weight larger than that of molecular nitrogen. However, stellar occultations are sensitive to the scale height which is a combination of the temperature, temperature gradient and mean molecular weight (Eq. 5.11). The difference between the fitted molecular weight and a pure N_2 atmosphere could be due to a problem with the temperature or temperature gradient of the model. This is likely since we have shown that the data do not agree with the temperature gradient of the model. However, we cannot strictly say that the greater molecular weight is not real, so we will consider the implications.

From spectroscopic observations of surface ices (Cruikshank *et al.* 1993), we infer Triton's atmosphere is mainly composed of N_2 [CO_2 ice was detected, but its vapor pressure at 38 K is negligible (Brown and Ziegler 1980)]. Those observations would not have detected noble gases, so we will consider the possibility that the addition component is a noble gas. Of the noble gases heavier than N_2, we would expect argon (mean molecular weight = 39.9) to be the most abundant. The UVS spectra from Voyager showed no signature of argon (Broadfoot *et al.* 1989), however, those observations may not place a strict limit on the amount of argon in the lower atmosphere (D. Strobel, personal communication).

The change in refractivity at STP of the atmospheric gas from pure N_2 was not included in the least-squares fit. The refractivity at STP of Ar is about 5% less than the refractivity at STP of N_2 (Peck and Fisher 1964; Peck and Khanna 1966). If there were

about 9% argon by mass in the atmosphere, the refractivity at STP would only change by about 0.5%. This would not make an appreciable difference in the results.

These measurements are consistent with a mass fraction of argon equal to 8.7 ± 4.7%. At 38 K, the vapor pressure of argon is 3% of the vapor pressure of N_2 (Brown and Ziegler 1980). Therefore, to get such a large vapor pressure of argon, there would have to be almost three times as much argon ice as N_2 ice on the surface of Triton. The vapor pressure of heavier noble gases like Xe and Kr are smaller than Ar by a factor of more than 1000 at 38 K (Brown and Ziegler 1980).

8.4 Asymmetry

In Chapter 5, we established that the scale height of Triton's atmosphere in the microbar region was different between the immersion and emersion limbs probed by the IRTF light curves. Did the Voyager 2 spacecraft data show any asymmetry? With UV occultation observations, the starlight is dimmed mainly due to extinction (absorption and scattering) rather than refraction. The occultation is observed as a time series of spectra with different molecules causing extinction in different channels. Absorption of the transmitted solar spectrum below 800 Å, attributed to N_2 around 500 km altitude, showed no asymmetry (Broadfoot *et al.* 1989). The occultation probed the winter and summer hemispheres on ingress and egress.

However, the occultation signature due to extinction by methane at radii similar to those probed by these occultations (40 km altitude) shows a factor of 10 difference in the methane concentration from ingress to egress. As discussed above, the observed asymmetry from these stellar occultation data could be due to a difference in temperature, temperature gradient or mean molecular weight. But a factor of 10 difference in the methane concentration would not change the mean molecular weight of the atmosphere sufficiently to account for this asymmetry since the nominal concentration is so small; however, it does imply that the atmosphere is not homogeneous.

What could cause the asymmetry? First, we will consider the possibility that the asymmetry is tied to Triton's diurnal cycle. The immersion and emersion chords are probing the sunrise and sunset limbs. If the atmosphere is cooling radiatively during Triton's night we might expect the atmosphere above the sunrise limb to be cooler than that above the sunset limb. The radiative-time constant of the atmosphere is the ratio of the thermal capacity of the atmosphere above a pressure level p, to the radiated power per unit area, Q.

$$\tau_{\text{rad}} = \frac{c_p pH}{R}\frac{1}{Q} = \frac{7pH}{2}\frac{1}{Q} \tag{8.1}$$

CO provides the most cooling in Triton's atmosphere (X. Zhu, personal communication); therefore, we shall consider only radiation from this molecule. The integrated cooling rate depends on the amount of CO in the atmosphere and the temperature. Estimates of the CO cooling rate in Triton's atmosphere vary from 1.6×10^{-4} to 1.5×10^{-3} erg cm^{-2} s^{-1}, depending on the assumed mixing ratio (Krasnopolsky *et al.* 1993, X. Zhu, personal communication). Taking the largest of these, to determine the shortest τ_{rad}, we get a radiative-time constant on the order of 150 years–much longer than the rotational period of Triton (5.877 days). The temperature of Triton's atmosphere at the microbar level is not varying diurnally through radiative transfer. Another indication that the asymmetry is not tied to the local time on Triton is that we do not see asymmetry in all the occultation light curves.

Next, we investigate whether the scale-height asymmetry could be caused by surface-atmosphere interactions. Unfrosted regions on Triton's surface have a lower albedo; therefore, they reflect less incoming radiation, and have a higher surface temperature. We will look to see if there is any correlation of higher temperatures with unfrosted regions. Figure 8.3 displays the equivalent isothermal temperature as a function of Triton latitude probed at the half-light level.

The latitude and longitude probed by an occultation light curve at a particular time are the coordinates of Triton's limb where the starlight (observed at that time) made its closest pass to Triton (recall that the occultation is probing a line of sight through the atmosphere). The closest approach point of the ray to Triton causes the most refraction in the starlight because that is where the atmosphere is densest.

The temperatures derived from the Tr148A occultation chords (the furthest south probing chords) agree to within about one sigma, especially the highest SNR chords (Lick and KAO). The asymmetry is evident in the IRTF chords.

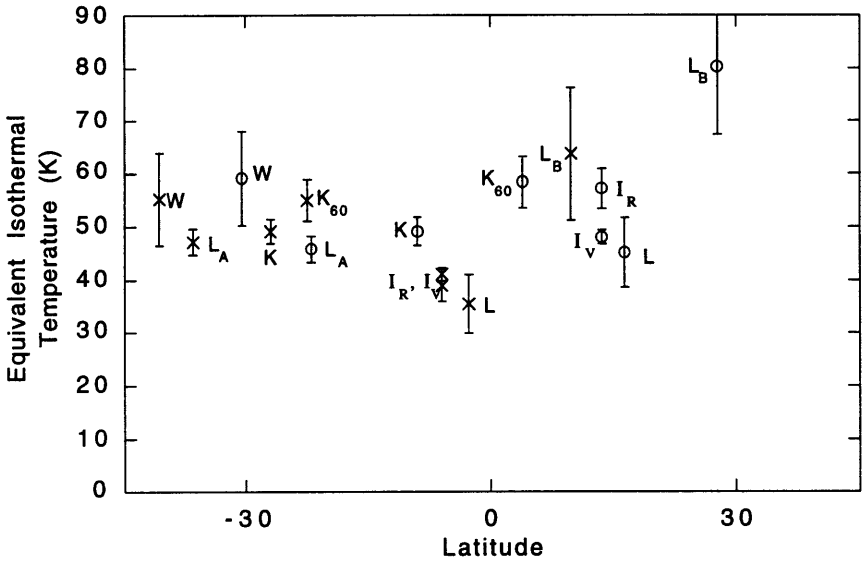

Figure 8.3 Temperature variation with latitude on Triton. The equivalent isothermal temperatures at both immersion and emersion ("x" and "o") are displayed at the latitude probed at half light. The observing stations are indicated: K_{60}=KAO Tr60, I_R=IRTF-NSFCAM, I_V=IRTF-PCCD, K=KAO, L=Lowell, L_A=Lick Tr148A, L_B=Lick Tr148B, W=WIRO. The immersion occultation light curves from the IRTF and Lowell have a colder equivalent isothermal temperature than the others.

Figure 8.4 shows the locations probed at half light by the near limb on a map of Triton's surface (Stansberry *et al.* 1992), where dark correspond to unfrosted patches on the surface and white is ice covered. The Stansberry *et al.* (1992) model assumes regions of the surface are unfrosted if they have an albedo less than a cutoff value ($\lambda_c = 0.75$ for this map) and the equilibrium temperature (given by the albedo) is greater than the frost temperature. This figure shows the relative locations that each light curve probed, but does not show the locus of points probed by each light curve with time (that is illustrated in the next figure).

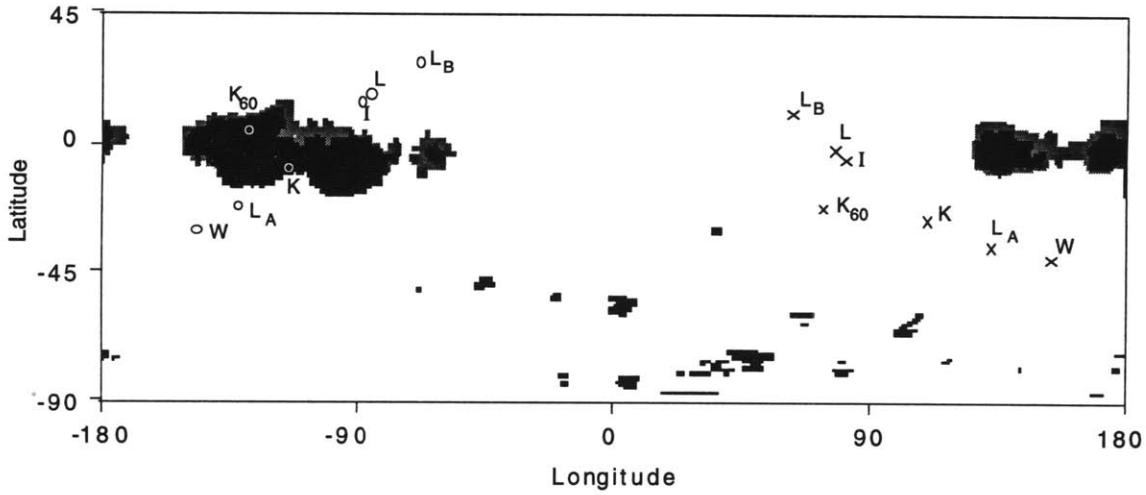

Figure 8.4 Triton latitude and longitude probed at half-light. The dark regions represent unfrosted regions on Triton's surface, while the white represents frost [from Stansberry *et al.* (1992)]. The x's and o's indicate the location probed at half-light during immersion and emersion. From north to south, the chords are: Lick (Tr148B), Lowell, IRTF, Tr60, KAO, Lick (Tr148A) and WIRO. The "o" (white spot) near 0° latitude in the unfrosted region is the emersion probe of the Tr60 occultation.

Before half-light and just after half-light the occultation light curves probe different locations (as shown in Figure 8.4). However, around the midtime of the occultation all the occultation light curves probe around the southern and/or northern limb of Triton. A nearly central light curve (such as the IRTF) probes both the northern and southern limb with the near-limb and far-limb images of the star [the star appears at two locations due to refraction].

Figure 8.5 shows the locations probed by the near and far limbs of the IRTF light curves. At the occultation midtime for the IRTF light curve, the flux contribution from the near limb just about equals that from the far limb, see Figure 5.2. For less central occultation light curves, the far-limb flux is not as significant and the occultation probes either the northern or southern hemisphere, but not both. Because all the Tr148A occultation chords had a closest approach south of Triton's center, they all probe the southern hemisphere around the midtime of the occultation.

From these figures (8.3 and 8.4) we see that the IRTF light curves probed above a frost-free region during immersion with the far-limb image. The KAO light curve probed above the same frost free region during emersion with its near-limb image. However, we only see a scale-height asymmetry in the IRTF data, not in the KAO data. Also, when

the IRTF light curves are weighted to probe the same radii as the KAO data, the asymmetry is still present. From this, we conclude that the scale-height asymmetry is not related to unfrosted surface regions.

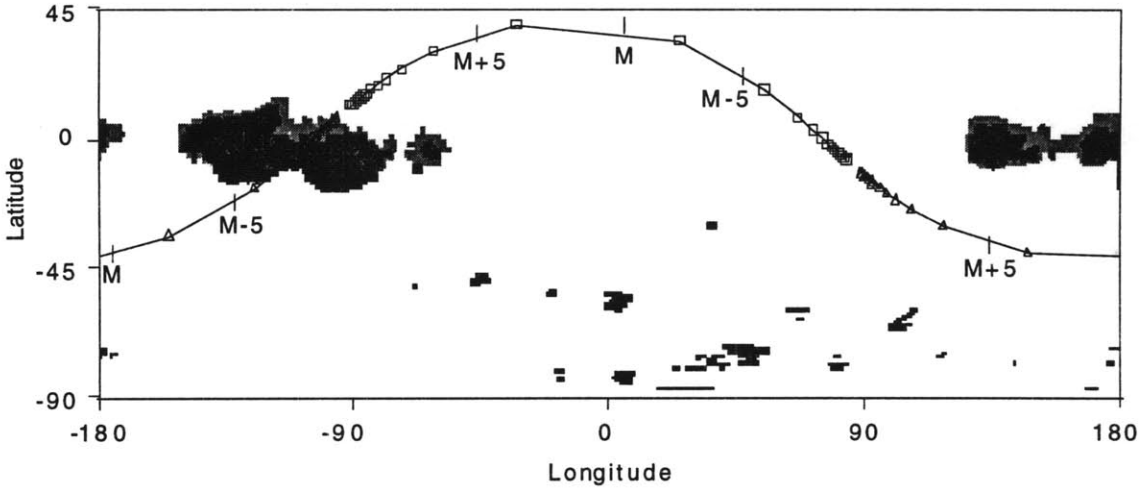

Figure 8.5 Locations on Triton probed by the IRTF light curves. The squares represent the location probed by the near-limb image in the IRTF light curve at an interval of 5 seconds. The triangles represent the location probed by the far-limb image also at 5 second intervals. The location probed by the near-limb and far-limb at the midtime of the event (labeled "M") and 5 seconds before and after the midtime are indicated. During this time (within 5 seconds of the event midtime) the asymmetry is most significant. The dark regions represent unfrosted regions on Triton's surface, while the white represents frost [from Stansberry *et al.* (1992)]. The near- and far-limb paths trace out the terminator of Triton. Near the central-flash, when the asymmetry is most obvious, the starlight is probing a large swath of Triton's terminator and this swath covers a range of longitudes, but nearly the same latitude.

The scale-height asymmetry is most evident in the IRTF light curves. It is also possibly present in the other Tr148B occultation light curves, since the difference in the immersion and emersion scale heights is about one standard deviation (see Table 5.4). And it is not evident in the Tr148A occultation light curves. None of the Tr148A occultation light curves probed the northern hemisphere, while all of the Tr148B light curves did. This leads us to postulate that the scale-height asymmetry is in the northern hemisphere.

The cause of the observed scale-height asymmetry is neither interactions of the atmosphere with the unfrosted regions nor diurnal cooling. From the locations probed by the stellar occultation, we expect that the source of the asymmetry is in the northern hemisphere. Finding the driving mechanism will require new ideas in the modeling of Triton's atmosphere and is beyond the scope of this work.

8.5 Extinction in Triton's Atmosphere

The Voyager observations detected two types of hazes: (i) a ubiquitous thin haze that extended up to 30 km altitude, and (ii) a denser condensation cloud below 10 km altitude (Pollack *et al.* 1990). None of these occultation chords likely probed within 10 km of Triton's surface, but two of the highest SNR light curves may have probed below 30 km altitude (for a surface radius of 1352 km) depending on the atmospheric structure. From either the isothermal model fit or the physical model fit, the IRTF-PCCD light curve probed below 30 km altitude. The minimum radius probed by this light curve corresponds to 17 km altitude for the isothermal model fit and 24 km for the S96 model fit. For the KAO-Tr148A light curve, the minimum radius probed corresponds to 26 km altitude for the isothermal model fit and 30 km for the S96 model fit.

While the Voyager observations showed the thinner haze to be widespread, it did not always extend to 30 km altitude, nor was it present in all locations (Pollack *et al.* 1990). From the Voyager observations, we do not necessarily expect to see extinction in our occultation light curves and we would be surprised to see it in the occultation chords that did not probe below 30 km altitude. And we do not see any evidence for haze in any of the occultation light curves.

One indicator of extinction is a reduced flux level relative to a clear-atmosphere model. We found in Chapter 5 that the background levels for the Lick light curves (Tr148A and Tr148B) from post-event photometry were consistent with that derived from isothermal model fit to within ~1% (and approximately one standard deviation). From this agreement, we conclude that extinction is not significant in that occultation light curve. This light curve probed to a minimum radius of 1400 km, so we would not expect to see extinction based on the Voyager observations.

Next, we will address the deepest probing light curve–the IRTF. There are three arguments indicating that the IRTF-PCCD light curve is not being dimmed by haze. The first indication of a clear atmosphere (besides the general shape of the light curve–no "knee" as in the Pluto occultation light curve), was presented in Chapter 5. The isothermal model fits of the IRTF-PCCD light curve for the impact parameter gave a value consistent with the solution from the light curve timings (Chapter 4). The central-flash flux is proportional to H/ρ (Elliot *et al.* 1977); therefore, an unmodeled haze would appear as either a larger fitted impact parameter or a smaller scale height. The question remains whether unmodeled extinction in the lower altitudes is affecting the fitted scale height. We compare the scale heights from the best fitting two-limb isothermal fits of the IRTF-PCCD and Lick-Tr148A light curves (from Chapter 5, Tables 5.1 and 5.7). The

scale heights are 19.2 ± 0.8 km and 20.4 ± 1.4 km. We choose the Lick data for comparison, since we have already established that it is sampling a clear atmosphere. If there were extinction in the IRTF light curve, it would be manifested by a smaller scale height (or larger impact parameter). The scale height for the IRTF light curve is not significantly smaller than the "clear" atmosphere scale height from the Lick data. The difference is 1.2 ± 1.6 km–consistent with no extinction.

The second argument for a clear atmosphere (in the region probed by the IRTF-PCCD light curve) comes from the physical model fit results. The physical model does not match the occultation light curve data, but this mismatch is not consistent with extinction in Triton's atmosphere, as extinction would cause a decrease of the observed flux.

The final (third) indication that there is no extinction in the region probed by the IRTF-PCCD light curve is related to the observed asymmetry. We will show that neither Mie theory or Rayleigh scattering are consistent with the larger asymmetry in the IR than visible. Extinction efficiency depends on the particle size, so we will digress to discuss estimates of haze particle sizes from Voyager.

Haze has been observed both in imaging data and UVS solar occultation data from Voyager. From these data, the size of the particles has been estimated. Krasnopolsky *et al.* (1992) and Rages and Pollack (1992) both derived particle radii in the range of 0.1–0.2 μm although they used different data in their analysis. However, Herbert and Sandel (1991) derived a very different particle size (0.03 μm) from UV extinction. See Yelle *et al.* (1995) for a discussion of these different results.

We need Mie theory if the particle sizes are 0.1–0.2 μm, and Rayleigh scattering if they are 0.03 μm. First, we will address Rayleigh scattering. If the asymmetry were due to a small particle haze (in comparison to the wavelength), we would expect it to be more efficient in the visible than the IR since Rayleigh scattering is proportional to $1/\lambda^4$. However, the asymmetry is stronger in the IR than in the visible, supporting the hypothesis that there is no small-particle haze.

If the particle's size were closer to the wavelength, we would be in the Mie scattering regime. Mie scattering theory (van de Hulst 1981) is a formal solution to Maxwell's equations that describes the scattering and absorption of light due to arbitrary-sized spherical particles as a function of the refractive index. Figure 8.6 shows the extinction efficiency given by Mie theory at two different wavelengths (0.68 μm and 2.2 μm) as a function of particle radius for a given refractive index. This size parameter (the

ratio of the circumference of the sphere to the wavelength) and the refractive index are independent variables in Mie theory.

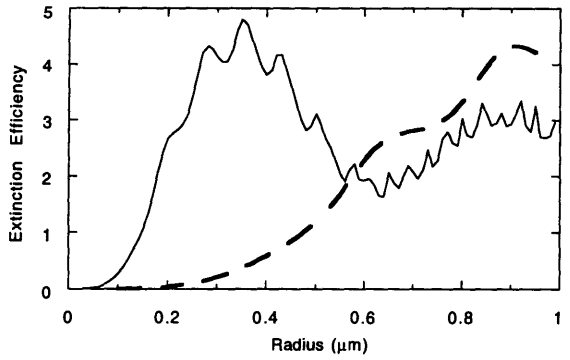

Figure 8.6 The scattering efficiency for two different wavelengths from Mie theory. The solid line is the efficiency for a wavelength of 0.68 μm, while the dashed line corresponds to 2.2 μm. The index of refraction was assumed to be $1.66 - 10^{-4}i$ (olivine). The scattering in the visible is larger than the scattering in the IR for particle sizes less than 0.6 μm.

Although in Figure 8.6 we assumed an index of refraction, we have calculated the scattering efficiency for values of the index of refraction ranging from 1.1 to $2.70 - 1.4\,i$, and found the same behavior. The scattering in the visible is larger than the scattering in the IR for particles with radii below 0.3 μm even for the most extreme value of the index of refraction used ($2.70 - 1.4\,i$ which corresponds to graphite). If the asymmetry were due to extinction, we would see a more extreme asymmetry in the visible than the IR for particles with radii less than 0.3 μm.

8.6 Turbulence and Waves in Triton's atmosphere

In the occultation light curves of the atmosphere of Mars and the giant planets, we see sporadic, short changes in the observed flux (called spikes). These spikes are a result of local density variations. The cause of the density variation has been suggested to be either atmospheric waves (Elliot *et al.* 1977) or turbulence (Hubbard *et al.* 1978; Hubbard 1979).

In the Triton light curves (see Figure 2.9), there are no spikes. This leads to the following questions: Are the density variations not present in Triton's atmosphere? Are we not sampling the atmosphere with fine enough resolution to see them? Do we have high enough SNR data to discern them?

If the projected diameter of the star (at the distance of Triton) is much larger than the Fresnel zone, then we may not be sampling at a high enough resolution. However, for these occultations we shall show the Fresnel zone ($\sqrt{\lambda D} \approx 2$ km) is less than or equal to the projected stellar diameter.

To estimate the projected stellar diameter, we need to know the spectral type of the star. This is derived from the V-K colors of Tr148A and Tr148B. We have the V and K magnitudes of the blended object (Tr148A-Tr148B), and the ratio of the intensities.

We assume the intensity ratio measured by the unfiltered SNAPSHOT system is similar to the intensity ratio through a V filter which has a center wavelength of 0.55 μm and a FWHM of 0.089 μm (unfiltered CCD magnitudes are typically close to an R magnitude, center wavelength of 0.7 μm and a FWHM of 0.2 μm). We also assume the intensity ratio measured through a K' filter (2.12 μm and a FWHM of 0.34 μm) is similar to the intensity ratio at K (2.21 μm and a FWHM of 0.39 μm). Table 8.2 gives derived individual magnitudes of Tr148A and Tr148B at V and K. The V–K colors of the stars are 2.0 ± 0.3 for Tr148A and 1.8 ± 0.4 for Tr148B. The V–K color of a K0 star is 2.0 (Allen 1973); therefore, these stars are approximately K0.

Table 8.2 Individual Magnitudes of Tr148A and Tr148B at V and K

Filter	Magnitude Tr148AB	Intensity Ratio	Magnitude Tr148A	Magnitude Tr148B
V	12.96 ± 0.03[a]	3.78 ± 0.15	13.22 ± 0.03	14.66 ± 0.05
K	10.98 ± 0.11	4.57 ± 0.48	11.20 ± 0.11	12.85 ± 0.14

[a] B. Argyle, personal communication

The absolute magnitude (the magnitude if the star were at a distance of 10 parsec) of a K0 star is +5.9 (Allen 1973). From the apparent magnitudes and the absolute magnitudes of the stars, we determine their distances to be 290 and 564 parsecs for Tr148A and Tr148B. Also from the absolute magnitude, we estimate the radius to be 0.88 times the radius of our Sun (Allen 1973). From the radius and distance, we determine the angular size of the stars as seen from Earth (28 and 15 μarcsec). The projected stellar diameters are the distances these angles subtend at the distance of Triton from Earth (29.3 AU). These are 0.6 km and 0.3 km–less than the Fresnel zone. The sampling beam of the star (the projected stellar diameter) is not so large as to be masking density variations (spikes).

The intensity ratio in the near IR was derived from a low SNR (1.2) occultation light curve. Given that the half-light radius and energy ratio were fixed to solve for the background level in the Tr148B occultation light curve recorded at Lick Observatory in the near IR, the formal error in the near IR intensity ratio is likely underestimated. Given that we consider if these stars are at the same distance. Even, if the near-IR photometry was inaccurate, then the stellar diameter of Tr148A, given above, would have to be too small by more than a factor of three to make the stellar diameter greater than the Fresnel

scale. Similarly the Tr148B diameter could be off by a factor of six and still be less than the Fresnel scale.

Next, we consider whether the integration time could be masking density variations. At altitudes above which refraction of the starlight is significant, we are sampling the planet radius at an interval of 3.5 km to 25 km depending on the dataset (this interval is the product of the integration time and the shadow velocity). As the starlight penetrates deeper in the atmosphere, the same interval in the shadow plane corresponds to increasingly smaller intervals in the planet plane; see Figure 8.7. In the deepest parts of the light curve, we would be sampling intervals in radius of less than one km if the star were a point source. The sampling interval is eventually limited by the apparent diameter of the star (0.3 km or 0.6 km). The finite extent of the integration is not masking any spikes.

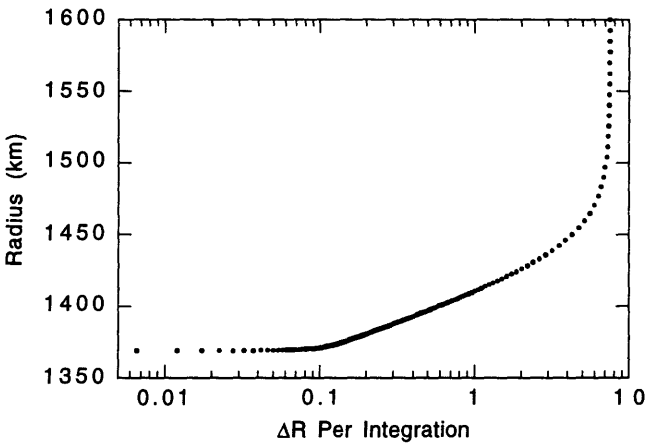

Figure 8.7 The increment in radius probed during the occultation for the IRTF-PCCD light curve. As the starlight probes deeper, the same integration time corresponds to an ever decreasing radius at the planet. By the half-light radius (1444 km), the integration interval is covering less than 5 km. We cannot sample an interval smaller than the stellar diameter (0.3 km).

Not only is there a length scale that characterizes the turbulence we can observe, there is also a minimum size for the density variation to create a spike that would appear larger than the noise. French and Lovelace (1983) derive an equation to determine the RMS refractivity variation given the Fresnel scale, scale height, and the turbulence strength. From French and Lovelace's numerical simulations of the effect of turbulence on an occultation light curve, turbulence with a strength (*i.e.*, an RMS phase shift of a plane wave produced by passage through the atmosphere) of 1.0 should be visible in these Triton occultation light curves, if it is present. This turbulence strength along with the Fresnel scale and scale height of Triton's atmosphere translates to an RMS variation in the refractivity of 0.1%.

We can place limits on the turbulence in Triton's atmosphere from the lack of spikes in these occultation data. At the locations probed, there was no atmospheric

turbulence in the microbar pressure levels with an RMS variation greater than 0.1% and a scale greater than 4 km.

9. Conclusions

9.1 Scientific Results

There are seven new results about Triton's atmosphere presented in this thesis.

1. We have probed the microbar pressure level on Triton in 1993 and 1995 and found the atmospheric pressure to be consistent from these two datasets. There is no detectable seasonal change in Triton's atmosphere. The 3σ change in pressure at 1400 km radius is between –0.9 and +0.7 μbar/year from the isothermal fits. Using the S96 model to relate conditions at the microbar pressure level to the surface, we can place limits on the surface pressure change. The 3σ change in surface pressure is between +4.4 and –6.3 μbar/year.

2. Using three different analysis methods to retrieve atmospheric pressure from occultation light curves, we consistently find the pressure at 1400 km to be larger than the nominal Voyager model at the same radius. This pressure difference is probably the result of the atmospheric structure being mismodeled in the microbar pressure levels where the Voyager 2 instruments did not probe and/or an underestimate of Triton's surface radius. Another explanation (seasonal change in atmospheric pressure) is unlikely because of the non-detection of a pressure change between the 1993 and 1995 observations.

3. In the highest SNR occultation light curve (IRTF-PCCD), we find no evidence for the strong thermal gradient predicted by atmospheric models (Krasnopolsky *et al.* 1993; Strobel *et al.* 1996). The IRTF-PCCD data place a limit on the thermal gradient in the microbar region to be 0.4 ± 0.4 K/km. The other occultation light curves are consistent with either an isothermal model or the nominal Voyager model. Some potential explanations of the observed thermal structure are: (i) the amount of heat into Triton's upper thermosphere has decreased since the Voyager observations, (ii) the heat is input at a higher altitude than modeled, (iii) the concentration of radiatively important species is different than modeled, or (iv) there is more vigorous convection near the surface extending the altitude of the tropopause.

4. We find an atmospheric scale height which is less than the nominal Voyager model from physical model fits for the mean molecular weight of the atmosphere. The

indication of a heavier constituent is likely the result of an incorrectly modeled temperature or temperature gradient.

5. From the consistency in the zero-flux level determined from post-event photometry and isothermal model fitting, we have determined that there is no evidence of extinction in three occultation light curves (two from the 0.9-m telescope at Lick and the light curve from the IRTF-NSFCAM). Three different analyses supported the idea that the IRTF-PCCD light curve was not affected by extinction from haze in Triton's atmosphere. The lack of extinction in these occultation light curves is consistent with Voyager observations (Pollack *et al.* 1990).

6. We have identified asymmetry in occultation light curves recorded at the IRTF and potential asymmetry from the other occultation light curves that probed the northern hemisphere of Triton. The asymmetry could be caused by a change in temperature, temperature gradient or molecular weight. This change is consistent with a lower temperature at immersion relative to emersion of 7 K.

7. From the absence of spikes in the occultation light curves, we conclude there is no turbulence with an RMS density variation greater than 0.1% and a scale greater than 4 km in the microbar pressure level of Triton's atmosphere.

9.2 Technical Advancements

In this section, we summarize the technical developments that were used in this work. The most significant technical advancement has been the improvements to our occultation prediction methods. The ability to predict the shadow path of small-body occultations is essential to these (and future) observations. We have consistently shown that we can predict the shadow path for bodies with an angular radius of 0.06 arcsec (Triton and Pluto) in time to locate the KAO in the shadow path.

We have also expanded our analysis methods for this work. In particular, we have applied a new method for fitting a general physical model to these occultation data, implemented a numerical inversion method applicable to small-body occultation data and expanded existing atmospheric models to include the far-limb flux contribution.

There is certain ancillary information that must be known to analyze occultation data (*i.e.* the impact parameter and zero-flux level). In Chapter 3, we developed a method for determining the closest approach distance between a star and a solar-system body passing nearby (the ephemeris method). Applying this method to the Tr60 occultation,

we determined the impact parameter to six milliarcsec and demonstrated how future observations could be planned to decrease that error. The impact parameter derived from the ephemeris method was consistent with the value derived from model fitting and the closest approach time predicted by the method agreed with the observed midtime of the occultation. Appendix IV expands on the ephemeris method for the special case of linear sky-plane motion (the *compromise* method).

We have demonstrated that model fitting of the central-flash flux can yield an impact parameter more accurate than the traditional multiple-chord method. One can fit for the impact parameter if the occultation light curve exhibits a central-flash and no extinction. For the Tr148B occultation, this method resulted in an impact parameter that agreed with the result from the occultation timings and had an error about 3 times smaller (8 km vs. 25 km).

We have also demonstrated that the zero-flux level of an occultation light curve can be determined using isothermal-model fitting when the pre- or post-event photometry is inaccurate (due to a CTE problem, vignetting or mismodeled scattered light).

Finally, we used numerical PSF model fitting to derive occultation light curves. This photometric method results in higher SNR occultation light curves than simple aperture photometry. Future occultation observers should strive to simultaneously record a reference point-source during the occultation.

9.3 Future Work

As usual, new observational results provide fodder for theorists. This work is no exception. Advances in modeling Triton's atmosphere are needed to reconcile these observations with current models. Possible ways to change the thermal gradient in this region are: (i) decrease the amount of heat into Triton's upper thermosphere, (ii) input the heat at a higher altitude, (iii) change the concentration of radiatively important species, or (iv) change the troposphere model to extend to higher altitudes. These ideas need to be examined to see if they can change the thermal structure sufficiently while still matching the Voyager observations.

Other future work is to continue monitoring Triton's atmosphere for seasonal change. For both Triton and Pluto, extreme changes in surface pressure have been predicted due to the varying seasonal insolation and the vapor-pressure control of the atmosphere. The most inexpensive method for detecting this seasonal change is a series of occultation observations. We have begun this for Triton (and one Pluto occultation has

been observed). A continuing program of occultation observations of these two bodies would teach us about the atmosphere and surface ices on these two bodies.

Unfortunately, many opportunities to observe small-body occultation will be lost in the next 5 years due to the shutdown of the Kuiper Airborne Observatory. Occultation observations are different than most astronomical observations. To successfully view the event, the observer must be positioned at a specific location at a set time and the sky must be clear. For small-body occultations, the shadow path may be a only few thousand kilometers wide and large telescopes often are not located in the shadow path. With the KAO, we were able to locate a 0.9-m telescope in the shadow path and fly above the clouds. There are two Triton occultations (McDonald and Elliot 1995) predicted for 1997 (see Appendix II) which could be recorded with much higher SNR than previous occultations (one star is 15 times brighter than Tr148A). But their shadow paths are mostly over the oceans. The KAO will be sorely missed for these occultations.

We look forward to the next generation airborne observatory (SOFIA) which should see first light in 2001. The increase in telescope aperture (2.5 m) will increase our pool of scientifically interesting occultation candidates.

10. References

Acton, C. H., Jr. (1990). The SPICE concept: An approach to providing geometric and other ancillary information needed for interpretation of data returned from space science instruments. AIAA/NASA Second International Symposium on Space Information Systems, JPL (Pasadena, CA), AIAA, 1029-1052.

Allen, C. W. (1973). Astrophysical Quantities. London, Athlone Press.

Baron, R. L., R. G. French and J. L. Elliot (1989). "The oblateness of Uranus at the 1-μbar level." Icarus **78**: 119-130.

Baum, W. A. and A. D. Code (1953). "A photometric observation of the occultation of σ Arietis by Jupiter." Astronomical Journal **58**: 108-112.

Bevington, P. R. and D. K. Robinson (1992). Data Reduction and Error Analysis for the Physical Sciences. New York, McGraw-Hill Inc.

Bosh, A. S. and S. W. McDonald (1992). "Stellar occultation candidates from the Guide Star Catalog. I. Saturn, 1991-1999." Astronomical Journal **103**(3): 983-990.

Bosh, A. S., L. A. Young, J. L. Elliot, H. B. Hammel and R. L. Baron (1992). "Photometric variability of Charon at 2.2 μm." Icarus **95**: 319-324.

Broadfoot, A. L., S. K. Atreya, J. L. Bertaux, J. E. Blamont, A. J. Dessler, *et al.* (1989). "Ultraviolet spectrometer observations of Neptune and Triton." Science **246**: 1459-1466.

Brown, G. N., Jr. and W. T. Ziegler (1980). "Vapor pressure and heats of vaporization and sublimation of liquids and solids of interest in cryogenics below 1-atm pressure." Advances in Cryogenic Engineering **25**: 662-670.

Buie, M. W., R. L. Millis, L. H. Wasserman, J. L. Elliot, S. J. Bus, *et al.* (1993). "CCD Camera Occultation System." Bulletin of the American Astronomical Society **25**(3): 1115.

Buratti, B. J., J. D. Goguen, J. Gibson and J. Mosher (1994). "Historical photometric evidence for volatile migration on Triton." Icarus **110**(2): 303-314.

Bus, S. J., L. H. Wasserman and J. L. Elliot (1994). "Chiron stellar occultation candidates: 1993-1996." Astronomical Journal **107**(5): 1814-1824.

Bus, S. J., M. W. Buie, D. G. Schleicher, W. B. Hubbard, R. L. Marcialis, *et al.* (1996). "Stellar occultation by 2060 Chiron." Icarus: submitted.

Carlson, R. W., J. C. Bhattacharyya, B. A. Smith, T. V. Johnson, B. Hidayat, *et al.* (1973). "An atmosphere on Ganymede from its occultation on SAO 186800 on 7 June 1972." Science **182**: 53-55.

Chamberlain, D. M., S.B. Thesis, Department of Earth, Atmospheric and Planetary Sciences, Massachusetts Institute of Technology, 1996.

Clifford, A. A. (1973). Multivariate Error Analysis. London, Applied Science Publishers, Ltd.

Cruikshank, D. P. and P. M. Silvaggio (1979). "Triton: A satellite with an atmosphere." Astrophysical Journal **233**: 1016-1020.

Cruikshank, D. P., R. H. Brown and R. N. Clark (1984). "Nitrogen on Triton." Icarus **58**: 293-305.

Cruikshank, D. P. and R. H. Brown (1986). Satellites of Uranus and Neptune, and the Pluto-Charon System. Satellites. J. A. Burns and M. S. Matthews, University of Arizona Press: 1026.

Cruikshank, D. P., T. L. Roush, T. C. Owen, T. R. Geballe, C. de Bergh, *et al.* (1993). "Ices on the surface of Triton." Science **261**: 742-745.

Cruikshank, D. P. (1995). Neptune and Triton. Tucson, AZ, University of Arizona Press.

Davies, M. E., P. G. Rogers and T. R. Colvin (1991). "A control network of Triton." Journal of Geophysical Research **96**(E1): 15,675 - 15,681.

deVaucouleurs, G. and D. H. Menzel (1960). "Results of the occultation of Regulus by Venus, July 7, 1959." Nature **188**: 28-33.

Dunham, D. W., J. B. Dunham, R. P. Binzel, D. S. Evans, M. Freuh, *et al.* (1990). "The size and shape of (2) Pallas from the 1983 occultation of 1 Vulpeculae." Astronomical Journal **99**(5): 1636-1662.

Dunham, E. W., R. L. Baron, J. L. Elliot, J. V. Vallerga, J. P. Doty, *et al.* (1985). "A high-speed, dual-CCD imaging photometer." Publications of the Astronomical Society of the Pacific **97**: 1196-1204.

Dunham, E. W., S. W. McDonald and J. L. Elliot (1991). "Pluto-Charon stellar occultation candidates: 1990-1995." Astronomical Journal **102**(4): 1464-1484.

Dunham, E. W., C. H. Ford, R. P. S. Stone, S. W. McDonald, C. B. Olkin, *et al.* (1994). "Occultation predictions using CCD strip-scanning astrometry." Bulletin of the American Astronomical Society **26**(3): 1154.

Dunham, E. W., J. S. McDonald, D. K. Gilmore, J. Holbrook, D. M. Rank, *et al.* (1995). "Lick Observatory observations of the occultation of Tr148 by Triton." Bulletin of the American Astronomical Society **27**(3): 1101.

Elliot, J. L., R. G. French, E. Dunham, P. J. Gierasch, J. Veverka, *et al.* (1977). "Occultation of ε Geminorum by Mars. II. The structure and extinction of the Martian upper atmosphere." Astrophysical Journal **217**: 661-679.

Elliot, J. L., R. G. French, E. Dunham, P. J. Gierasch, J. Veverka, *et al.* (1977). "Occultation of ε Geminorum by Mars: Evidence for atmospheric tides?" Science **195**: 485-486.

Elliot, J. L. (1979). "Stellar occultation studies of the solar system." Annual Review of Astronomy and Astrophysics **17**: 445-475.

Elliot, J. L. and P. D. Nicholson (1984). The rings of Uranus. Planetary Rings. R. Greenburg and A. Brahic. Tucson, University of Arizona Press: 25-72.

Elliot, J. L., E. W. Dunham, A. S. Bosh, S. M. Slivan, L. A. Young, *et al.* (1989). "Pluto's atmosphere." Icarus **77**: 148-170.

Elliot, J. L. and L. A. Young (1991). "Limits on the radius and a possible atmosphere of Charon from its 1980 stellar occultation." Icarus **89**(2): 244-254.

Elliot, J. L. and L. A. Young (1992). "Analysis of stellar occultation data for planetary atmospheres. I. Model fitting, with application to Pluto." Astronomical Journal **103**(3): 991-1015.

Elliot, J. L., A. S. Bosh, M. L. Cooke, R. C. Bless, M. J. Nelson, *et al.* (1993). "An occultation by Saturn's rings on 1991 October 2-3 observed with the Hubble Space Telescope." Astronomical Journal **106**(6): 2544-2572.

Elliot, J. L., E. W. Dunham and C. B. Olkin (1993). "Triton's atmospheric structure from KAO stellar occultation observations." Bulletin of the American Astronomical Society **25**(3): 1106-1107.

Elliot, J. L., C. B. Olkin, E. W. Dunham, C. H. Ford, D. K. Gilmore, *et al.* (1995). "Jet-like features near the nucleus of 2060 Chiron." Nature **373**: 46-49.

Elliot, J. L. and C. B. Olkin (1996). Probing Planetary Atmospheres with Stellar Occultations. Annual Review of Earth and Planetary Sciences. G. W. Wetherill. Palo Alto, Annual Reviews Inc. **24:** (in press).

Foust, J. A., J. L. Elliot, C. B. Olkin, S. W. McDonald, E. W. Dunham, *et al.* (1996). "Determination of the Charon-Pluto mass ratio from center-of-light astrometry." Icarus: submitted.

French, R. G., J. L. Elliot and P. J. Gierasch (1978). "Analysis of stellar occultation data. Effects of photon noise and initial conditions." Icarus **33**: 186-202.

French, R. G. and G. E. Taylor (1981). "Occultation of the ε Geminorum by Mars. IV. Oblateness of the Martian upper atmosphere." Icarus **45**: 577-585.

French, R. G. and R. V. E. Lovelace (1983). "Strong turbulence and atmospheric waves in stellar occultations." Icarus **56**: 122-146.

French, R. G., P. A. Melroy, R. L. Baron, E. W. Dunham, K. J. Meech, *et al.* (1985). "The 1983 June 15 occultation by Neptune. II. The oblateness of Neptune." Astronomical Journal **90**(12): 2624-2638.

French, R. G., J. L. Elliot, L. M. French, J. A. Kangas, K. J. Meech, *et al.* (1988). "Uranian ring orbits from Earth-based and Voyager occultation observations." Icarus **73**: 349-378.

French, R. G., P. D. Nicholson, C. C. Porco and E. A. Marouf (1991). Dynamics and structure of the Uranian rings. Uranus. J. T. Bergstralh, E. D. Miner and M. S. Matthews. Tucson, University of Arizona Press**:** 327-409.

French, R. G., P. D. Nicholson, M. L. Cooke, J. L. Elliot, K. Matthews, *et al.* (1993). "Geometry of the Saturn system from the 3 July 1989 occultation of 28 Sgr and Voyager observations." Icarus **103**(2): 163-214.

Green, R. M. (1985). Spherical Astronomy. Cambridge, Cambridge University Press.

Gurrola, E. M., E. A. Marouf, V. R. Eshleman, G. L. Tyler and P. A. Rosen (1992). Analysis of Voyager radio occultation observations of Triton. Neptune and Triton, Tucson, Arizona, 28.

Gurrola, E. M., "Interpretation of radar data from the icy Galilean satellites and Triton," Ph. D. Thesis, , Stanford University, 1995.

Hansen, C. J. and D. A. Paige (1992). "A thermal model for the seasonal nitrogen cycle on Triton." Icarus **99**(2): 273-288.

Herbert, F. and B. R. Sandel (1991). "CH4 and haze in Triton's lower atmosphere." Journal of Geophysical Research **96**: 19,241-19,252.

Høg, E. and J. von der Heide (1976). "Perth 70 catalog." Abhandlungen der Hamburg Sternwarte **9**.

Hubbard, W. B. and T. C. Van Flandern (1972). "The occultation of Beta Scorpii by Jupiter and Io. III. Astrometry." Astronomical Journal **77**: 65-74.

Hubbard, W. B., J. R. Jokipii and B. A. Wilking (1978). "Stellar occultations by turbulent planetary atmospheres: A wave-optical theory including a finite scale height." Icarus **34**: 374-395.

Hubbard, W. B. (1979). "The ε Geminorum occultation: Evidence for waves or turbulence." Astrophysical Journal **229**: 821-827.

Hubbard, W. B. (1984). Planetary Interiors. New York, van Nostrand Reinhold Co.

Hubbard, W. B., P. D. Nicholson, E. Lellouch, B. Sicardy, A. Brahic, *et al.* (1987). "Oblateness, radius, and mean stratospheric temperature of Neptune from the 1985 August 20 occultation." Icarus **72**: 635-646.

Hubbard, W. B., C. C. Porco, D. M. Hunten, G. H. Rieke, M. J. Rieke, *et al.* (1993). "The occultation of 28 Sgr by Saturn: Saturn pole position and astrometry." Icarus **103**(2): 215-234.

Hubbard, W. B., B. Sicardy, R. Miles, A. J. Hollis, R. W. Forrest, *et al.* (1993). "The occultation of 28 Sgr by Titan." Astronomy and Astrophysics **269**(1/2): 541-563.

Jacobson, R. A., J. E. Riedel and A. H. Taylor (1991). "The orbits of Triton and Nereid from spacecraft and Earthbased observations." Astronomy and Astrophysics **247**: 565-575.

Klemola, A. R. and B. G. Marsden (1977). "Predicted occultations by the rings of Uranus, 1977-1980." Astronomical Journal **82**: 849-851.

Klemola, A. R., D. J. Mink and J. L. Elliot (1981). "Predicted occultations by Uranus: 1981-1984." Astronomical Journal **86**: 138-140.

Klemola, A. R. and D. J. Mink (1991). "Occultations by Uranus and Neptune: 1991-1999." Astronomical Journal **102**: 389-394.

Krasnopolsky, V. A., B. R. Sandel and F. Herbert (1992). "Properties of haze in the atmosphere of Triton." Journal of Geophysical Research **97**: 11695-11700.

Krasnopolsky, V. A., B. R. Sandel, F. Herbert and R. J. Vervack (1993). "Temperature, N_2, and N density profiles of Triton's atmosphere: observations and model." Journal of Geophysical Research **98**: 3065-3078.

Krasnopolsky, V. A. and D. P. Cruikshank (1995). "Photochemistry of Triton's atmosphere and ionosphere." Journal of Geophysical Research **100**: 21271-21286.

Lellouch, E., W. B. Hubbard, B. Sicardy, F. Vilas and P. Bouchet (1986). "Occultation determination of Neptune's oblateness and stratospheric methane mixing ratio." Nature **324**: 227-231.

Mason, E. C., "The Rings of Uranus," B.A. Thesis, , Wellesley College, 1992.

McDonald, S. W. and J. L. Elliot (1992). "Triton stellar occultation candidates: 1992-1994." Astronomical Journal **104**: 862-879.

McDonald, S. W., C. B. Olkin, E. W. Dunham, J. L. Elliot, C. C. Dahn, *et al.* (1993). "Predicting the occultation of Tr60 by Triton." Bulletin of the American Astronomical Society **25**(3): 1107.

McDonald, S. W. and J. L. Elliot (1995). "Triton stellar occultation candidates: 1995-1999." Astronomical Journal **109**: 1352-1362.

Millis, R. L. and J. L. Elliot (1979). Direct determination of asteroid diameters from occultation observations. Asteroids I. T. Gehrels. Tucson, The University of Arizona Press: 98-118.

Millis, R. L. and D. W. Dunham (1989). Precise measurement of asteroid sizes and shapes from occultations. Asteroids II. R. P. Binzel, T. Gehrels and M. S. Matthews. Tucson, The University of Arizona Press: 148-170.

Millis, R. L., L. H. Wasserman, O. G. Franz, R. A. Nye, J. L. Elliot, *et al.* (1993). "Pluto's radius and atmosphere: Results from the entire 9 June 1988 occultation data set." Icarus **105**(2): 282-297.

Mink, D. J. and A. Klemola (1985). "Predicted occultations by Uranus, Neptune, and Pluto: 1985-1990." Astronomical Journal **90**: 1894-1899.

Mink, D. J., A. R. Klemola and M. W. Buie (1991). "Occultations by Pluto and Charon: 1990-1999." Astronomical Journal **101**(6): 2255-2261.

Nicholson, P. D., C. McGhee and R. G. French (1995). "Saturn's central flash from the 3 July 1989 occultation of 28 Sgr." Icarus **113**(1): 57-83.

Olkin, C. B., J. L. Elliot, E. W. Dunham, R. L. Millis, L. H. Wasserman, *et al.* (1993). "Radius scale of Triton's atmosphere from stellar occultation observations." Bulletin of the American Astronomical Society **25**(3): 1106.

Olkin, C. B., J. L. Elliot, E. W. Dunham, C. H. Ford, D. K. Gilmore, *et al.* (1994). On the size of particles near the nucleus of 2060 Chiron. Proceedings of the Airborne Astronomy Symposium on the Galactic Ecosystem: From Gas to Stars to Dust. M. R. Haas, J. A. Davidson and E. F. Erickson. San Francisco, ASP: 333-336.

Olkin, C. B., J. L. Elliot, H. B. Hammel, A. Cooray, J. A. Foust, *et al.* (1995). "Triton stellar occultation observations from the KAO and multi-wavelength observations from the IRTF." Bulletin of the American Astronomical Society **27**(3): 1102.

Olkin, C. B., J. L. Elliot, S. J. Bus, S. W. McDonald and C. C. Dahn (1996). "Astrometry of single-chord occultations: Application to the 1993 Triton event." Publications of the Astronomical Society of the Pacific **108**(720): 202-210.

Peck, E. R. and D. J. Fisher (1964). "Dispersion of argon." Journal of the Optical Society of America **54**: 1362-1364.

Peck, E. R. and B. N. Khanna (1966). "Dispersion of nitrogen." Journal of the Optical Society of America **56**(8): 1059-1063.

Pollack, J. B., J. M. Schwartz and K. Rages (1990). "Scatterers in Triton's atmosphere: Implications for the seasonal volatile cycle." Science **250**: 440-443.

Rages, K. and J. B. Pollack (1992). "Voyager imaging of Triton's clouds and hazes." Icarus **99**: 289-301.

Reitsema, H. J., W. B. Hubbard, R. Hill, R. Marcialis and R. Howell (1995). "WIRO observations of stellar occultation by Triton on 14 August 1995." Bulletin of the American Astronomical Society **27**(3): 1101.

Seidelmann, P. K., Ed. (1992). Explanatory Supplement to the Astronomical Almanac. Mill Valley, CA, University Science Books.

Shure, M., D. W. Toomey, J. T. Rayner, P. M. Onaka and A. T. Denault (1994). NSFCAM: A new infrared array camera for the NASA Infrared Telescope Facility. Instrumentation in Astronomy VIII, Kona, HI, SPIE Proceedings,

Sicardy, B., F. Roques and A. Brahic (1991). "Neptune's rings, 1983-1989: Ground-based stellar occultation observations." Icarus **89**: 220-243.

Smart, W. M. (1977). Textbook on Spherical Astronomy. Cambridge, Cambridge University Press.

Smith, B. A., L. A. Soderblom, D. Banfield, C. Barnet, A. T. Basilevksy, *et al.* (1989). "Voyager 2 at Neptune: Imaging science results." Science **246**: 1422-1449.

Smith, J. D., "Lunar occultation timing in a two-telescope observation of Saturn," B. S. Thesis, Department of Physics, Massachusetts Institute of Technology, 1995.

Spencer, J. R. (1990). "Nitrogen frost migration on Triton: a historical model." Geophysical Research Letters **17**(10): 1769-1772.

Spencer, J. R. and J. M. Moore (1992). "The influence of thermal inertia on temperatures and frost stability on Triton." Icarus **99**(2): 261-272.

Stansberry, J. A., R. V. Yelle, J. I. Lunine and A. S. McEwen (1992). "Triton's surface-atmosphere energy balance." Icarus **99**: 242-260.

Stetson, P. B. (1987). "DAOPHOT: A computer program for crowded-field stellar photometry." Publications of the Astronomical Society of the Pacific **99**: 191 - 222.

Stevens, M. H., D. F. Strobel, M. E. Summers and R. V. Yelle (1992). "On the thermal structure of Triton's thermosphere." Geophysical Research Letters **19**(7): 669-672.

Strobel, D. F. and M. E. Summers (1995). Triton's upper atmosphere and ionosphere. Neptune and Triton. M. S. Matthews. Tucson, University of Arizona Press: 1107-1148.

Strobel, D. F., X. Zhu, M. E. Summers and M. H. Stevens (1996). "On the vertical thermal structure of Pluto's atmosphere." Icarus: (in press).

Taylor, G. E. (1963). "The occultation of Regulus by Venus on 1959 July 7." Royal Observatory Bulletin(No. 72): E355-E366.

Taylor, G. E. (1970). "The occultation of B.D. -17° 4388 by Neptune on 1968 April 7." Monthly Notices of the Royal Astronomical Society **147**: 27-33.

Taylor, G. E., B. O'Leary, T. C. VanFlandern, P. Bartholdi, F. Owen, *et al.* (1971). "Occultation of Beta Scorpii C by Io on May 14, 1971." Nature **234**: 405-406.

Taylor, G. E. (1974). Planetary Occultations: A Review of the Methods of Prediction, the Results of Astrometric Analysis and Future Prospects, Nautical Almanac Office, Royal Greenwich Obs., Hailsham, Sussex, England.

Trafton, L. (1984). "Large seasonal variations on Triton." Icarus **58**: 312-324.

Tryka, K. A., R. H. Brown, V. Anicich, D. P. Cruikshank and T. C. Owen (1993). "Spectroscopic determination of the phase composition and temperature of nitrogen ice on Triton." Science **261**: 751-754.

Tyler, G. L., D. N. Sweetnam, J. D. Anderson, S. E. Borutzki, J. K. Campbell, *et al.* (1989). "Voyager radio science observations of Neptune and Triton." Science **246**: 1466-1473.

van de Hulst, H. C. (1981). Light Scattering by Small Particles. New York, Dover.

Veverka, J., L. H. Wasserman, J. Elliot, C. Sagan and W. Liller (1974). "The occultation of β Scorpii by Jupiter. I. The structure of the Jovian upper atmosphere." Astronomical Journal **79**: 73-84.

Walker, A. R. (1980). "An occultation by Charon." Monthly Notices of the Royal Astronomical Society **192**: 47p-50p.

Walker, P. M. B., Ed. (1988). Chambers Science and Technology Dictionary. Cambridge, Cambridge University Press.

Wasserman, L. H. and J. Veverka (1973). "On the reduction of occultation light curves." Icarus **20**: 322-345.

Wasserman, L. H., R. L. Millis, O. G. Franz, E. Bowell, N. M. White, *et al.* (1979). "The diameter of Pallas from its occultation of SAO 85009." Astronomical Journal **84**: 259-268.

Wasserman, L. H., E. Bowell and R. L. Millis (1981). "Occultations of stars by solar system objects. II. Occultations of catalog stars by asteroids in 1982 and 1983." Astronomical Journal **86**: 1974-1979.

Wasserman, L. H., E. Bowell and R. L. Millis (1987). "Occultations of stars by solar system objects. VII. Occultations of catalog stars by asteroids in 1988 and 1989." Astronomical Journal **94**: 1364-1372.

Wasserman, L. H., E. Bowell and R. L. Millis (1990). "Occultations of stars by solar system objects. VIII. Occultations of catalog stars by asteroids, planets, Titan, and Triton in 1990 and 1991." Astronomical Journal **99**: 723-734.

Wasserman, L. H., M. W. Buie and R. L. Millis (1995). "Observation of the occultation of Tr148 by Triton." Bulletin of the American Astronomical Society **27**(3): 1102.

Yelle, R. V., J. I. Lunine and D. M. Hunten (1991). "Energy balance and plume dynamics in Triton's lower atmosphere." Icarus **89**: 347-358.

Yelle, R. V., J. I. Lunine, J. B. Pollack and R. H. Brown (1995). Lower atmospheric structure and surface-atmosphere interactions on Triton. Neptune and Triton. M. S. Matthews. Tucson, University of Arizona Press: 1031-1105.

Appendix I. Occultation Astrometry: Predictions and Post-Event Results[3]

Stellar occultations potentially provide high precision data for relating solar system ephemerides to the stellar reference frame. For example, occultations by the Uranian rings can define the position of the occulted star relative to the rings to better than 0.02 milliarcsec (equivalent to a few hundred meters at the distance of Uranus). Occultations by atmospheres can be less precise than occultations by symmetrical solid bodies, like rings and large asteroids, with a precision on the order of 1.0 milliarcsec. Planetary astronomers have published the results of about 80 occultation observations, including events involving all known planets (with the exception of Mercury) and more than 40 asteroids. In order to improve the relation between solar system ephemerides and stellar reference frames, an astrometric program is needed to accurately determine the positions and proper motions of previously occulted stars. Since only the brightest stars are currently selected for occultation observations–in order to probe the physical properties of planetary systems–many occultations that involve fainter stars are not observed. However, these events would be useful for improving planetary astrometry in the stellar reference frame. Also, improvement of the ephemerides relative to FK5 would benefit the occultation prediction process, since most of the effort in the prediction refinement involves modeling differences between the observed planet and its ephemeris.

AI.1 Introduction

In order to adequately predict an occultation for deployment of ground-based observers and the Kuiper Airborne Observatory, one needs accurate relative astrometry of the star and occulting body. The accuracies required are a fraction of the angular body radius to ensure that the observer is within the occultation shadow. Small outer solar system bodies like Pluto and Triton (with radii in the range 0.06–0.07 arcsec) require accuracies of 0.02 arcsec. The prediction process has been refined over the years to identify fainter candidates and to achieve these levels of accuracy.

---

[3]This appendix is based on Olkin, C. B. and J. L. Elliot (1994). Occultation astrometry: Predictions and post-event results. Galactic and Solar System Optical Astrometry. L. V. Morrison and G. F. Gilmore. Cambridge, Cambridge University Press: 286-290.

Not only is astrometry important to the prediction of occultations, the resulting occultation timings provide the relative position of the star and occulting body. These data are very accurate (on the order of milliarcseconds to microarcseconds), especially if the star is occulted by a sharp ring feature or gasless limb.

AI.2 Candidate Searches and Predictions

Early occultation predictions were performed by comparing star catalogs against planetary ephemerides (Taylor 1963; Taylor 1970; Taylor 1974). This task has been accelerated with the use of modern computing facilities. Currently, occultations have been predicted for every planet and nearly 200 asteroids using catalogs like the ACRS, GSC and CAMC (Wasserman *et al.* 1990; Bosh and McDonald 1992). This technique of catalog searches is useful for bright planets, because a star of comparable magnitude to the occulting body is needed to provide an adequate signal-to-noise ratio to satisfy most scientific objectives (Elliot 1979).

With the advent of CCD detectors, occultations of fainter bodies–such as Pluto and Triton–could be observed, so that stars fainter than catalog limits could be considered. This was the incentive for some observational searches of occultation candidates. The earliest observational searches were performed by A. Klemola and B. Marsden, who found numerous occultations by the Uranian rings using the Double Astrograph at Lick Observatory (Klemola and Marsden 1977). Klemola and his colleagues have expanded this effort to include Neptune and Pluto (Klemola *et al.* 1981; Mink and Klemola 1985; Klemola and Mink 1991; Mink *et al.* 1991). Searches for occultations by asteroids have been carried out at the Lowell Observatory Astrograph (Wasserman *et al.* 1981; Wasserman *et al.* 1987; Wasserman *et al.* 1990). Recently CCD strip scans have been used for these searches (Dunham *et al.* 1991; McDonald and Elliot 1992) for three reasons: (i) they can record fainter stars than photographic plates for a telescope of the same size, (ii) the raw data are ready for reduction (eliminating the scanning process need for plates), and (iii) CCDs are now more readily available to observers.

Following the identification of a candidate, further astrometry of the star and occulting body is needed to generate occultation predictions for various sites, if the occulting body has a small angular size. Fortunately, only the relative positions are relevant for predicting the path of the occultation shadow.

As an example of how occultations are currently predicted, we shall describe the process used for the 1993 July 10 occultation of Tr60 by Triton. First, a search for Triton occultation candidates was carried out using CCD strips scans from Wallace

Astrophysical Observatory (McDonald and Elliot 1992). In that search, the candidate Tr60 was identified along with 129 other candidates through 1994. CAMC positions confirmed the star's location within 0.15 arcsec in declination, so plans began in earnest to refine the prediction and to observe the occultation. Strip scans containing both objects began two months prior to the occultation at Lick Observatory and Lowell Observatory. Stare frames from the USNO also began at the same time; however, they did not contain both objects until 4 days before the occultation. Having both objects on the same stare frame or strip scan greatly reduces the errors in their relative positions because both the star and occulting body are reduced with the same set of reference stars. All data were sent to MIT by the fastest means possible (FTP or overnight delivery of tapes), where they were reduced relative to a standard network determined with the Lick Double Astrograph.

The positions of Triton relative to its ephemeris were fit to a model that projected its position relative to Tr60 at the occultation time. This model had three components in both right ascension and declination: (i) a constant offset that accounted for RA and Dec errors of Neptune relative to the star, (ii) a linear time variation that absorbed any rotational or scale error of the reference system, and (iii) a term that accounted for an along-track error in Triton's ephemeris about Neptune. The total number of fitted parameters in this model was five. The result of this procedure was a successful prediction (McDonald *et al.* 1993), which allowed several teams of ground-based observers and the KAO to be deployed within Triton's shadow (Olkin *et al.* 1993). However, due to weather and instrument problems, only the KAO observed the occultation (Elliot *et al.* 1993).

AI.3 Post-Event Results

Occultation timings could become a valuable tool for linking the FK5 frame and the solar system frame. Over eighty occultations have been observed using modern detectors and timing methods (see Table 1). Some of these events provide very accurate relative positions between the star and the occulting body. For example, solutions for Uranian ring orbits have given formal errors considerably less than a kilometer in the shadow center (French *et al.* 1991; Mason 1992). This translates to an error of about 0.02 milliarcsec between the star and the center of Uranus. The Saturn ring models are not as precise, but Elliot *et al.* (1993) find uncertainties in the closest approach between the star and Saturn to be 0.5 milliarcsec for the 28 Sgr occultation and 0.6 milliarcsec for the GSC6323–01396 occultation. For objects without sharp edges, such as Pluto's

atmosphere, accurate astrometry is still possible. The uncertainty in the midtime of the atmospheric occultation of P8 by Pluto is 0.046 seconds, which translates to 0.04 milliarcsec at Pluto (Elliot *et al.* 1989; Millis *et al.* 1993).

Table AI.1 Occultations Observed Prior to 1996

Planet or Satellite	Number of Published Occultations	References
Mercury	0	
Venus	1	(deVaucouleurs and Menzel 1960; Taylor 1963)
Mars	1	(Elliot *et al.* 1977; Hubbard 1979; French and Taylor 1981)
Asteroids	>40	(Millis and Elliot 1979; Millis and Dunham 1989)
Jupiter	3	(Baum and Code 1953; Hubbard and Van Flandern 1972; Veverka *et al.* 1974)
Saturn	2	(Elliot *et al.* 1993; French *et al.* 1993; Hubbard *et al.* 1993)
Uranus	20	(Elliot and Nicholson 1984; French *et al.* 1991)
Neptune	8	(French *et al.* 1985; Hubbard *et al.* 1987)
Pluto	1	(Elliot *et al.* 1989; Millis *et al.* 1993)
Io	1	(Taylor *et al.* 1971)
Ganymede	1	(Carlson *et al.* 1973)
Titan	2	(Hubbard *et al.* 1993)
Triton	2	(Elliot *et al.* 1993; Olkin *et al.* 1993; Olkin *et al.* 1995)
Charon	1	(Walker 1980; Elliot and Young 1991)

AI.4 Conclusions

Astrometric networks of faint stars near the outer planets would aid the current methods of occultation prediction. However, even with current techniques, occultations by bodies with an angular size similar to Triton and Pluto can be accurately predicted.

In order to use occultation timings to improve planetary ephemerides, three things need to be accomplished: (i) past and future occultation candidate stars need to be measured accurately in the FK5 system, (ii) the occultation light curves need to be reduced relative to modern ephemerides, and (iii) the results would have to be included in new calculations of planetary ephemerides. Additional astrometric data could be obtained from the many occultations not observed because their signal-to-noise is too low for physical studies, but observations of these events would provide sufficient signal-to-noise for accurate relative astrometry.

Occultation timings could provide improved planetary ephemerides, which would in turn facilitate occultation predictions and improve the tie between solar system ephemerides and the FK5 system.

Appendix II. Occultation Prediction: Case Studies

Since 1992, we have refined the shadow path predictions for seven stellar occultations; see Table AII.1. We will discuss the predictions chronologically to illustrate our prediction methods and their evolution.

Table AII.1 Stellar Occultation Predictions Refined at MIT from 1992-1995

Event	Body	Date	Shadow Path
P17	Pluto	1992 05 21	North of Earth
Tr60	Triton	1993 07 10	South Africa, South America
Ch02	Chiron	1993 11 07	Southwest US
Ch08	Chiron	1994 03 09	South Africa, South America
P20/C20	Pluto	1994 10 03	South of Earth
P20/C20	Charon	1994 10 03	North of Earth
P28	Pluto	1995 07 06	North of Earth
Tr148	Triton	1995 08 14	Hawaii and Western US

AII.1 The P17 Occultation Prediction

When we began these small-body predictions, there were two phases (now we have an intermediate step to improve the prediction many months before an event from transit telescope observations). The first step was the initial candidate identification and the second was the prediction refinement from strip scans. The refinement was most useful just prior to the event (1-2 days) to locate mobile observers (such as the KAO) in the shadow path. The initial candidate search of Dunham *et al.* (1991) determined the star P17 would pass within 0.19 arcsec from Pluto based on five strip scan observations. For reference, the Earth subtends about 0.6 arcsec from Pluto, so an impact parameter larger than 0.3 puts the occultation shadow off the Earth.

We planned observations of this event and begun a prediction refinement in the spring of 1992. Strip scans were recorded at Wallace Observatory and reduced using the candidate search pipeline of Dunham *et al.* (1991) to produce a list of celestial coordinates for all the objects identified on the strip scans. The software pipeline automatically identifies all objects on the CCD strip scans in a given intensity range. The observed star list is compared with an astrometric network, and all observed standard stars are linearly

registered to the astrometric network to determine the conversion from detector coordinates to celestial coordinates.

Due to variations in the starting coordinates of the strip scan and variable seeing, the set of astrometric standard stars used in the registration is not constant across strip scans. The random errors in the astrometric networks will result in a slightly different celestial coordinate system for each strip scan. This effect is minimized if care is taken to always begin the strip scan at the same location. Also, the relative position between two objects is determined much better if both objects are recorded on the same strip scan because they would be reduced with the same set of astrometric standard stars. For that reason, we now record strip scans only when the both objects are on the same strip.

For each observation taken at time, t, a planet residual, ($\Delta\alpha_p(t)$, $\Delta\delta_p(t)$), and star residual, ($\Delta\alpha_*(t)$, $\Delta\delta_*(t)$), are constructed from the difference of the observed occulting body position and its ephemeris and the difference of the observed star position from a reference position; see Eqs AII.1 and AII.2 for the RA equations. Analogous Dec equations exist. The subscripts o, c and e refer to observed, catalog and ephemeris; the subscripts * and p refer to star and planet. The topocentric planet observation are converted to geocentric positions before being subtracted from the ephemeris. Although the star residual should be constant, the residual is indexed by the observation time.

$$\Delta\alpha_*(t) = \alpha_{*o}(t) - \alpha_{*c} \tag{AII.1}$$

$$\Delta\alpha_p(t) = \alpha_{po}(t) - \alpha_{pe}(t) \tag{AII.2}$$

The simplest method to predict the residuals at the occultation time is to assume there is no trend and use the mean value. This is typically not a good assumption for the planet residuals. The occulting body may have a correlated pattern of residuals as it moves through the star field. For example, if the occulting body is a satellite that lags in its orbit, then the residuals will have a cyclic pattern with the period of the orbit. Also, the occulting body's residuals will have a linear trend if there is a simple rotation of the astrometric coordinate system relative to the ephemeris coordinate system (see the Tr60 prediction, Section AII.2, for an example).

For the P17 occultation prediction, we fit for a linear trend to the residuals. Eqs. AII.3 and AII.4 show the model equation where $\bar{t}$ is the mean time of all the observations and the subscript m stands for model.

$$\Delta\alpha_m(t) = a_1 + a_2(t - \bar{t}) \tag{AII.3}$$

$$\Delta\delta_{\rm m}(t) = d_1 + d_2(t - \bar{t}) \qquad \text{(AII.4)}$$

The square of the difference between the model residuals and the observed residuals (planet residual minus star residual) is minimized to solve for the four coefficients (a_1, a_2, d_1, and d_2). The RA and Dec equations are explicitly:

$$\chi^2_\alpha = \sum_{\rm i}\left(\Delta\alpha_{\rm m}(t_{\rm i}) - \left(\frac{\Delta\alpha_{\rm p}(t_{\rm i})}{\cos\delta_{\rm pe}(t_i)} - \frac{\Delta\alpha_{*}(t_{\rm i})}{\cos\delta_{*_{\rm c}}}\right)\right)^2 \qquad \text{(AII.5)}$$

$$\chi^2_\delta = \sum_i\left(\Delta\delta_{\rm m}(t_i) - \left(\Delta\delta_{\rm p}(t_{\rm i}) - \Delta\delta_{*}(t_{\rm i})\right)\right)^2 \qquad \text{(AII.6)}$$

The predicted offset (the difference between the planet residual and star residual at the occultation time) was sent to L. Wasserman who converted this to a geocentric impact parameter. An offset of Pluto from its ephemeris caused the refined prediction to differ from the initial prediction, which did not include a correction to the ephemeris. This difference moved the predicted shadow path off the Earth. To confirm that no occultation was visible, the close passage of the star to Pluto (an appulse) was observed from Wallace Astrophysical Observatory.

AII.2 The Tr60 Occultation Prediction

The next occultation we planned to observe was Tr60. The ephemeris of Triton was known more precisely than that of Pluto (in part due to the Voyager encounter), so we did not anticipate any significant problems with the initial prediction. We launched an all-out effort for refining the prediction of the shadow path for this event. We recorded strip scans at Wallace Astrophysical Observatory, Lowell Observatory, and Lick Observatory. Stare frames of the star field and Triton approaching the field were recorded at the USNO.

The strip scans for the Tr60 prediction contained an over-exposed image of Neptune. The exposure time is dictated by the declination one is observing, and therefore the "bleeding" (*i.e.*, overexposure) could only be controlled by filter choice. Neptune was bleeding in the east-west direction, so whenever Triton was near eastern or western elongation a neutral density filter was used. For other orbital phases a long pass filter was used. Fortunately, the standard stars were relatively bright, so we did not lose any standards using the neutral density filter.

However, the number of standard stars did fluctuate with the seeing–from 50 to 90 standard stars were identified on a frame (using the densest network available). This

variation in the standard stars could cause changes in the derived celestial coordinates, since each standard position has its own random error associated with it. Removing (or adding) a large number of standards will change the transformation from detector coordinates to celestial coordinates if the random errors do not cancel.

The strip scans provided the best estimate of the shadow path more than three days before the occultation. At that time, both Tr60 and Triton were on the same stare frame field of the 2K CCD at the 61-in telescope at the USNO (see Chapter 3 for details of the instrument and field size). A few days before the occultation, the USNO stare frames provided the best estimate of the shadow path.

AII.2.1 Method Improvements

For this occultation, there were four improvements in our analysis methods: (i) rotating the astrometric network, (ii) removing the "wobble" from the CCD strip scans, (iii) allowing for an error in Triton's ephemeris along track, and (iv) calculating the geocentric impact parameter ourselves. We will discuss each of these in order.

To relate the observed row and columns to celestial coordinates, we use a linear registration of the observed standard star coordinates to an astrometric network. The strip scans have the detector columns aligned with the right ascension of date coordinate. To minimize any higher order terms in the registration, we rotate the astrometric network from the equinox in which we receive it (typically J2000) to an equinox near the time of the strip scan observations. We do not rotate it to "of date" coordinates because that would require a different network for each strip scan (or at least each night).

The next improvement was to remove the low-frequency change in the relative positions of stars on a strip scan (Dunham *et al.* 1991). This observed fluctuation in the relative star centers with time has been termed “wobble”. Unlike stare frames, where the stars are all exposed at the same time, the relative positions of stellar images on a strip are affected refraction changes during the strip scan because all stars are not exposed simultaneously.

To correct for the wobble (which is different for each strip), a dense network of stars is needed. Usually the astrometric network is not sufficiently dense for this purpose. Therefore, a denser network (the dewobble network) is generated from the average of the registered row and column positions for stars that appear on the strips more than a set number of times. Many stars are included in the dewobble network, often more than one thousand (Foust *et al.* 1996). This network cannot be constructed until a sufficient number of strips (at least 25) have been observed to get accurate mean positions for the stars.

The raw row and column centers are transformed to a "standard" row and column coordinate system using a linear registration. The standard row and column coordinate system is related to the celestial coordinates by a scale, s, and an offset (A, D). The scale is chosen to be similar to the image scale of the observations. The offset is chosen to put the origin of the coordinate system in the vicinity of the strip scan.

$$\alpha = sr + A$$
$$\delta = sc + C \qquad \text{(AII.7)}$$

The astrometric network is transformed to the standard coordinate system and the observed centers are transformed to this system by a linear registration of the observed standard stars. The star positions from all strips are now in the same ("standard") row and column coordinate system. Since the wobble is random, we get the true position of the star by averaging many observations; therefore, the dewobble network is the average center for each of the observed stars. We cannot average the centers of the occulting body since it is moving through the field. We model the wobble in each strip and remove it from the body centers.

The wobble is the difference between the centers of the stars (in the standard coordinate system) for a single strip relative to the dewobble network. The wobble is modeled by a Fourier series—the number of terms depends on the number of rows in the strip scan. A longer strip scan can accommodate more terms; typically 50 terms are fit. This Fourier function is removed from the positions of the standard stars (stars from each strip common to the astrometric network), the candidate star and the occulting body. The dewobbled standard star centers are registered to the astrometric network and the observed location of the candidate star and occulting body is derived from the registration coefficients.

Next, we discuss the third improvement of the method: allowing for an along-track error to Triton's ephemeris. We typically assume that the residuals of the occulting body (relative to its ephemeris) are either constant or linear (as discussed above). For Triton we modified the residual model so that we fit for a linear trend in RA and Dec (corresponding to a gross Neptune offset from the ephemeris) and a timing error in the Triton orbit. This timing error is similar to an along-track error — which is the component of the orbit that is least well determined. The timing error should be less than 121 seconds (in 1993) assuming a 0.4 sec error in Triton's orbital period propagating since the Voyager encounter (B. Jacobson, personal communication). Using seventeen nights of Lick strip scan data with both Tr60 and Triton on the same strip (from June 25, 1994 to

July 14, 1994 for a total of 180 strip scans), we found no timing error in the Triton ephemeris. The solution yielded a timing offset of 5 ± 58 seconds.

The final method improvement was to determine the closest approach distance ourselves. The residuals are modeled to predict there value in the future, and the closest approach distance is:

$$p = \mathrm{Min}\left[\left(\frac{\alpha_{*_c}}{\cos\delta_{*_c}} - \left\{\frac{\alpha_{pe}(t)}{\cos\delta_{pe}(t)} + \Delta\alpha_m(t)\right\}\right)^2 + \left(\delta_{*_c} - \left\{\delta_{pe}(t) + \Delta\delta_m(t)\right\}\right)^2\right] \quad \text{(AII.8)}$$

The model RA residual has previously been divided by the cosine of the Declination, see Eq. AII.5.

AII.2.2 Linear Trend and Coordinate System Rotation

One of the most intriguing lessons from the Tr60 prediction came about because we had two astrometric networks. We found that the predictions from separate reductions using two different astrometric networks differed at first, but their linear extrapolations crossed at the event time. Both networks were made by A. Klemola using the Double Astrograph at Lick Observatory. The first included stars only within a few arcminutes of Neptune's ephemeris and used the Perth 70 catalog (Høg and von der Heide 1976) as the primary network. The second network was measured for this event from the same plates, but included a swath nine arcmin in Dec (as opposed to three arcmin) and used the ACRS catalog as the primary network.

Figure AII.1 shows how the predictions from four nights of USNO data varied as more data were included into the solution. The earliest solution is a mean solution of one night's data. The predicted impact parameter is a poor estimate and error is greatly underestimated because we are not able to determine the linear trend. The other three solutions were based on a linear extrapolation of the available data. As more data are added to the solution (and the linear trend is better determined), the solutions agree.

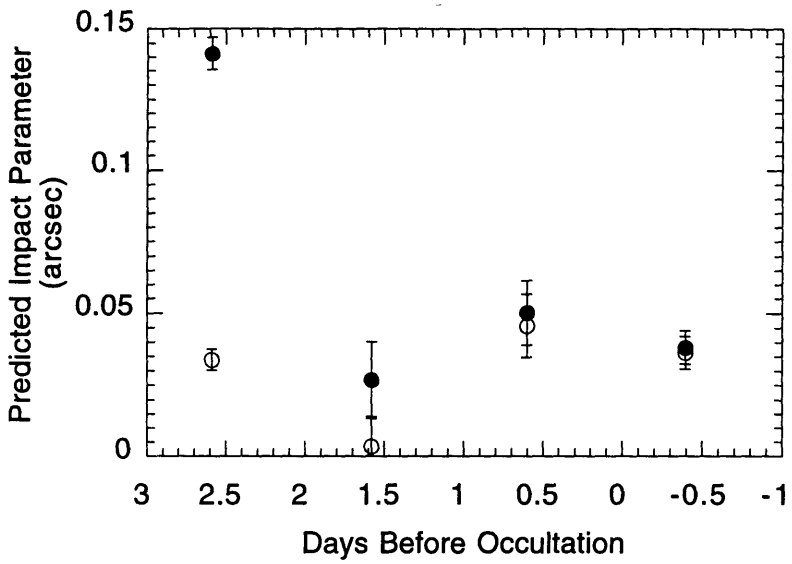

Figure AII.1 USNO prediction based on the two Klemola networks. The *x*-axis is the time before the prediction in days. The open circles are the predicted impact parameter based on the remeasured network; the filled circles are prediction based on the earlier network. Each night 20 frames were taken. The solutions based on the two different astrometric networks clearly converge as more data are included. The first solutions (at about 2.6 days before the occultation) are very different because they do not include a linear trend.

A linear trend will be present in the planet residuals if the coordinate systems of the astrometric network and ephemeris are rotated relative to each other. This convergence of the solutions is just what one would expect if the two reference systems were rotated. There is a large difference between the trends found using the two different networks. Using the original network based on the Perth 70 catalog (Høg and von der Heide 1976), the RA and Dec trends are 0.005 and -0.001 (±0.004) while the same data has RA and Dec trends of 0.020 and 0.045 (±0.004) if reduced with the remeasured network. Figure AII.2 shows the trend in the Dec residuals.

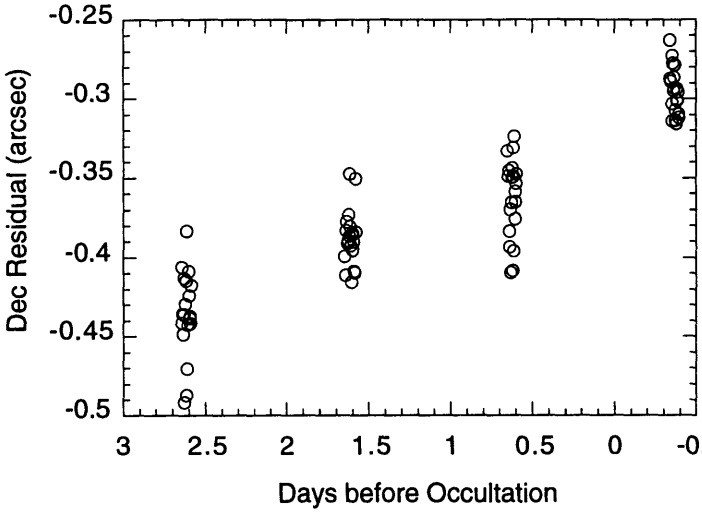

Figure AII.2 The trend in the Dec residuals of the USNO observations. These data were reduced with the second (remeasured) astrometric network. No significant second order effects are evident, as one would expect from the consistency of the prediction as more data is added (see previous figure).

A similar rotation exists in the strip scans. If the linear trend is not included, the occultation prediction will drift as more data is added. For this occultation, the linearly extrapolated strip scan prediction showed a drift with time. The early predictions put the occultation shadow path near Punta Arenas Chile at the southern tip of South America (this is from where the KAO deployed). As more data were added to the prediction, the refined occultation shadow path moved north. For the occultation flight, we flew north and east from Punta Arenas, observed the occultation and refueled in Buenos Aires before returning the Punta Arenas. The refueling stop was necessary because the shadow path was further north than originally anticipated in the deployment plans. Because of this drift, E. W. Dunham investigated the possibility of a field distortion in the Crossley telescope. A field distortion was identified (Dunham *et al.* 1994), and now we correct for it.

AII.2.3 Theoretical Prediction Precision

This section derives an equation for the theoretical error in the impact parameter. We assume the residuals are adequately modeled by a linear trend with time. The factors affecting the precision of the prediction are: (i) time between the mean time of data and the occultation time, (ii) length of the data span, and (iii) the precision of a single strip scan. The first factor is important because the further the mean time of the data is from the occultation time, the more one has to extrapolate the trends into the future. The second factor is also related to any trends in the data; the longer the observations span, the better determined any trend will be.

To estimate the uncertainty in the prediction, we need to know the uncertainty in the extrapolation of the residuals. We will derive the uncertainty in the RA residual at the

occultation time. The declination uncertainty is derived similarly; only the final result is presented. These two uncertainties are projected onto the line connecting the occulting body and star at the closest approach time to get the uncertainty in the impact parameter.

The least-squares fit of the line in Eq. AII.3 gives the following equations for the coefficients (given N observations).

$$a_1 = \frac{\sum_i (t_i - \bar{t})^2 \sum_i \Delta r_\alpha(t_i) - \sum_i (t_i - \bar{t}) \sum_i (t_i - \bar{t}) \Delta r_\alpha(t_i)}{N \sum_i (t_i - \bar{t})^2 - \left(\sum_i (t_i - \bar{t}) \right)^2} \tag{AII.9}$$

$$a_2 = \frac{N \sum_i (t_i - \bar{t}) \Delta r_\alpha(t_i) - \sum_i (t_i - \bar{t}) \sum_i \Delta r_\alpha(t_i)}{N \sum_i (t_i - \bar{t})^2 - \left(\sum_i (t_i - \bar{t}) \right)^2} \tag{AII.10}$$

From the expression for the coefficients, we derive their errors σ_{a_1} and σ_{a_2} (AII.12 and AII.13). The times are assumed to be known exactly, so the only source of uncertainty is the observed residuals $\Delta r_\alpha(t_i)$.

$$\sigma_{a_2}^2 = \sum_j \left(\frac{\partial a_2}{\partial \Delta r_\alpha(t_i)} \right)^2 \sigma_{\Delta r_\alpha(t_i)}^2 = \sum_{j=1}^{N} \left(\frac{N(t_j - \bar{t}) - \sum_i (t_i - \bar{t})}{N \sum_i (t_i - \bar{t})^2 - \left(\sum_i (t_i - \bar{t}) \right)^2} \right)^2 \sigma_{\Delta r_\alpha(t_i)}^2 \tag{AII.11}$$

We define Δ to be the denominator of Eq. AII.12 and simplify the equation by noting the second term in the denominator is zero. We assume each data point has the same error ($\sigma_{\Delta r_\alpha} = \sigma_{\Delta r_\alpha(t_i)}$).

$$\sigma_{a_2}^2 = \frac{N}{\Delta} \sigma_{\Delta r_\alpha}^2 \tag{AII.12}$$

A similar method yields the following equation for σ_{a_1}.

$$\sigma_{a_1}^2 = \frac{\sigma_{\Delta r_\alpha}^2}{\Delta} \sum_i t_i^2 \tag{AII.13}$$

Now that we have the error in the coefficients, we can get an expression for the RA error at the event time, $\sigma_{\Delta r_\alpha(t_o)}$.

$$\sigma_{\Delta r_\alpha(t_o)}^2 = \sigma_{a_1}^2 + \sigma_{a_2}^2 (t_o - \bar{t})^2 \tag{AII.14}$$

Substituting Eqs. AII.12 and AII.13 into AII.14 gives the full equation:

$$\sigma^2_{\Delta r_\alpha(t_o)} = \frac{\sigma^2_{\Delta r_\alpha}}{\Delta}\sum_i t_i^2 + \frac{N}{\Delta}\sigma^2_{\Delta r_\alpha}\left(t_o - \bar{t}\right)^2 \qquad \text{(AII.15)}$$

which simplifies to

$$\frac{\sigma^2_{\Delta r_\alpha(t_o)}}{\sigma^2_{\Delta r_\alpha}} = \frac{1}{\mathrm{N}}\left(1 + \frac{\mathrm{N}\left(\mathrm{t}_o - \bar{\mathrm{t}}\right)^2}{\sum_i \left(\mathrm{t}_i - \bar{\mathrm{t}}\right)^2}\right) \qquad \text{(AII.16)}$$

The equation for the Dec error in the residual is:

$$\frac{\sigma^2_{\Delta r_\delta(t_o)}}{\sigma^2_{\Delta r_\delta}} = \frac{1}{N}\left(1 + \frac{N\left(t_o - \bar{t}\right)^2}{\sum_i \left(t_i - \bar{t}\right)^2}\right) \qquad \text{(AII.17)}$$

The relevant quantities are the quality of each data point $\sigma_{\Delta r}$, the time over which the result is extrapolated ($t_o - \bar{t}$) and the data coverage (which is in the sums).

Finally we get an equation for the theoretical error in the geocentric impact parameter, where θ is the angle between the RA direction and the direction of the occulting body's motion.

$$\sigma_p^2 = \sigma^2_{\Delta r_\alpha(t_o)}\sin^2(\theta) + \sigma^2_{\Delta r_\delta(t_o)}\cos^2(\theta) \qquad \text{(AII.18)}$$

Now that we have derived an equation for the theoretical precision of a prediction we can compare that with our formal error from the Tr60 prediction (Figure AII.3). The theoretical curve assumes an individual strip uncertainty of 0.035 arcsec and that nine images were taken each night. It also has the observing schedule. The desired precision for a Triton occultation is about 0.02 arcsec, or about one-third of Triton's radius, so that a 3σ error would yield a grazing occultation. The desired precision for a Chiron occultation is also indicated. The formal error for the prediction based on the Lick strip scan data is indicated by the open circles. Note that this formal error is an underestimate of the actual error, because of a recently discovered field distortion (Dunham *et al.* 1994).

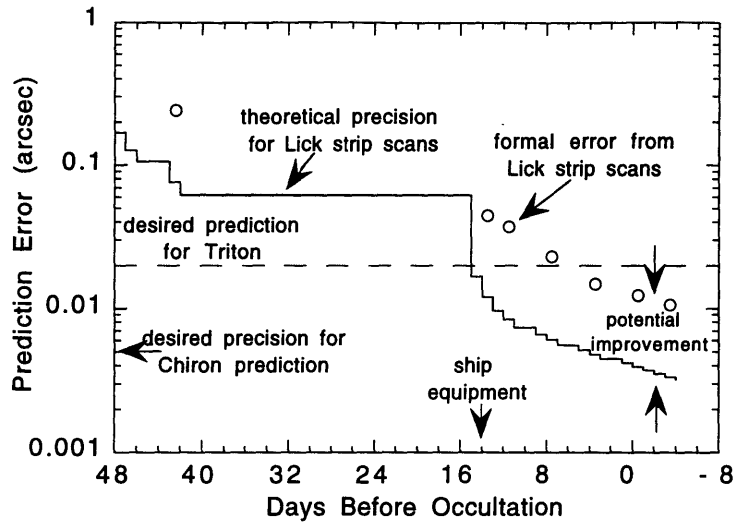

Figure AII.3 Theoretical and actual prediction precision from Lick strip scans for the Tr60 event. The assumptions in the theoretical curve are detailed in the text. A typical lead time for shipping equipment to a foreign country is indicated. Notice that there is room for improvement. The desired precision for both a Triton and Chiron occultation prediction are indicated (for each this is about a third of a radius).

AII.3 The Ch02 Occultation Prediction

Predicting an occultation by Chiron tested our methods. The size of Chiron's nucleus was unknown. If the nucleus were 100 km in radius, then its angular radius would be 0.015 arcsec (given an Earth-Chiron distance of 9.302 AU). We prefer for the prediction to have a 3σ error less than the radius of the occulting body. For this event, that would be 0.005 arcsec. The prediction was complicated by the fact that the event occurring near the beginning of the Chiron season, so astrometric data in advance of the event were slim.

The event was predicted to occur over the western United States (Bus *et al.* 1994). It was a good event to test our prediction abilities, given that the deployment was not very expensive, and it would occur before we has to commit ourselves to a major deployment for the Ch08 occultation in South America.

We had data for the prediction only from the Crossley telescope at Lick Observatory. There were about 13 strips per night for 12 nights between 1993 Oct. 28 to 1993 Nov. 9, each with an accuracy of 0.035 arcsec. The altitude of the observations was between 15 and 46 degrees. Some of the lowest altitude strip scans could not be reduced because of the effects of color refraction elongating the images. The astrometric network for this analysis was supplied by Brian Skiff from PDS measurements of films taken at the 46-cm Schmidt telescope at Palomar Mountain by E. M. and C. S. Shoemaker as a part of the Palomar Asteroid and Comet Survey. The ACRS catalog was used as a primary astrometric network.

We can estimate the actual impact parameter for this event from observations of the event. Bus *et al.* (1996) assumed that the Palomar chord just missed the nucleus and estimated the largest Chiron possible given this condition. From this, we estimate that the Terra del Sol light curve was approximately 30 kilometers north of the center which gives a geocentric impact parameter of 0.239 arcsec.

Figure AII.4 shows the time history of the actual error in the prediction, the formal error and the theoretical precision the given data schedule. The actual error in the prediction is the absolute value of the difference between the predicted impact parameter and the actual impact parameter as determined above. As seen in the figure, the formal error is a good estimate of the actual error (for this prediction), and neither is particularly far from the theoretical precision that would be expected. The reduction process did not include dewobbling until 1.89 days before the occultation. It was only at this time that we had enough strips to make a reasonable network for dewobbling. We had data containing both objects only five nights before the event.

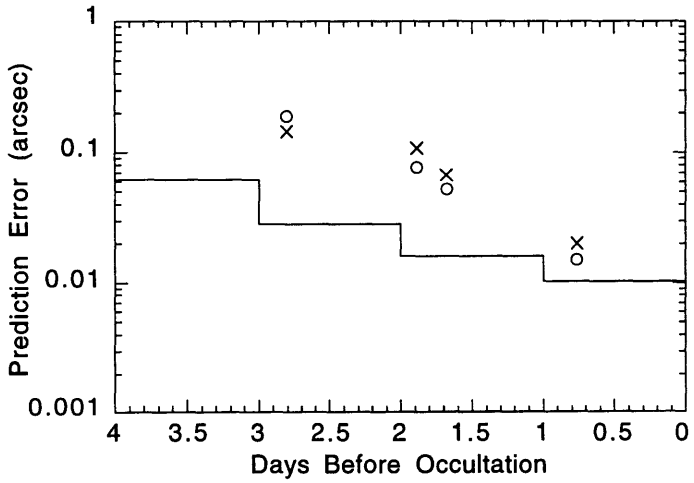

Figure AII.4 The precision of the Ch02 occultation prediction as a function of time. The circles are the real error estimated from the observed chord, see text; the x's are the formal error from the prediction and the solid line is the theoretical precision of the data. Only data containing both objects (which started 5 nights before the occultation) are shown.

AII.4 The Ch08 Occultation Prediction

We expected the Ch08 occultation prediction to be more precise than the Ch02 event because the event was closer to opposition (so we could get more data per night and at higher altitudes). In general, this was true. There were more data, the data were higher quality (observed closer to the meridian) and the precision of the final prediction was better. However, precision was not the problem in the Ch08 occultation prediction. There was a systematic effect that made this prediction difficult. The systematic problem was a faint companion about 3 arcsec away from Ch08. Ch08 and the companion were unresolved in the Lick and Wallace strip scans. However, they were

resolved in the USNO stare frames. From images of the field taken before Ch08 and Chiron were on the same frame with the USNO 61-in telescope, we could determine the relative magnitude and separation of Ch08 and its companion. This information was used to correct our strip scan predictions of the blended pair.

Due to bad weather in Flagstaff, we had only one night of USNO stare frames (13 images) with Ch08 and Chiron together before the occultation. Relative to Triton, Chiron moves across the sky faster. This is a disadvantage in prediction refinements because there are fewer nights when the star and Chiron can be observed on the same strip scan or stare frame.

The final prediction was flown by the KAO and it placed us 107 km from the center of Chiron (see Appendix IV for the reduction of the USNO data). The prediction was in error by 0.018 arcsec (the Earth-Chiron distance was 7.87 AU). If we would have had another night of USNO imaging data before the occultation (so a linearly extrapolated solution could be constructed), we probably would have been in the shadow path of the nucleus. As it turned out, we probed the near-nucleus coma, detected two discrete jets and possibly a bound coma (Elliot *et al.* 1995).

AII.5 The P20 Occultation Prediction

Predicting an occultation by Pluto (or Charon) is difficult because the two bodies are not resolved in the observations. To predict precisely where one of the bodies will be, both the mass ratio and the light ratio (which is a function of orbital phase) of the bodies must be known.

The following is a description of how the observations are corrected to be Pluto center positions from observations of the instantaneous center of light of the system (an analogous method can be applied to derive Charon center positions). The general plan involves using the light curves and relative masses of Pluto and Charon to make the corrections from the mean center-of-light ephemeris to the center of Pluto (ignoring, for now, the center-of-Pluto light to center of disk offset that arises from non-uniform albedo distribution).

There are two corrections necessary: (i) a correction of each observation to make it a mean center of light observation from an instantaneous center of light observation and (ii) a correction of a mean center of light prediction to a center of Pluto prediction. The first correction is applied to all the data and the resulting position is compared to the ephemeris (which is assumed to be a mean center of light ephemeris). The second correction is applied at the predicted closest approach time to convert from a mean center of light prediction to a center of Pluto prediction.

These corrections will be applied in the uv plane with the Pluto-Charon barycenter at the origin [see Elliot *et al.* (1993) for a definition of the coordinate system]. The fraction of system light (as a function of Charon's orbital phase) and system mass attributable to Charon are defined as $f_l(\varphi)$ and f_m. Eq. AII.19 gives the light fraction due to Charon as defined by imaging data taken at the 88-in telescope at MKO.

$$f_l(\varphi) = 0.16103 + 0.019528\cos(2\pi\varphi - 0.16604) + 0.0048752\cos(4\pi\varphi + 0.41779) \quad \text{(AII.19)}$$

Since the equations for u and v are analogous, only the equations for u will be derived. The rotational phase is φ and it varies from 0.0 to 1.0. The variables $u_p(\varphi)$ and $u_c(\varphi)$ are defined to be the coordinates of Pluto and Charon (from the barycenter), and $u_\ell(\varphi)$ is the coordinate of the center of light, which given by the equation:

$$u_\ell(\varphi) = [1 - f_\ell(\varphi)]u_p(\varphi) + f_\ell(\varphi)u_c(\varphi) \quad \text{(AII.20)}$$

By definition, the u coordinate of the barycenter is 0:

$$0 = (1 - f_m)u_p(\varphi) + f_m u_c(\varphi) \quad \text{(AII.21)}$$

We define the following quantities:

$$u_{pc}(\varphi) \equiv u_c(\varphi) - u_p(\varphi) \quad \text{(AII.22)}$$

$$f_{m\ell} \equiv f_\ell(\varphi) - f_m \quad \text{(AII.23)}$$

Subtracting Eq. AII.21 from Eq. AII.20 gives the following expression for $u_\ell(\varphi)$:

$$u_\ell(\varphi) = [f_\ell(\varphi) - f_m][u_c(\varphi) - u_p(\varphi)] = f_{m\ell}(\varphi)u_{pc}(\varphi) \quad \text{(AII.24)}$$

The average of $u_\ell(\varphi)$ over the orbital phase is the mean center of light position:

$$\bar{u}_\ell = \int_0^1 u_\ell(\varphi)d\varphi \quad \text{(AII.25)}$$

Next we want the equation for the coordinate of Pluto relative to the center-of-light ephemeris. Rearranging Eq. AII.20 gives:

$$u_p(\varphi) = u_\ell(\varphi) - f_\ell(\varphi)u_{pc}(\varphi) \quad \text{(AII.26)}$$

Subtracting $\bar{u}_\ell$ from both sides, we get:

$$u_{\ell p}(\varphi) \equiv u_p(\varphi) - \bar{u}_\ell = u_\ell(\varphi) - \bar{u}_\ell - f_\ell(\varphi)u_{pc}(\varphi) \quad \text{(AII.27)}$$

This simplifies to:

$$u_{\ell p}(\varphi) = -f_m u_{pc}(\varphi) - \bar{u}_\ell \qquad \text{(AII.28)}$$

The analogous equation for the v component of Pluto relative to the mean center of light is:

$$v_{\ell \mathrm{p}}(\varphi) \equiv v_{\mathrm{p}}(\varphi) - \bar{v}_\ell = -f_{\mathrm{m}} v_{\mathrm{pc}}(\varphi) - \bar{v}_\ell \qquad \text{(AII.29)}$$

Once we have evaluated Eqs. AII.28 and AII.29 for the desired phase angle (or angles) these values are transformed to RA and Dec via the *fg* plane and the XYZ, coordinate system [see Elliot *et al.* (1993) for a description of these rotations]. This is the correction to apply to the prediction to go from a mean center of light prediction to a center of Pluto prediction. In these transformations, as an approximation, we use a constant value for the sub-Earth latitude on Pluto, the position angle of the projection of Pluto's rotational north pole onto the *fg* plane, and distance to Pluto-Charon.

Similar expressions are used to correct the observations (which are an instantaneous center of light measurement) to be a mean center of light observation:

$$u_{\ell\bar{\ell}}(\varphi) \equiv \bar{u}_\ell - u_\ell(\varphi) = \bar{u}_\ell - f_{\mathrm{m}\ell}(\varphi) u_{\mathrm{pc}}(\varphi) \qquad \text{(AII.30)}$$

$$v_{\ell\bar{\ell}}(\varphi) \equiv \bar{v}_\ell - v_\ell(\varphi) = \bar{v}_\ell - f_{\mathrm{m}\ell}(\varphi) v_{\mathrm{pc}}(\varphi) \qquad \text{(AII.31)}$$

To make the correction, we first convert $u_{\ell\bar{\ell}}(\varphi)$ and $v_{\ell\bar{\ell}}(\varphi)$ to RA and Dec, and then we add the results to the observed position to obtain the position of the mean center-of-light from the observations.

The residuals are constructed to calculate an impact parameter from ephemeris and the mean center-of-light observations. An offset of the star from its catalog position is also calculated. From this we generate a closest approach time and impact parameter. Here is where the remaining difference between a typical prediction and a Pluto-Charon prediction arises. This prediction generated with the mean center of light ephemeris needs to be corrected to the center of Pluto. The expressions in Eqs. AII.30 and AII.31 are added to this prediction to create a body-centered occultation prediction.

At the time of the P20/C20 events, the separation of Pluto and Charon was 0.66 arcsec which is approximately the diameter of the Earth at the distance of Pluto. Both shadows passed just off the edge of the Earth — Pluto to the north and Charon to the south! Because we were losing events that were predicted to be on the Earth, we decided to keep our eye on high SNR events whose shadows were predicted to be off the Earth. This was critical to the observation of the Tr148 occultation, since the shadow path was originally estimated to be off the Earth to the north.

AII.6 The P28 Occultation Prediction

For this occultation, we once again geared up the prediction team. Data for the prediction was recorded at four different telescopes. The number of observations as well as the span and data type is given in Table AII.2. The table also has an estimated closest approach distance for Pluto from P28 from the whole dataset (some of these include data after the closest approach). All the solutions indicate that no occultation would be visible from Earth because the impact parameters are greater than 0.3 arcsec.

Table AII.2 Data and Predictions for the P28 Occultation

Site	Data Type	Number of Nights	Data Span	Num. of Obs. P-C/P28	Mean C/A (arcsec)	Extrapolated C/A (arcsec)
Lick	Strips	27	5/17 - 7/09	164/163	0.547 ± 0.013	0.370 ± 0.016
USNO	Transit Obs.	28	3/13 - 7/12	21/28	0.487 ± 0.048	0.466 ± 0.068
USNO	Stare Frames	3	7/05 - 7/07	63/62	0.405 ± 0.067	0.442 ± 0.041
WAO	Strip Scans	27	4/25 - 7/4	242/163	0.574 ± 0.017	0.668 ± 0.035

For this occultation, the main improvement came in the calculation of the impact parameter. For this occultation (and future ones), the predicted values of the occulting body and star residuals at the event time are used to correct the reference position for the occulted star. This new position defines the *fgh* coordinate system, see Elliot *et al.* (1993). Next, the ephemeris coordinates are expressed in this coordinate system and the geocentric closest approach distance is determined by the minimum separation of the occulting body (as defined by the ephemeris) and the origin of the *fgh* system (where the star is located). This can easily be generalized to give an impact parameter for a given site, see Eq 3.7 of Chapter 3.

A description of the Lick strip scans for this prediction and the P20 prediction is presented in Foust *et al.* (1996). The analysis of strip scans from the Crossley telescope at Lick Observatory was improved for the P28 occultation by removing the field distortion. To do this we needed to redesign our observing plan. For each strip scan that contained Pluto and P28, we also observed one strip shifted north and another shifted south. In this way we could determine the field distortion each night from the relative differences in star centers.

AII.7 The Tr148 Prediction

For the Tr148 occultation, as usual, we had a diverse set of data: strip scans from the Crossley telescope at Lick Observatory and from the 24-in at Wallace Astrophysical Observatory, two sets of transit circle observations (from CAMC and the USNO) and stare frames from the 61-in at the USNO. A schematic of the star field for the USNO stare frames is shown in Figure AII.5. Some field stars are indicated along with the nightly position of Triton.

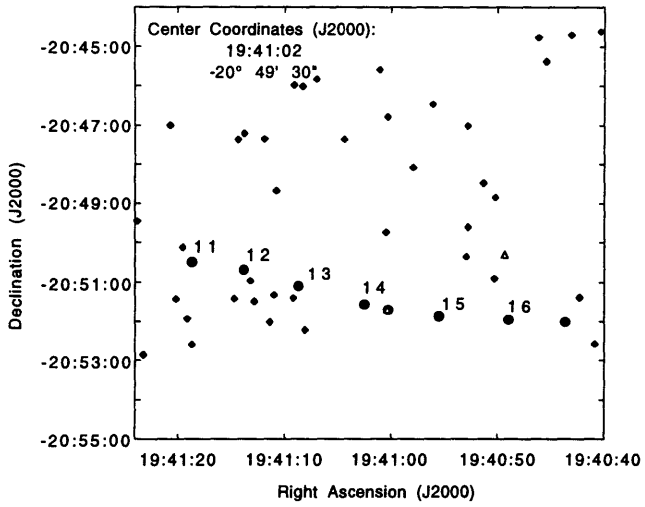

Figure AII.5 Tr148 field for USNO observations. The circles represent the location of Triton at 0 hr UT on the dates in August indicated. The triangles are stars measured by the CAMC (including Tr148). The diamonds are stars in our secondary astrometric network.

To reduce the strip scans we used an astrometric network measured by the CAMC (B. Argyle, personal communication). There were approximately 24 standard stars on a Lick strip scan. However, this network is not dense enough to use in the reduction of the USNO stare frames. We constructed a secondary astrometric network from our dewobble network for the strip scans. From Figure AII.6, one can see that the astrometric network stars do not go below a given declination. This is the lowest declination covered by the strip scans.

The field distortion of the Crossley telescope was calculated and removed from the Lick data each night. The strip scan observations were also dewobbled. The observations were used to generate residuals for the star and planet. The mean of these residuals and the linear extrapolation of these residuals (in RA and Dec), was used in conjunction with the DE211 ephemeris for Neptune and the NEP016 Triton ephemeris to determine the closest approach between the star and satellite.

The final predictions (both mean and extrapolated) from all the datasets are given in Table AII.3. At the time, we did not know that Tr148 was a double star. The predictions refer to the center of light of the blended Tr148. The number of observations of Triton and Tr148 are listed. The radius of Triton is 0.06 arcsec and the radius of the

Earth at the Triton distance is 0.30 arcsec. To position ourselves in the shadow path, the uncertainty in the prediction needs be less than a Triton radius and preferably less than 1/3 of a Triton radius. For impact parameters more than 0.3 arcsec, the centerline of the shadow will be off the Earth. Figure AII.6 shows the shadow path predicted using the CAMC measurement of the star.

Table AII.3 Final Predictions for Tr148 Occultation

Observatory	Mean Prediction	Extrapolated Prediction	Number of Obs. Triton/Tr148
WAO	0.170 ± 0.029	0.424 ± 0.057	36/72
Lick	0.258 ± 0.011	0.282 ± 0.023	150/154
USNO Transit	0.192 ± 0.076	0.897 ± 1.292	25[b]/15
USNO 61 in	0.220 ± 0.005	0.312 ± 0.046	52/52
CAMC	0.302 ± 0.129	n/a	0/1[b]

[a] observed Neptune
[b] CAMC may have measured the star multiple times, we received one position from them.

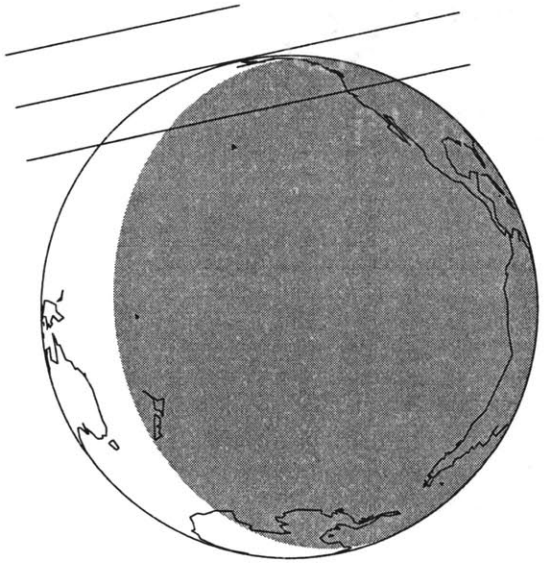

Figure AII.6 The predicted shadow path for the Tr148 occultation. This globe depicts an impact parameter of 0.30 arcsec. This prediction used the CAMC position for Tr148 and the DE211 ephemeris for the barycenter of Neptune and NEP016 for the motion of Triton about the barycenter. The shaded region indicates where the Sun is below -12°.

Table AII.4 shows final solutions for the closest approach distance between the blended Tr148 and Triton using pre- and post-event data. The extrapolated solutions from Lick Observatory strip scans and USNO stare frames are within one standard deviation of each other.

Table AII.4 Final Astrometric Solutions

Observatory	Data Type	Mean Prediction	Extrapolated Prediction	Number of Obs. Triton/Tr148
Lick	Strip Scans	0.264 ± 0.010	0.273 ± 0.018	183/189
USNO	Stare Frames	0.238 ± 0.004	0.270 ± 0.004	110/110

From the multiple chord observations of both the Tr148A and Tr148B occultation (Chapter 4), we find the closest approach distance between Tr148A and Triton was 0.279 ± 0.003 arcsec, and for Tr148B it was 0.197 ± 0.001 arcsec. The predictions above refer to the mean center of light of Tr148. To adjust the individual predictions derived from the occultation chords to get a mean center of light prediction for comparison, we use the separation of the stars in the track of the occultation shadow and the intensity ratio of the two stars (Chapter 5). The separation of the two stars in the shadow path is derived from the *fg* offsets of Chapter 4 and the angle of the track relative to the g axis is 102°. The prediction of Tr148A should be shifted south by 0.036 ± 0.002 arcsec to derive a center of light prediction. This is an impact parameter of 0.243 arcsec which is south of the predictions, by less than a Triton radius and more than the formal error.

AII.8 Conclusions

Currently, we are able to accurately predict occultations by solar system bodies such as Triton and Pluto (with an angular radius of ~0.06 arcsec) as shown by the successful observations of Tr60 and Tr148. Occultations by bodies like Chiron (with and angular radius of 0.015 arcsec) are possible to predict barring any unforeseen systematic effects (such as an unresolved faint companion near the occulted star) or given multiple nights of high-quality astrometric stare frames before the event.

We have shown the evolution of our occultation prediction methods over the last few years. We have included all known affects into our reduction procedure. This has entailed rotating the astrometric network to an equinox near date to reduce the rotation terms in the registration, removing the wobble, removing field distortion, accounting for the rotation between the coordinate systems of the astrometric network and planetary ephemerides, and correcting the Pluto predictions for the center-of-light offset.

AII.9 Future Improvements

While our methods are able to accurately predict occultations by solar system bodies such as Triton and Pluto, the effort required for such a prediction is significant. A typical prediction is produced by a team with approximately eight weeks of a technical staff member, six weeks of a graduate student, six weeks of two undergraduate assistants and three weeks of a professor. This is a substantial effort. This could be decreased by automating some tasks with software.

One improvement would be to upgrade the current center-finding section of the analysis to identify given stars, not all the stars on every strip. We would have to identify more than just the astrometric standard stars so that we could construct the dewobble network. This would save time in finding centers of unused stars and eliminate the step of comparing the randomly numbered star list to identify astrometric standard stars (since the stars could be identified in the same order on each strip). This improvement could also result in more consistent positions for a given star across strip scans because the set of standard stars would be constant.

Another software improvement would be to have a program for constructing the dewobble network. Currently, we search through all observed strips to identify the stars that are common to most strips. This is time consuming and could be automated. In addition, the dewobbling should be implemented in C (instead of *Mathematica*). *Mathematica* is slower.

We need to improve our mid- to long-range prediction capabilities. Too often, resources and time are spent on an event that is not visible. Improved mid-range predictions would alleviate these problems, while improved long-range predictions would improve the timeliness of our telescope proposals. We have begun requesting observations at transit telescopes more than a year in advance to improve this.

Table AII.5 presents the magnitudes of three Triton occultation candidates, three Pluto occultation candidates and Tr148 for reference. Table AII.6 present refined predictions for the same occultation candidates. The position and V magnitude of Tr148 is from the CAMC (B. Argyle, personal communication). The V magnitudes and positions for the other stars are from the USNO transit circle (R. Stone, personal communication), except for Tr180 which was measured by the CAMC. The occultation predictions used the DE403 ephemeris for the barycenter of the Neptune and Pluto systems. The orbits of Triton and Pluto about the barycenter is given by the NEP016 and Plu006 models. No correction has been made for the offset of either Triton or Pluto from their ephemerides. The uncertainties in the geocentric impact parameter based on

the random error in the star positions are less than a Triton (or Pluto) diameter and more than a Triton (or Pluto) radius. We checked the Pluto candidate stars to see if any would be occulted by Charon. No Charon occultations visible from Earth were found.

Table AII.5 Occultation Candidate Magnitudes

Candidate Star	Body	Date	V	J	K
Tr148	Triton	1995 08 14	12.96 ± 0.03	11.78 ± 0.09	10.982 ± 0.11
Tr169	Triton	1996 08 17	N/A	11.77 ± 0.09	10.57 ± 0.16
Tr176	Triton	1997 07 18	12.53 ± 0.02	11.23 ± 0.09	10.51 ± 0.16
Tr180	Triton	1997 11 04	10.52 ± 0.04	11.96 ± 0.09	11.20 ± 0.15
P30	Pluto	1996 04 17	15.61 ± 0.01	N/A	N/A
P30.04	Pluto	1996 06 03	16.11 ± 0.05	N/A	N/A
P31	Pluto	1996 07 28	15.84 ± 0.02	N/A	N/A

N/A: Not Available

Table AII.6 Refined Predictions For Selected Candidates

Candidate Star	Date UT	RA (J2000)	Declination (J2000)	Impact Parameter (arcsec)	Comment
Tr176	1997 07 18 10:17	20:02:51.279 ± 0.004	–20 00 57.166 ± 0.101	0.019 ± 0.097	See globe.
Tr180[a]	1997 11 04 05:09	19 57 32.256 ± 0.005	–20 18 18.91 ± 0.08	0.34 ± 0.08	See globe.
P30	1996 04 17 04:03	16:12:58.112 ± 0.004	–07 30 48.196 ± 0.064	0.412 ± 0.063	Tracks South of Earth
P30.04	1996 06 03 12:36	16:08:15.271 ± 0.002	–07 16 36.297 ± 0.072	0.172 ± 0.072	See globe.
P31	1996 07 28 03:08	16:04:02.016 ± 0.004	–07 23 46.743 ± 0.060	0.426 ± 0.062	Tracks North of Earth

[a] Measured at CAMC (B. Argyle, personal communication)

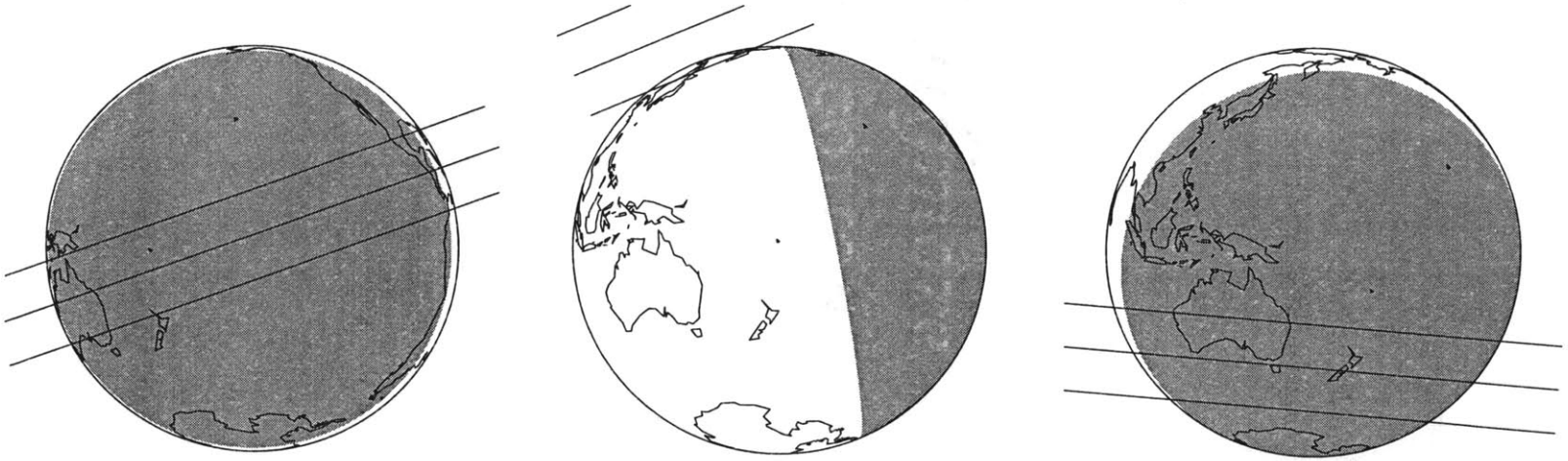

Figure AII.8 Tr176, Tr180 and P30.4 occultation shadow paths as viewed from the occulting body. The right panel has the predicted shadow path from the occultation of Tr176. The middle globe shows the predicted shadow path for the Tr180 occultation and the rightmost globe shows the predicted shadow path for the P30.04 occultation. The Tr176 event occurs near opposition. For the nominal path, observers could be stationed in Australia and New Zealand. Even a shift of the path north is acceptable. A shift of ~0.1 arcsec would put the IRTF and the western US in the path. The southern limit of the Tr180 occultation path grazes the Earth at the north. The predicted shadow path for the P30.04 event crosses Australia and New Zealand. No offset of Pluto from its ephemeris has been included in this prediction.

Appendix III. Adapting Our CCD Photometer to the IRTF

For the simultaneous visible and infrared observation of the Tr148B occultation at the IRTF, we mounted our portable CCD system (Buie *et al.* 1993) on the optical port of the NSFCAM instrument (Shure *et al.* 1994). The NSFCAM instrument can operate with three different pixel scales (0.310, 0.153 and 0.056 arcsec/pix) and the pixel scales change the location of the focal plane of the visible light from the optical port interface on NSFCAM. The mount design presented in this appendix assumes that NSFCAM is being operated at 0.310 arcsec/pixel. At this scale, the distance from the focal plane to the interface is –34.0 mm (Mark Shure, personal communication). This puts the focal plane over 1 inch inside the dewar. Therefore, we need reimaging optics to put our detector at a focal plane. The focal plane distance from the interface for the other two scale (0.153 arcsec/pix and 0.056 arcsec/pix) is +38.0 mm and +107.8 mm (both are outside of the dewar).

The focal ratio at the optical port for is f/37.2 and the focal-plane scale is 1.85 arcsec/mm (Mark Shure, personal communication). The PCCD pixels are 23 microns square making the nominal image scale 0.042 arcsec/pixel which is too small. The field of view (for the whole detector) would be about 17 arcseconds. This would create difficulty in finding objects and keeping them in the desired subframe. Therefore, we use a relay lens to increase the image scale (and create a focal plane for the detector).

We choose a pixel scale for the PCCD observations of 0.3 arcsec/pixel. This provides a well-sampled image compared to the seeing. This pixel scale sets the magnification required by the mount to be –0.14 (0.042/0.3). The magnification is less than 1 because we need to increase the pixel scale. The magnification is the ratio of the distance from the relay lens to the focal plane inside the dewar and the distance from the relay lens to the detector. Both distances are measured relative to the relay lens with the positive direction defined to be to the right in Figure AIII.1.

We used first-order optics to determine the focal length and diameter of the relay lens while satisfying our demagnification requirement and keeping the entire length less than 18 inches. As a result we chose a field lens with a 47 mm focal length and a 28 mm diameter; see Figure AIII.1. This lens has too small of a diameter to image the entire field of the CCD, so the field is vignetted. The usable field is the area imaged by the incoming beam (1.85 arcsec/mm × 28 mm) and has a diameter of about 51 arcsec, see Figure AIII.2.

To increase the size of the usable field, we would need a lens with the same focal length (since the focal length defines the demagnification) and a larger diameter. This type of lens is difficult to find.

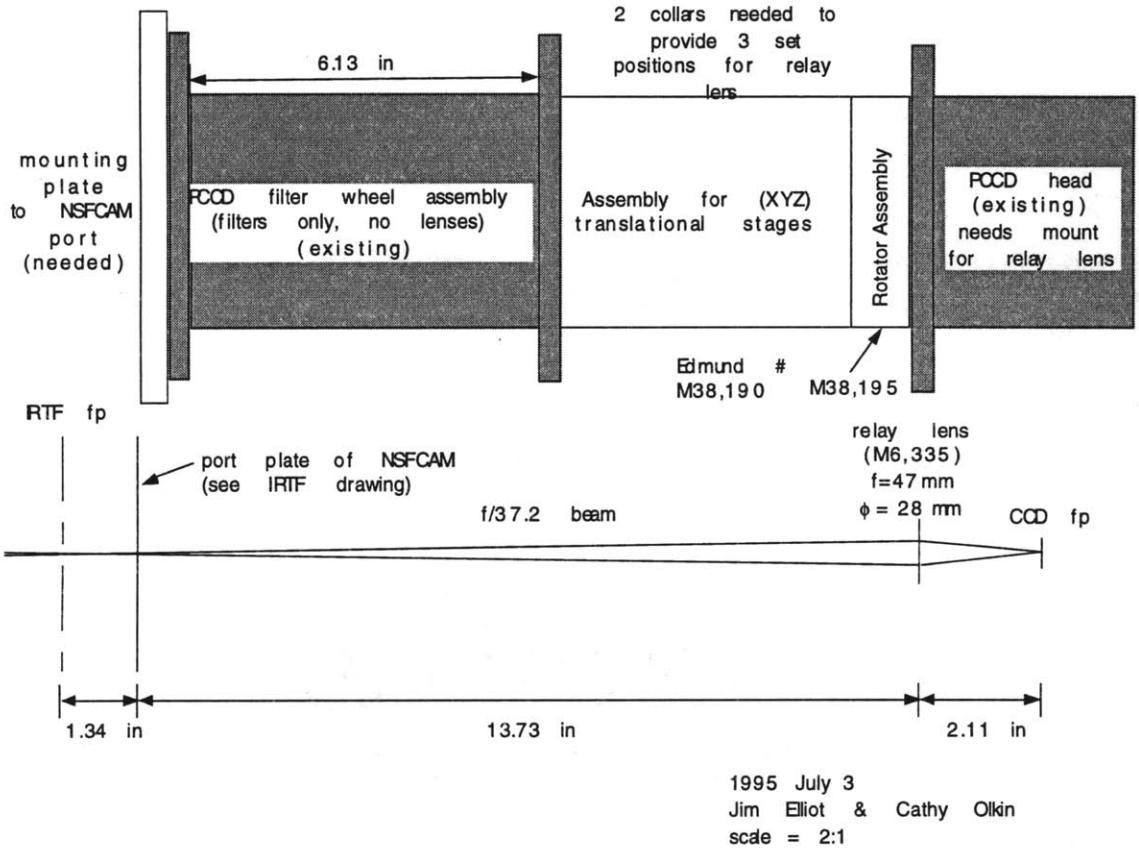

Figure AIII.1 The optical and mechanical drawing of the PCCD mount on the optical port of NSFCAM. The mechanical diagram shows the mounting plate to the port on NSFCAM, the standard PCCD filter wheel, an assembly of 3 degree of freedom translational stages, a rotational stage and the camera head. The Edmund's part numbers are indicated for the translational stage, rotational stage and relay lens. The optical diagram shows the f/37.2 beam passing through the focal plane inside the dewar, exiting the dewar 1.34 inches after the focal plane. The f/# of the beam is reduced by a factor of 7.14 at the relay lens, where the field outside 51 arcsec is vignetted by the lens. The demagnified field reaches the detector at the focal plane. Original drawing scale was 2:1; this reproduction was reduced to 60%.

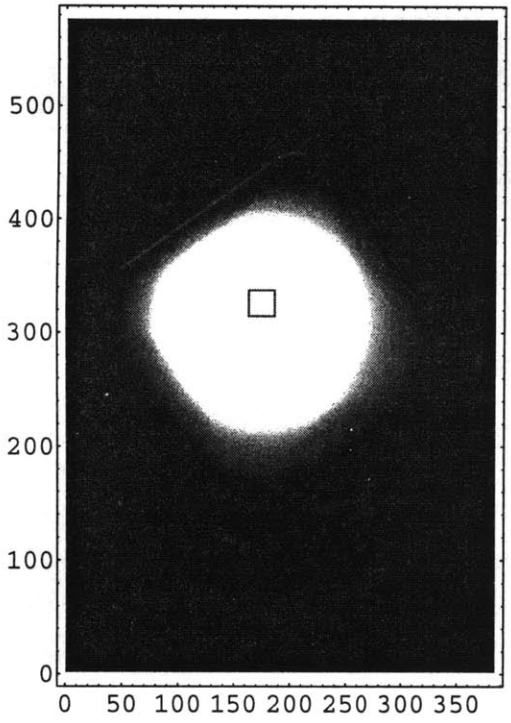

Figure AIII.2 The vignetted field of view. This is an image of an evenly illuminated surface taken with the MIT PCCD mounted on the optical port of the NSFCAM. The field of view is vignetted outside of the relay lens (the dark area in this flat field image). The box is the subframe used to record the blended image of Triton-Tr148 during the 1995 occultation. The subframe was located in the upper half of the detector to utilize the frame-transfer read out scheme.

To design an instrument mount, more than an optical design is needed. The mechanical system needs to be designed as well. The mechanical design had to provide: (i) a focus mechanism, (ii) a means to translate and rotate the field, (iii) filters, (iv) support for the relay lens, and (v) an interface to the optical port. Constraints on the mechanical design included overall length and weight of the system.

The PCCD is a modular system with separate sections for the filter wheel, reducing optics, and camera head. Whenever possible in the design, we used existing sections of the PCCD. The final design included the filter wheel section and the camera head sections. We purchased a micrometer stage that provides three degrees of freedom. This joins the filter wheel section and provides a mechanism for fine-scale focusing of the field as well as translation of the field in two perpendicular directions in the plane of the detector. Each micrometer has 2 inches of motion. We found little need to translate the field in the plane of the detector. The CCD proved to be well aligned with the IR detector. If more than 2 inches of adjustment is needed for focusing, the position of the relay lens can be adjusted (for coarse focusing) by adjusting the position of the aluminum barrel in which the lens is held. A nylon screw holds the aluminum barrel in place. Care is required in adjusting the nylon screw (it broke during the observing run).

The rotational stage allows the observer to rotate the field to align rows and columns with RA and Dec. Other rotations may be desirable depending on the observation. The instrument extends about 16 inches from the NSFCAM port. This provides enough clearance for other instruments on the multiple-instrument mount at the IRTF.

When mounting the PCCD on the optical port, move the telescope to zenith and align the top of the instrument (defined by the *y*-axis micrometer) about 45° clockwise from the top. The *x*-axis micrometer stage is 90° further counterclockwise. In this orientation, the screws and screw holes will be aligned and the weight of the translational stages is on the springs.

In the initial configuration (before the instrument is focused and the field centered and adjusted), set the 3 translational micrometers to 1.0 (the middle of the 2 inch span) and the rotational stage to 0°. At the NSFCAM image scale of 0.3"/pixel, the barrel in which the relay lens sits should be flush with the micrometer stage faceplate. The thumbscrews that square-up the rotator plate should be loose as well as the 3 screws on the focus bracket and the lock screw on the *x* and *y* brackets. The following steps will take the instrument from the state described above to focused with the field located at the desired position on both the NSFCAM and PCCD detectors:

1. Center and focus bright object on NSFCAM display. Find the object in PCCD frame. Note that the object was always near the center of the PCCD field when it was near the center of the NSFCAM field. Move the telescope to locate object in the center of the unvignetted field.
2. Focus PCCD. Use the focus micrometer and be sure all 3 screws are loose. Leave the screws loose. One person will be in the telescope dome moving the micrometer stage, while another is inside the warm room accessing the focus.
3. Rotate the field to have North up in PCCD (this rotation is optional, see below). Make note of rotation angle. Lock the rotation – just the lock screw not the thumbscrews. Read out the rotation angle. Relieve weight of rotation bearing with hand. Square up with hand and tighten 3 thumbscrews. Note: we never aligned North and East with rows and columns because that moved the unvignetted field out of the desired frame transfer area.
4. Adjust *x*-axis to maximize unvignetted area (should be near 1.0 on micrometer stage), tighten *x*-axis lock screw. Adjust *y*-axis to maximize unvignetted area (should be near 1.0 on micrometer stage) and tighten *y*-axis lock screw. Read out settings for *x*-axis and *y*-axis micrometers.
5. Refocus the focus micrometer and tighten all 3 screws (lock screw and two others). Read out focus setting.
6. Wrap opaque cloth around instrument, so stray light does not enter instrument.
7. Run a focus curve for both NSFCAM and PCCD using telescope focus to confirm optimum focus.

Appendix IV. Single-Chord Astrometry for Linear Sky-Plane Motion

AIV.1 Motivation

Chapter 4 presents a detailed method for determining the closest approach of a star and solar system body (*i.e.*, planet, satellite, asteroid) passing nearby which relies only field stars and the body's ephemeris. As mentioned in that chapter, the *ephemeris method* is not applicable if the sky-plane path of the body is linear because the scale would only be determined in one direction (the direction of motion). This appendix presents an extension of the *ephemeris method* for such circumstances. This adaptation is called the *compromise method*, since it is a compromise between the ephemeris solution and the astrometric network solution. The ephemeris is used to determine the scale along the direction of motion, while the astrometric network and field stars determine the scale in the perpendicular direction.

AIV.2 The Compromise Method

We will pick up from the weighted-mean frame of the ephemeris method. This is where the two compromise method diverges from the ephemeris method. The registration to determine the transformations from the weighted-mean frame to the tangent plane, takes place in two parts: (i) the scale is set along the direction of motion by the ephemeris, and (ii) the scale perpendicular to the motion is determined from a secondary astrometric network. At this point, our observations are in a weighted-mean frame coordinate system whose axis are aligned with detector row and column. The centers of the occulting body, occulted star, and the weighted-mean frame coordinates for the field stars need to be rotated to a coordinate system with axes along and perpendicular to the direction of the occulting body's motion. We will call these directions, x and y.

Eq. AIV.1 shows the matrix to rotate the row and column centers of the nth field star (in the weighted-mean frame, hence the subscript r) to x and y, where θ is the angle from the column axis to the direction of the planet's motion. Analogous equations exist for the occulted star and occulting body. The origin is chosen to be the center of the occulting body measurements $\left(\langle c_{rpk}\rangle, \langle r_{rpk}\rangle\right)$. The subscript p stands for the occulting body (as in Chapter 4).

$$\begin{bmatrix} \bar{x}_n \\ \bar{y}_n \end{bmatrix} = \begin{bmatrix} \cos\theta & \sin\theta \\ -\sin\theta & \cos\theta \end{bmatrix} \begin{bmatrix} \bar{c}_n - \langle c_{rpk} \rangle \\ \bar{r}_n - \langle r_{rpk} \rangle \end{bmatrix} \tag{AIV.1}$$

Here is the equation for the occulted star positions (an analogous equation exists for the occulting body):

$$\begin{bmatrix} x_{r*k} \\ y_{r*k} \end{bmatrix} = \begin{bmatrix} \cos\theta & \sin\theta \\ -\sin\theta & \cos\theta \end{bmatrix} \begin{bmatrix} c_{r*k} - \langle c_{rpk} \rangle \\ r_{r*k} - \langle r_{rpk} \rangle \end{bmatrix} \tag{AIV.2}$$

Note that for the field stars we are transforming the weighted-mean centers of the stars, but for the occulted star and planet we are interested in all of the positions. All the centers for the occulting body are needed for the registration against the ephemeris and all of occulted star positions are needed to calculate the uncertainty in the closest approach distance. Only the weighted-mean field-star positions are needed because they form the reference coordinate system that will be used in the registration against the astrometric network. The rotated weighted-mean coordinate system is registered to the tangent-plane projection of the astrometric network using all field stars that appear in the network:

$$\begin{aligned} \xi_n &= m_1 + m_2 \bar{x}_n + m_3 \bar{y}_n \\ \eta_n &= m_4 + m_5 \bar{x}_n + m_6 \bar{y}_n \end{aligned} \tag{AIV.3}$$

Next we register the occulting body coordinates to the planet's ephemeris. The ephemeris needs to be topocentric and include a correction for light travel time (as discussed in Chapter 4).

$$\begin{aligned} \xi_{ek} &= b_1 + b_2 x_{rpk} + b_3 y_{rpk} \\ \eta_{ek} &= b_4 + b_5 x_{rpk} + b_6 y_{rpk} \end{aligned} \tag{AIV.4}$$

Now that we know the registration parameters, we can determine the tangent-plane coordinates of the occulted star:

$$\begin{aligned} \xi_* &= b_1 + b_2 \langle x_{r*k} \rangle + m_3 \langle y_{r*k} \rangle \\ \eta_* &= b_4 + b_5 \langle x_{r*k} \rangle + m_6 \langle y_{r*k} \rangle \end{aligned} \tag{AIV.5}$$

From here on, the compromise and ephemeris methods are the same. The RA and Dec of the occulted star and the impact parameter are calculated using the equations in Chapter 4.

We estimate the error in the star center using Eq. AIV.6. Note, the correlation coefficients are zero. By choosing the origin as the mean-ephemeris position, the correlation between the b_1 and b_2 (and between b_4 and b_5) is zero. The remaining

correlation terms are assumed to be zero since the parameters are derived from distinctly different registrations.

$$\sigma(\xi_*)^2 = \sigma(b_1)^2 + \sigma(b_2)^2\langle x_{r*k}\rangle + b_2\sigma\left(\langle x_{r*k}\rangle\right)^2 + \sigma(m_3)^2\langle y_{r*k}\rangle + m_3\sigma\left(\langle y_{r*k}\rangle\right)^2$$
$$\sigma(\eta_*)^2 = \sigma(b_4)^2 + \sigma(b_5)^2\langle x_{r*k}\rangle + b_5\sigma\left(\langle x_{r*k}\rangle\right)^2 + \sigma(m_6)^2\langle y_{r*k}\rangle + m_6\sigma\left(\langle y_{r*k}\rangle\right)^2 \quad \text{(AIV.6)}$$

This method uses the astrometric network, but only to set the scale over a very short distance (effectively the closest approach distance separating the star and body). In this way, the effect of any errors in the astrometric network is minimized.

AIV.3 Application to the Chiron Occultation of Ch08

The 1994 March 10 occultation of Ch08 by Chiron was observed by two stations–the KAO flying near Recife, Brazil and the South African Astronomical Observatory (SAAO). Both stations probed the same region near Chiron (to within 2 km), and neither observed a nuclear chord. Therefore, the occultation data are not able to define where the observed chords probed relative to Chiron. There was a large effort by multiple institutions to observe this occultation from the ground using 14-in portable telescopes in Brazil, but the predicted occultation track was north of them.

Fortunately, the United States Naval Observatory (USNO) at Flagstaff was able to record stare frame images of the occultation field before and after both of this event using their 61-in telescope (same configuration as the Tr60 observations in Chapter 4). Unfortunately, due to the time critical nature of occultations (Chiron and Ch08 need to be on the same stare frame), we cannot await the best conditions for observing. Observers at the USNO were able to take a total of 40 usable images on the night of the occultation and the night after (13 images on 1994 March 9; 27 images on 1994 March 10). The seeing on the first night was 2.5 arcsec, and a faint star in the vicinity of Ch08 was not resolved. The faint nearby star lies at a distance of 3.27 arcsec from the brighter one, at a position angle of 19.6°, and it has magnitude differences with Ch08 of 3.83 in the broadband red filter (6600-8300 Å) used by the U. S. Naval Observatory. Fortunately, the seeing on the next night was much better (1.0 arcsec). There were also 4 nights of astrometric data that do not have Chiron and Ch08 on the same stare frame, but could be used to determine the position of the Ch08 on the night of the occultation when it was blended with the fainter star. Table AIV.1 lists the stare frame observations taken of the Ch08 field by the USNO.

Table AIV.1 Ch08 Astrometric Data from the USNO

Date	No. Stare Frames
1994 Feb. 15	13[a]
1994 March 1	14[a]
1994 March 2	21[a]
1994 March 3	19[a]
1994 March 9	13[b]
1994 March 10	36[b]

[a] only Ch08 on stare frame
[b] Ch08 and Chiron on stare frame

To calculate a center for Ch08 (not the blended image of Ch08 and its nearby companion) for the March 9 data, we used 46 resolved observations from other nights. The centers of the stars on those 46 frames were found using DAOPHOT (as described in Chapter 4 for the Tr60 astrometric data). A mean frame was constructed using 10 field stars, Ch08 and the faint companion. This mean frame (unweighted) was registered linearly to each of the frames from March 9. Using the registration coefficients, the mean resolved Ch08 position (from the 46 frames) was transformed to the coordinate system for each of the frames with large seeing (where the center of Ch08 could not be discriminated from the center of the blended image). In this way, resolved Ch08 positions were obtained for each of the 13 frames from this night.

A secondary astrometric network was supplied by Brian Skiff who measured films taken at the 46-cm Schmidt telescope at Palomar Mountain by E. M. and C. S. Shoemaker (as a part of the Palomar Asteroid and Comet Survey) using the Lowell Observatory PDS and the ACRS catalog as a primary network. There were ten field stars common to all observations and the network. These stars were used to set the scale in the direction perpendicular to Chiron's motion using the compromise method. The topocentric ephemeris for Chiron came from Ted Bowell's asteroid ephemeris program.

The closest approach distance in kilometers for each of the observing sites is shown in Table AIV.2. Both sites probed the same region near Chiron. This facilitated the interpretation of the SAAO light curve, since there was an uncertainty in the timing of that data (Elliot *et al.* 1995).

Table AIV.2 Ch08 Occultation Circumstances

	KAO	SAAO
Impact Parameter (km)	107 ± 16	109 ± 16
Impact parameter f component (km)	47. ± 16	47. ± 16
Impact parameter g component (km)	96.± 16	98.± 16
shadow velocity (km/s)	18.3	18.1

From the 3σ uncertainty in the impact parameter, we can derive an upper limit on the radius of Chiron to be 155.5 km. Without these astrometry results, the interpretation of the Chiron occultation light curves would have been impossible. The symmetric placement of a low optical depth feature in the KAO light curve relative to the center of Chiron allows us to interpret it as a putative coma. See Elliot *et al.* (1995) and Olkin *et al.* (1994) for analysis of the occultation data.

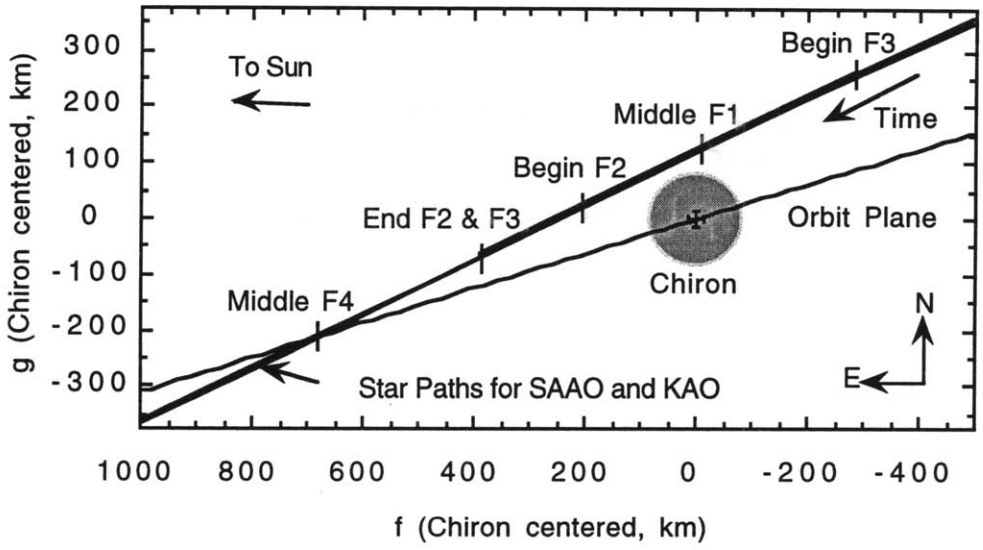

Figure AIV.1 The occulted star path relative to Chiron. This diagram of the Chiron-centered *fg* plane shows the star paths as seen by both observers. Also indicated for reference is Chiron's orbit plane. The position of the star at the time of particular occultation light curve features is indicated. Note that both stations probed the same near-nuclear environment (coincidentally). Without this post-event astrometry, interpretation of the light curve would be nearly impossible [after Elliot *et al.* (1995)].

Appendix V. Mathematica Notebooks

This appendix lists the *Mathematica* notebooks used in generating results for this thesis. For each table, the *Mathematica* notebook used to generate the results in that table are listed. For tables whose results are not derived from a *Mathematica* notebook, the entry is "N/A" for not applicable. These notebooks are all stored on the machine lowell.mit.edu, in folders contained in "Internal HD:Local Files:Projects:Triton:Tr148", "Internal HD:Local Files:Projects:Triton:Tr60" or "Internal HD:Local Files:Projects:Chiron". When multiple files of the same name exist, the folder is given.

Table AV.1 Mathematica Notebooks

Table	Mathematica Notebooks
Table 2.1 Observational Parameters	IRTF NSFCAM:Normalize:normalize 1.1.m, Lowell SNR 1.0.m, LIRC SNR 1.0.m, Pfit WIRO1 1.0.m Lit Curve Fit Results:SNRs
Table 2.2 Intensity of Tr148AB/Triton	KAO:Phot. Calibr:calibrate 1.3.m PCCD:Phot Calib.:calib 1.3.m compare with fit 1.2.m
Table 3.1 Tr60 Astrometric Data, RMS Error and Intensity Ratio	eph reg, rc, ab 1.7.m, USNO Photometry:USNO phot 1.6.m
Table 3.2 Maximum Image Displacements in the USNO Frames	Refrac & Aberr 1.1.m
Table 3.3 Tr60 Occultation Circumstances	eph reg, rc, ab 1.10.m
Table 3.4 Tr60 Photometry	USNO Photometry:calibration 2.2.m, USNO Photometry:USNO phot 1.6.m
Table 3.5 Tr60 Positions (J2000 FK5)	eph reg, rc, ab 1.7.m
Table 4.1 Geodetic Observatory Coordinates from GPS (WGS84)	N/A
Table 4.2 Tr148A and Tr148B Offsets from CAMC Position	Tr148AB fg soln3 1.5.m
Table 4.3 Tr148 Astrometric Solution	Tr148AB fg soln3 1.5.m
Table 4.4 Triton Longitude and Latitude Probed at Half-Light	Tr148AB fg soln3 1.6.m

Table 5.1 Isothermal Fit Results of IRTF Data	Fit Summary 1.8.m, Tr148_IRTF_P7_1.0.m, Tr148_IRTF_P9_1.0.m
Table 5.2 Tr148 Astrometric Solution	Tr148AB fg soln3 1.5.m, Fit Summary 1.8.m, Tr148_IRTF_P7_1.0.m
Table 5.3 Fitted and Calculated Background Levels	Tr60:Fitting Light Curve:Adopted DPS95 1.6.m, IRTF NSFCAM:calibration comparison 1.0.m, KAO:calibrate 1.3.m Lick-Snapshot:Phot. Calib.:compare with fit 1.2.m IRTF PCCD:PCCD Phot. Calib.:calib 1.3.m
Table 5.4 Immersion and Emersion Isothermal Fit Results	Fit Summary 1.10.m, Fit Summary IR 1.0.m, Tr148_IRTF_P7_1.0.m, Tr148_IRTF_P10_1.0.m, Tr148_IRTF_N3_1.0.m, Tr148_IRTF_N4_1.0.m, Tr148_KAO4_1.0.m, Tr148_KAO8_1.0.m, Tr148_Lick_A10_1.0.m, Tr148_Lick_B8_1.0.m, Tr148_FLG5_1.0.m, Tr148_W5_1.0.m
Table 5.5 Weighted Immersion and Emersion Isothermal Fit Results	Fit Summary 1.10.m, Fit Summary IR 1.0.m, Tr148_IRTF_P13_1.1.m, Tr148_IRTF_N6_1.0.m, Tr148_IRTF_N6_1.1.m, Tr148_KAO5_1.0.m, Tr148_KAO8_1.0.m
Table 5.6 Tr60 Isothermal Fit Results	Im/Em Results 1.0.m
Table 5.7 Power-Law Themal Gradient Fits	Fit Summary 1.10.m, Tr148_IRTF_P16_1.0.m Tr148_KAO14_1.0.m
Table 5.8 Correlation Matrix (IRTF-PCCD) Power-Law Thermal Gradient Fit	Fit Summary 1.10.m
Table 5.9 Adopted Isothermal Fit For Symetric Light Curves	Fit Summary 1.10.m, Tr148_Lick_A7_1.0.m, Tr148_Lick_A8_1.0.m, Tr148_KAO4_1.0.m,, Tr148_KAO6_1.0.m, Tr148_W4_1.1.m
Table 5.10 Correlation Matrix from Isothermal Fit of Lick-Tr148A Light Curve	Fit Summary 1.10.m

Table 7.1 Physical Model Fits	P1400_KAO1_1.0.m P1400_IRTF-PCCD1_1.0.m P1400_LickA1_1.0.m Pfit_IRTF5_1.0.m Pfit_KAO6_1.0.m Pfit_LickA4_1.0.m Pfit_Tr601_1.0.m
Table 7.2 Chord Length Difference	N/A
Table 8.1 Pressure at 1400 from Isothermal Fit of Data and Model	Im/Em Results 1.0.m, Fit Summary 1.8.m, Light Curve Fit Results:Fit Iso. Strobel 1.0.m
Table 8.2 Individual Magnitudes of Tr148A and Tr148B at V and K	Tr148 Diameter 1.1.m
Table AI.1 Occultations Observed Prior to 1996	N/A
Table AII.1 Our Stellar Occultation Predictions from 1992-1995	N/A
Table AII.2 Data and Predictions for the P28 Occultation	P28_Lick_anal6_1.1.m, P28-transit 7/26 1.0.m, P28 USNO61 anal1 1.0.m, P28 WAO anal6 1.2.m
Table AII.3 Final Predictions for Tr148 Occultation	Tr148 WAO anal3 1.0.m, Tr148 Lick anal18 dew 1.0.m, Tr148-transit alan5 1.0.m, USO61 anal3a 1.0.m, CAMC 1.0.m
Table AII.4 Final Astrometric Solutions	Tr148 Lick anal20 dew 1.1.m, USO61 anal5 1.0.m
Table AII.5 Occultation Candidate Magnitudes	N/A
Table AII.6 Refined Predictions For Selected Candidates	Tr176 1.0.m, Tr180 1.0.m, Pluto Events 1.0.m
Table AIV.1 Ch08 Astrometric Data from the USNO	N/A
Table AIV.2 Ch08 Occultation Circumstances	saao astrometry 1.8.m, compr. anal10 1.0.m

Appendix VI. Glossary

The definitions in this glossary come from Cruikshank (1995), Seidelmann (1992), Walker (1988) and J. Elliot's course notes for the MIT class "Observational Techniques of Optical Astronomy".

absolute magnitude — the apparent magnitude of an object if it were at a distance of 10 parsec

adiabat — the trajectory in pressure-temperature space followed by a parcel of matter which undergoes changes in volume without exchanging heat with its surroundings

airmass — the secant of the zenith distance (90° - altitude). It is a measure of the amount of atmosphere one is looking through. It has a minimum value of 1.0 when looking zenith

annual aberration — the component of stellar aberration (see stellar aberration) resulting from the motion of the Earth about the Sun

arcsec — one part in 3600 of a degree

Astronomical Unit (AU) — average distance between the Earth and Sun. 1.4959787×10^{11} m

bar — a unit of pressure: 1×10^{6} dyne/cm^{3}. The standard atmospheric pressure at Earth's surface (termed "one atmosphere") is 1.013 bar

CCD — charge-couple device

chords — an occultation light curve or just the immersion or emersion section

correlation coefficient — a dimensionless quantity taking values from –1 to +1 measuring the degree of linear association between two variates. A value of –1 indicates a perfect negative linear relationship, +1 a perfect positive relationship.

CTE charge transfer efficiency. The efficiency of transferring electrons from the wells of a CCD detector. If the efficiency is not 100%, charge will be left behind as the detector is read out.

deadtime the time between integrations

declination the angular distance on the celestial sphere north or south of the celestial equator. It is measured along the hour circle passing through the celestial object.

density scale height the distance in an atmosphere over which the number density changes by a factor of e

diurnal aberration the component of stellar aberration (see stellar aberration) resulting from the observer's diurnal motion about the center of the Earth

emersion that portion of an event (in this case a stellar occultation) in which one object (the star) reappears from behind another (the occulting body).

energy ratio a parameter in the model of Elliot and Young (1992). It is the ratio of the half-light radius to the scale height at the half-light radius.

ephemeris a tabulation of the positions of a celestial object in an orderly sequence for a number of dates

extinction the scattering or absorption of photons

EUV extreme ultraviolet radiation

far-limb flux the observed flux that was refracted across the x axis, see Figure 5.1

flat-field image an image of an evenly illuminated field

frame transfer a method for reading out a CCD to minimize deadtime. The recorded image is transferred to a different part of the detector after the exposure and read out during later integrations.

FWHM full width at half maximum

geocentric with reference to, or pertaining to, the center of the Earth

half-light radius the radius (typically in the planet plane) probed by a stellar occultation when the flux from the occulting star equals half its unocculted value

hour circle a great circle on the celestial sphere that passes through the celestial poles and is therefore perpendicular to the celestial equator

hydrostatic equilibrium the condition of stability that exists when gravitational forces are exactly balanced by counteracting gas and radiation pressure

immersion that portion of an event (in this case a stellar occultation) in which one object (the star) disappears behind another (the occulting body).

impact parameter the closest approach distance (usually measured in arcsec) between two celestial bodies.

IRTF Infrared Telescope Facility. Located on Mauna Kea, Hawaii.

ISS Imaging Science Sub System, the Voyager camera system

K filter center wavelength 2.21 μm and a FWHM of 0.39 μm

K' filter center wavelength 2.12 μm and a FWHM of 0.34 μm

KAO Kuiper Airborne Observatory. A modified C141 transport plane with a 0.9-m telescope.

Lick Observatory Lick Observatory is located on Mount Hamilton near San Jose, California.

light curve the record of observed flux from a body (or bodies)

light travel time the interval of time required for light to travel from a celestial body to the Earth. During this interval the motion of the body in space causes an angular displacement of its apparent place from its geometric position.

LIRC2	Lick Infrared Camera 2
Lowell Observatory	Lowell Observatory is located in Flagstaff, Arizona. The telescope used to observe the Tr148B occultation is located on Anderson Mesa which is outside of town.
magnetosphere	the region of space surrounding a rotating, magnetized sphere
magnitude	a measurement on a logarithmic scale of the brightness of a celestial object considered as a point source
meridian	a great circle passing through the celestial poles and through the zenith of any location on Earth
Mie scattering	a classical theory of scattering of light from homogeneous, spherical particles
microbar	μbar, 10^{-6} bar
NSFCAM	an astronomical instrument for imaging in the infrared
occultation	the obscuration of one celestial body by another of greater apparent diameter
oblateness	the ratio of the difference between the equatorial and polar radii to their mean value
parsec	the distance at which one astronomical unit subtends an arcsecond
PCCD	a Portable CCD instrument designed to perform high-speed imaging for occultation observations. Four PCCD systems exist.
photometry	a measurement of the intensity of light usually specified for a specific wavelength range
planet plane	the plane parallel to the shadow plane at the occulting body. See Figure 5.1.

pressure scale height — the distance in an atmosphere over which the pressure changes by a factor of *e*

R filter — center wavelength = 700 nm, passband = 220 nm

Rayleigh scattering — selective scattering (*i.e.* preferential scattering of shorter wavelengths) of light by very small particles suspended in a planetary atmosphere, or by molecules of the air itself. The scattering is inversely proportional to the fourth power of the wavelength.

refraction — the bending of a light ray as it passes through an atmosphere

right ascension — angular distance on the celestial sphere measured eastward along the celestial equator from the equinox to the hour circle passing through the celestial object

RSS — Radio Science Subsystem

scale height — the distance in an atmosphere over which the pressure or number density changes by a factor of e. For an isothermal atmosphere the pressure and density scale heights are equal.

secular aberration — the component of stellar aberration resulting from the essentially uniform and rectilinear motion of the entire solar system in space. Secular aberration is usually disregarded.

seeing — refers to the enlargement of and motion of an image due to random refraction of light by turbulent eddies in Earth's atmosphere.

shadow plane — the plane perpendicular to the direction of the occulted star whose origin is at the center of the Earth.

shadow velocity — the velocity of an occultation shadow as seen from an observer.

SNAPSHOT — a CCD instrument.

SNR — signal-to-noise ratio

spectral type categorization of stars according to their spectra, primarily due to differing temperatures of the stellar atmosphere. From hottest to coolest the spectral types are O, B, A, F, G, K, M.

stare frame a typical image from an array detector.

stellar aberration the apparent angular displacement of the observed position of a celestial body resulting from the motion of the observer. Stellar aberration is divided into diurnal, annual and secular components.

stratosphere an upper layer of a planetary atmosphere, above the troposphere and below the thermosphere, characterized by a vertical temperature gradient which is stable against convection

strip scan an arbitrarily long image of the sky recorded with an array detector. The telescope is left stationary, while the columns of the detector are clocked out at the same rate as the stellar images move across the detector. See Dunham *et al.* (1991) for more details.

subframe a subsection of an array detector

subsolar the point on a planet where the Sun is at the local zenith

tangent plane a plane parallel to the focal plane of the telescope on which the celestial sphere is projected. See *Green* (1985) for details.

thermosphere the region of temperature rise due to ionospheric heating

topocentric with reference to, or pertaining to, a point on the surface of the Earth, usually with reference to a coordinate system.

Tr148 The blended star (Tr148A-Tr148B)

Tr148A a star that was occulted by Triton on 1995 August 14. It has a companion, Tr148B.

Tr148B a star that was occulted by Triton on 1995 August 14. See Tr148A.

Tr60 a star that was occulted by Triton on 1993 July 10

transit	the passage of a celestial object across the meridian.
tropopause	the boundary between the troposphere and stratosphere (or for Triton, the thermosphere) where the vertical temperature gradient goes to zero
troposphere	region of atmosphere characterized by a convective (adiabatic) temperature gradient. This is typically the region where most weather occurs.
UT	Universal Time. A measure of time that conforms, within a close approximation, to the mean diurnal motion of the Sun and serves as the basis of all civil time keeping.
UVS	Ultraviolet Spectrometer on the Voyager spacecraft
vignetting	the diminution of observed flux due to an obstacle in the optical path
V filter	center wavelength = 550 nm, passband = 89 nm
WIRO	Wyoming Infrared Observatory. Located in Jelm, Wyoming.